SIMULATING TRANSIENT CLIMATE EVOLUTION

OF THE LAST DEGLACIATION WITH CCSM3

by

Feng He

A dissertation submitted in partial fulfillment of the

requirements for the degree of

Doctor of Philosophy

(Atmospheric and Oceanic Sciences)

at the

UNIVERSITY OF WISCONSIN-MADISON

2011

The University of Wisconsin - Madison
The Graduate School

Candidate for the degree of Doctor of Philosophy

He, Feng

9026511742

Major: **Atmospheric and Oceanic Sciences**
(if this is a joint degree, list both majors. If special committee degree, state specific name.)

Minor: **Distributed**

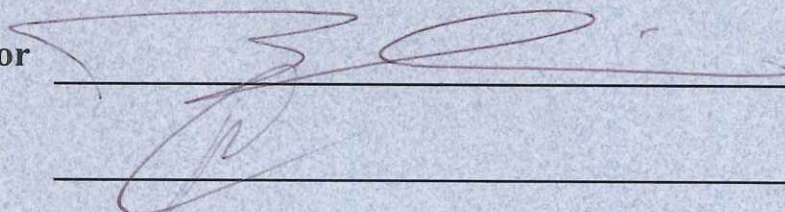*We, the undersigned, report that as a committee we have examined* **Feng He**

on _____09/27/10_____ , *and upon the work done in the subjects named and upon the*

dissertation presented by the candidate we find that the candidate may properly be admitted to the degree of Doctor of Philosophy

Committee Member Names
Last Name, First Name, Middle

Signature of Committee Members
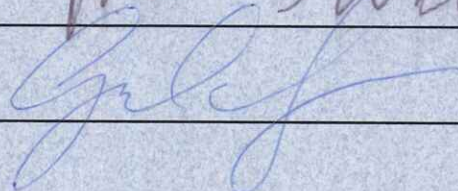
Liu, Zhengyu	**Advisor**
Carlson, Anders	
Hitchman, Matt	*Matthew H. Hitchman*
Williams, John W.	
McKinley, Galen	

I dissent from the following report _____

Dissertation Approved by Graduate School on

The University of Wisconsin - Madison
The Graduate School

Candidate for the degree of Doctor of Philosophy

He, Feng

9026511742

Major: Atmospheric and Oceanic Sciences
(If this is a joint degree, list both majors. If special committee degree, state specific name.)

Minor: Distributed

We, the undersigned, report that as a committee we have examined Feng He

on _____ and upon the work done in the subjects named and upon the

examination administered by the committee we find that the candidate may properly be admitted to the degree of Doctor of Philosophy

Committee Member Names	Signature of Committee Members
Last Name, First Name, Middle	
Liu, Zhengyu	Advisor
Carlson, Anders	
Hitchman, Matt	
Williams, John W.	
McKinley, Galen	

I dissent from the following report

Dissertation Approved by Graduate School on

SIMULATING TRANSIENT CLIMATE
EVOLUTION OF THE LAST DEGLACIATION
WITH CCSM3

submitted to the Graduate School of the
University of Wisconsin-Madison
in partial fulfillment of the requirements for the
degree of Doctor of Philosophy

By

Feng He

Date of final oral examination: September 27, 2010

Month and year degree to be awarded: May 2011

The dissertation is approved by the following members of the Final Oral Committee:

Zhengyu Liu, Professor of Atmospheric and Oceanic Sciences
Matthew H. Hitchman, Professor of Atmospheric and Oceanic Sciences
John W. (Jack) Williams, Associate Professor of Geography
Galen A. McKinley, Assistant Professor of Atmospheric and Oceanic Sciences
Anders E. Carlson, Assistant Professor of Geoscience

To my wife, Xiaoyi Sun

for her love and encouragement

Simulating Transient Climate Evolution of the Last Deglaciation with CCSM3

by

Feng He

Under the supervision of Professor Zhengyu Liu

At the University of Wisconsin-Madison

ABSTRACT

The transient climate evolution of last deglaciation 21,000 to 10,000 years ago (21 to 10 ka) provides key observations for constraining climate sensitivity and understanding global carbon cycle. Here I present the first complete synchronously coupled atmosphere-ocean general circulation model simulation of the last deglaciation using NCAR-CCSM3. The transient simulation reproduces many major features of the deglacial climate evolution in Greenland, Antarctic, tropical Pacific, Southern and Deep Ocean, suggesting CCSM3 exhibits reasonable climate sensitivity in those regions and is capable of simulating abrupt climate changes.

In the transient simulation, the Northern Hemisphere meltwater (NHMW) forcing associated with the onset of Northern Hemisphere deglaciation ~19 ka results in a near-collapse of the Atlantic Meridional Overturning Circulation (AMOC) by 17.0 ka. The reduction of the AMOC causes Oldest Dryas (19-14.5 ka) cooling in the Greenland ice core whereas the sudden

termination of NHMW at 14.67 ka is responsible for the resumption of AMOC and abrupt Bølling warming. Meltwater discharge during meltwater pulse 1A (mwp-1A) causes a reduction in the AMOC and the associated cooling during the Older Dryas event at ~14 ka. The reduction of NHMW after mwp-1A causes the Allerød warm period ~14-12.9 ka, while a subsequent increase in NHMW weakens the AMOC, resulting in the Younger Dryas cold interval (~12.9-11.7 ka), although the cooling is less than that reconstructed from Greenland ice cores. Following the Younger Dryas, continued Northern Hemisphere ice-sheet melting prevents AMOC from reaching the Holocene level and causes cooler Greenland surface air temperature than proxy records in early Holocene.

In particular, our simulation supports the view that the last deglaciation is triggered by the enhanced spring-summer insolation locally in the Northern Hemisphere. Northern Hemisphere glacial meltwater is able to induce the early deglacial warming of the Southern and Deep Ocean, and accounts for the lead-lag relationship among the Southern Ocean, tropical Pacific and Northern Hemisphere observed during the last deglaciation. Furthermore, by inducing deep ocean warming and Southern Ocean sea ice retreat, Northern Hemisphere glacial meltwater likely plays an active role in deglacial CO_2 rise and gives an explanation for the associations between Heinrich events and atmospheric CO_2 rise.

ACKNOWLEDGEMENTS

The completion of this thesis would have not been possible without the help from many people. I am deeply indebted to my adviser, Professor Zhengyu Liu, who brought me into the fascinating field of paleoclimatology and provided me his full trust in carrying out one of the most epic numerical modeling in the climate community to date. I am always encouraged by his passion for science and appreciate his special insights during our discussions. It is my great pleasure to have this opportunity to work under Professor Liu's guidance.

I am also grateful to the other TraCE-21K project members: Esther Brady, Anders Carlson, Peter Clark, Eric Davidson, Robert Jacob, Bette Otto-Bliesner, Nan Rosenbloom and Robert Tomas. With their encouragement, I had a smooth and quick start on my journey of the paleoclimate modeling. Their continuous scientific insights and technical support helped me to complete transient simulation of the last 21,000 years in CCSM3 within three years.

I am also grateful to my PhD committee members: Anders Carlson, Matt Hitchman, Zhengyu Liu, Galen McKinley and Jack Williams. Without their encouragement and scientific comments, I could not have completed my PhD thesis.

I would also like to thank Pat Behling and Kevin Braun for computer assistance and advice on this study. I also want to express my gratitude to Julie Nielson for her excellent administrative work that provided the most comfortable research environment I ever had.

I would also want to thank all the faculties and researchers in CCR, especially the students in our research group: Jun Cheng, Yafang Zhong, Wei Liu, Mark Wehrenberg, Jiaxu

Zhang, Karen Russ, Yun Liu, Guangshan Chen, Shu Wu, John-Paul Argenti. The weekly student meeting has always broadened my horizon on climate research.

A special thanks goes to my bachelor thesis adviser, Dr. Jiwei Tian, who introduced me into global climate research and provided me with the framework of my knowledge on climate dynamics.

I am also grateful for the support from my parents and parent-in-laws. It is their prayers that helped me to overcome the difficulties.

As always, my wife, Xiaoyi Sun and my son, Zijun He (Le Le), deserve the most gratitude from me. I enjoy every minute of our life and share with each other the happiness as well as the sadness. It is their love that gives me the strength to move forward and enjoy my work as a climate researcher.

I would like to thank Michael Notaro, Steve Vavrus, John Kutzbach, Kenji Kawamura, and Jinming Yu for very useful comments at various stages of this study. This research used resources of the Oak Ridge Leadership Computing Facility at the Oak Ridge National Laboratory, which is supported by the Office of Science of the U.S. Department of Energy under Contract No. DE-AC05-00OR22725. The simulation was conducted on supercomputers Phoenix and Jaguar and the results were analyzed on the analysis server Lens.

Contents

Abbreviations:

Abbreviations	Full names
AABW	Antarctic Bottom Water
AMOC	Atlantic Meridional Overturning Circulation
BA	Bølling-Allerød
DGVM	Dynamic global vegetation model
D/O	Dansgaard-Oeschger
GHG	Greenhouse gas
Greenland SAT	SAT at the summit of Greenland
H1	Heinrich event 1
HS1	Heinrich Stadial 1
IACP	Intra-Allerød Cold Period
ka	1,000 years before A. D. 1950
kyr	1,000 years
LGM	Last Glacial Maximum
m/kyr	1 meter of equivalent global sea level rise per thousand year
MIS3	Marine isotope stage 3
mwp-1A	Meltwater pulse 1A
NADW	North Atlantic Deep Water
NHMW	Northern Hemisphere Meltwater
SAT	Surface air temperature
SHMW	Southern Hemisphere Meltwater
Sv	Sverdrup
TraCE-21K	Transient simulation of Climate Evolution of the last 21,000 years
YD	Younger Dryas

Chapter 1   Transient climate evolution of the last deglaciation

Through the late Quaternary period of past one million years, the Earth has experienced rather regular ice age cycles once every 100,000 years [Hays et al., 1976]. Various natural archives of the Earth have preserved rich climatic information for these ice age cycles. Scientists take advantage of these proxy records to study the Earth's climate dynamics and to better project future climate changes. The last deglaciation (~21 to 10 ka) (ka: 1,000 years ago) was the most recent major natural global warming, with a concurrent CO_2 rise of 70~80 ppmv (parts per million by volume) that is comparable in magnitude to the rise caused by anthropogenic emissions between the industrial revolution and the end of 20th century [Karl and Trenberth, 2003]. Another striking feature during the last deglaciation is the abrupt climate change events that punctuated the overall warming trend. The Greenland ice cores have recorded surface air temperature (SAT) changes of more than 10 ^{o}C in few decades during Bølling-Allerød (BA) and Younger Dryas (YD) [Severinghaus and Brook, 1999; Grachev and Severinghaus, 2005]. With extensive proxy data and relatively less dating uncertainty than earlier terminations, the last deglaciation provides a unique opportunity to test the sensitivity of climate models to CO_2 as well as the capability of the models in predicting abrupt climate changes. In the following, I will describe the current state of our understanding of the transient climate evolution of the last deglaciation based on paleoclimatic proxy data, with the focus on the deglacial history of polar temperatures as well as its potential drivers, such as insolation, CO_2, ice sheet and ocean circulation.

1.1   Greenland and Antarctic temperature

Our understandings of the Earth's climate evolution during the last deglaciation are mostly based on the SAT reconstructions from lake sediments and polar ice cores. Based on Greenland GISP2 SAT record [Alley, 2000; Cuffey and Clow, 1997] (Fig. 1 C), the sequence of the last deglaciation includes the Last Glacial Maximum (LGM) from 26 to 19 ka, the Heinrich Stadial 1 (HS1) from 19 to 14.7 ka, the BA from 14.7 to 12.9 ka, the YD from 12.9 to 11.7 ka and the Holocene from 11.7 ka to the start of industrial era (~1750 AD) [Rasmussen et al., 2006]. During the LGM, the SAT at the Summit Greenland (Greenland SAT thereafter) increased by more than 5 ^{o}C. In HS1, Greenland SAT decreased by ~4 ^{o}C between 19 ka and 17~16 ka and then increased by 2~3 ^{o}C before the onset of BA. The onset of BA is quite abrupt, with ~13 ^{o}C increase of SAT in less than 150 years [Cuffey and Clow, 1997]. BA lasted for ~1,700 years and exhibited several centennial oscillations, including the Older Dryas and the Intra-Allerød Cold Period (IACP). The Allerød warming ended with the 1,200-year YD cooling episode with ~9 ^{o}C cooling during its onset and ~10 ^{o}C warming at its close [Grachev and Severinghaus, 2005]. During the YD/Holocene transition, Greenland SAT warmed by ~6 ^{o}C and reached Holocene levels. During the Holocene, Greenland SAT is fairly stable, with weak millennial oscillations of less than 2 ^{o}C. The 8.2-ka event started ~8.2 ka and lasted ~150 years, during which Greenland SAT dropped by ~3 ^{o}C [Kobashi et al., 2007]. During the last two millennia, there was a weak cooling trend of ~1 ^{o}C/kyr (kyr, 1,000 years). Overall, the total Greenland SAT increased by 11 ^{o}C between the LGM and the end of Holocene.

Compared with the dramatic climate swings in Greenland, the climate evolution of Antarctic during the last deglaciation is more gradual (Fig. 1 D). Based on SAT reconstruction from Dome C

and Dome Talos, the deglacial warming in Antarctic occurred concurrently with the cold episodes of Greenland during the HS1 and YD, and paused or even reversed during BA [Jouzel et al., 2007, Stenni et al., 2011]. The first stage of warming started at ~18 ka and stopped at the end of HS1 with 5~6 $^{\circ}$C increase of SAT. The second stage of warming occurred during YD with a SAT increase of 4 $^{\circ}$C. The deglacial warming in the Antarctic concluded at the end of YD (11.7 ka), about 1,200 years before the end of Greenland warming (~10 ka). During the Holocene, the Antarctic temperature did not exhibit significant millennial variability. Overall, the total warming from Antarctic since the LGM is ~9 $^{\circ}$C [Jouzel et al., 2007].

1.2   Northern Hemisphere Ice Sheets

Massive ice sheets covered the North America, Greenland and Eurasia at the LGM with the height of North American Ice Sheet being more than 4.5 km (Fig. 2) [Peltier, 2004]. Between the LGM and BA, the Eurasian Ice Sheet retreated significantly with the area coverage reduced by about two thirds. During this period, the area coverage of North American Ice Sheet remained more or less the same. However, the total volume of the North American Ice Sheet reduced significantly. For example, the peak of the North American Ice Sheet, the Keewatin Dome, dropped from more than 4.5 km to below 4 km with the height of the surrounding area also reduced from 3 km to 2.5 km. The North American Ice Sheets rapidly retreated between BA and YD, during which most of the Cordilleran Ice Sheet in the western North American disappeared and the majority of the remaining Laurentide Ice Sheet was below 2 km. The Eurasian Ice Sheet

eventually disappeared ~8 ka, so did the Laurentide Ice Sheet ~6 ka. The last deglaciation completely ended around 6 ka, when the mass balance of both the Greenland and Antarctic Ice Sheet approximately reached their equilibrium in the Holocene.

1.3   Northern Hemisphere insolation

According to Milankovitch theory, the ice age cycles were paced by the Earth's orbital variations, with the Northern Hemisphere summer insolation intensity playing a dominant role in the growth and decay of Northern Hemisphere Ice Sheets [Milankovitch, 1941]. During the last 21,000 years, solar radiation varies mostly due to the gradual shift in the orientation of Earth's axis of rotation, i.e., the precession of Earth's orbit (Fig. 1 A). At both the LGM and present, the Earth's aphelion, i.e., the farthest point from the Earth's orbit to the Sun, occurs during the Northern Hemisphere summer, resulting in less Northern Hemisphere summertime incoming solar radiation than during early Holocene, when the Earth's aphelion occurs during the Northern Hemisphere winter. As a result, the Northern Hemisphere summer insolation intensity was at a minimum between 26 and 19 ka (Fig. 1 A), during which most of the Northern Hemisphere Ice Sheets reached their maximum size [Clark et al., 2009]. The increase of Northern Hemisphere summer insolation intensity after 21 ka is believed to have triggered the onset of the last deglaciation. Between 20 and 19 ka, sea level started to rise as a result of the glacial meltwater discharge into the ocean [Clark et al., 2004] (Fig. 1 B). Between 22 and 11 ka, Northern Hemisphere summer insolation intensity at 60° N progressively increased by ~60 W m^{-2}, reaching a maximum at the onset of Holocene. During the Holocene epoch of last 10,000 years, it gradually decreased by ~50 W m^{-2}. At present, the Northern Hemisphere summer insolation

intensity is in its minimum of the precession cycle with an orbital configuration similar to that during the LGM.

1.4   Atmospheric CO_2 concentration

Atmospheric CO_2 has long been suggested to play an important role in amplifying the relatively weak orbital forcing during 100,000-year ice age cycles [Pisias and Shackleton, 1984; Genthon et al., 1987]. Similar to Antarctic temperature, the deglacial CO_2 rise also occurred in two stages within HS1 and YD [Monnin et al., 2001; Joos and Spahni, 2008] (Fig. 1 A). The atmospheric CO_2 concentration varied between 185 to 190 ppmv during the LGM and started to rise at ~17 ka within HS1. The increase of CO_2 paused and reversed within the BA after increasing from 190 to 240 ppmv between 17 ka and the onset of the BA. After a ~5 ppmv drop between the BA and YD, CO_2 resumed its rising ~12.5 ka in the middle of YD and increased another ~30 ppmv from 235 to 265 ppmv before the onset of the Holocene. The total CO_2 rise during the last deglaciation was 75 ppmv (from 190 to 265 ppmv). During the early Holocene, CO_2 decreased by 5 ppmv between 10 and 8 ka, and then started to rise by 20 ppmv to reach the preindustrial level of 280 ppmv. The two-stage CO_2 rise during the last deglaciation suggests that the atmospheric CO_2 tends to rise during cold events of HS1 and YD [Marchitto et al., 2007; Anderson et al., 2009; Skinner et al., 2010; Denton et al., 2010], and tends to decline by several ppmv during warm period, such as BA and early Holocene. However, there is still ~1,000-year uncertainty of the age of atmosphere CO_2 reconstruction during the last deglaciation [Marchitto et al., 2007; Anderson et al., 2009; Lemieux-Dudon et al., 2010]. The CO_2 record used in this study adopted the EDC1 age model [Monnin et al., 2001]. If GISP2 age model is adopted

[Marchitto et al., 2007], the CO_2 record can be shifted by ~1,000 years earlier during the last deglaciation, which suggests that deglacial CO_2 rise started ~18 ka.

1.5   Atlantic meridional overturning circulation (AMOC)

The smooth forcing from insolation and CO_2 has difficulty in causing the millennial climate variability over the Greenland. Because ocean circulation significantly affects climate variability via the associated oceanic heat transport and various positive feedbacks (such as the ice-albedo feedback) [Liu and Alexander, 2007], the "climatic roller-coasters" recorded by Greenland ice cores have been suggested to be caused by the variability of Atlantic Meridional Overturning Circulation (AMOC) [Broecker et al., 1985]. Recent proxy reconstructions of AMOC from deep sediments provide further evidence that the millennia variability of AMOC during the last deglaciation occurred in tandem with that of the Greenland SAT [McManus et al., 2004] (Fig. 1 C and E). For example, during the HS1 and YD, the reduction of AMOC occurred when there was significant cooling over the Greenland; at the onset of BA warming, the Greenland abruptly warmed up with the abrupt resumption of AMOC at the end of HS1.

The close relationship between AMOC and abrupt climate change events suggests that it is possible to conduct the Transient simulation of Climate Evolution of the last 21,000 years (TraCE-21K) in climate models by modulating the strength of AMOC as well as greenhouse gas (GHG) concentration and earth's orbital parameters. Earlier modeling studies have shown that AMOC is quite sensitive to the surface meltwater fluxes and can exhibit a hysteresis behavior in simple box models or more complex ocean general circulation models [Stommel, 1961; Rahmstorf et al., 2005]. However, limited by the required massive computation and storage resources, it is only recently that transient simulation of the last deglaciation was carried out in

synchronously coupled atmosphere-ocean global climate models [Liu et al., 2009], which include the most advanced climate physics and are currently being used for future climate projections.

1.6   Challenges of transient simulation of the last deglaciation

The major challenge of simulating the last deglaciation involves the insufficient knowledge of meltwater fluxes from retreating glaciers during the last deglaciation. Even though the meltwater fluxes are closely related to the sea level reconstruction, they are still loosely constrained, because sea level records cannot constrain the location of the meltwater fluxes, only with a few exceptions [Clark et al., 2002; Bassett et al., 2005]. On the other hand, there are also large uncertainties regarding the sea level rise reconstruction. For example, the lowest stand of the sea level during the LGM is still controversial with the lower and upper limit at 120 and 135 meters [Peltier and Fairbanks, 2006; Yokoyama et al., 2000]. Another example is the meltwater pulse 1A (mwp-1A), one of the most rapid sea level rise events during the last deglaciation, whose origin is still controversial. Peltier [2004] assigns the entire 20m sea level rise during mwp-1A to a Northern-Hemisphere origin, which in state-of-the-art climate models triggers an AMOC collapse [Stouffer et al., 2006]. However, reconstructions suggest that the AMOC during mwp-1A did not collapse [McManus et al., 2004]. Using a glacial isostatic adjustment model, Clark et al. [2002] and Bassett et al. [2005] found that a large contribution from the Antarctic Ice Sheet to mwp-1A (~15-meters eustatic equivalent) resolves the discrepancies among the far field sea level rise reconstructions.

There are also some debates on the causality between mwp-1A and BA. After coupling a 3D ocean model with an energy balance atmosphere model, Weaver et al. [2003] found that the meltwater forcing from the Antarctic can initiate the resumption of the collapsed AMOC at the

end of HS1 and trigger the BA warming. However, this result cannot be verified in fully coupled climate models [Stouffer et al., 2007]. Furthermore, Stanford et al. [2006] suggests that mwp-1A occurred after BA event and the impact of mwp-1A is to induce Older Dryas cooling. All these controversies demonstrate the difficulties in nailing down the meltwater fluxes, and show that a systematic simulation of the last deglaciation is needed to elucidate these problems.

References

Alley, R. B. (2000), The Younger Dryas cold interval as viewed from central Greenland, Quaternary Science Reviews, 19(1-5), 213-226, doi: DOI: 10.1016/S0277-3791(99)00062-1.

Anderson, R. F., S. Ali, L. I. Bradtmiller, S. H. H. Nielsen, M. Q. Fleisher, B. E. Anderson, and L. H. Burckle (2009), Wind-Driven Upwelling in the Southern Ocean and the Deglacial Rise in Atmospheric CO_2, Science, 323(5920), 1443-1448, doi: 10.1126/science.1167441.

Bard, E., B. Hamelin, M. Arnold, L. Montaggioni, and G. Cabioch (1996), Deglacial sea-level record from Tahiti corals and the timing of global meltwater discharge, Nature, 382, 241.

Bassett, S. E., G. A. Milne, J. X. Mitrovica, and P. U. Clark (2005), Ice Sheet and Solid Earth Influences on Far-Field Sea-Level Histories, Science, 309(5736), 925-928, doi: 10.1126/science.1111575.

Berger, A. L. (1978), Long-Term Variations of Daily Insolation and Quaternary Climatic Changes, J.Atmos.Sci., 35(12), 2362-2367.

Broecker, W. S., D. M. Peteet, and D. Rind (1985), Does the ocean-atmosphere system have more than one stable mode of operation? Nature, 315(6014), 21-26.

Clark, P. U., J. X. Mitrovica, G. A. Milne, and M. E. Tamisiea (2002), Sea-Level Fingerprinting as a Direct Test for the Source of Global Meltwater Pulse IA, Science, 295(5564), 2438-2441, doi: 10.1126/science.1068797.

Clark, P. U., A. S. Dyke, J. D. Shakun, A. E. Carlson, J. Clark, B. Wohlfarth, J. X. Mitrovica, S. W. Hostetler, and A. M. McCabe (2009), The Last Glacial Maximum, Science, 325(5941), 710-714, doi: 10.1126/science.1172873.

Clark, P. U., A. M. McCabe, A. C. Mix, and A. J. Weaver (2004), Rapid Rise of Sea Level 19,000 Years Ago and Its Global Implications, Science, 304(5674), 1141-1144, doi: 10.1126/science.1094449.

Cuffey, K. M., and G. D. Clow (1997), Temperature, accumulation, and ice sheet elevation in central Greenland through the last deglacial transition, Journal of Geophysical Research, 102(C12), 26383-26396.

Denton, G. H., R. F. Anderson, J. R. Toggweiler, R. L. Edwards, J. M. Schaefer, and A. E. Putnam (2010), The Last Glacial Termination, Science, 328(5986), 1652-1656, doi: 10.1126/science.1184119.

Genthon, G., J. M. Barnola, D. Raynaud, C. Lorius, J. Jouzel, N. I. Barkov, Y. S. Korotkevich, and V. M. Kotlyakov (1987), Vostok ice core: climatic response to CO_2 and orbital forcing changes over the last climatic cycle, Nature, 329(6138), 414-418.

Grachev, A. M., and J. P. Severinghaus (2005), A revised +10±4 °C magnitude of the abrupt change in Greenland temperature at the Younger Dryas termination using published GISP2 gas isotope data and air thermal diffusion constants, Quaternary Science Reviews, 24(5-6), 513-519, doi: DOI: 10.1016/j.quascirev.2004.10.016.

Hanebuth, T., K. Stattegger, and P. M. Grootes (2000), Rapid Flooding of the Sunda Shelf: A Late-Glacial Sea-Level Record, Science, 288(5468), 1033-1035, doi: 10.1126/science.288.5468.1033.

Hays, H. D., J. Imbrie, and N. J. Shackleton (1976), Variations in the earth's orbit: pacemaker of the ice ages, Science, 194, 1121.

Joos, F., and R. Spahni (2008), Rates of change in natural and anthropogenic radiative forcing over the past 20,000 years, Proceedings of the National Academy of Sciences, 105(5), 1425-1430, doi: 10.1073/pnas.0707386105.

Jouzel, J., et al (2007), Orbital and Millennial Antarctic Climate Variability over the Past 800,000 Years, Science, , doi: 10.1126/science.1141038.

Karl, T. R., and K. E. Trenberth (2003), Modern Global Climate Change, Science, 302(5651), 1719-1723, doi: 10.1126/science.109022

Kobashi, T., J. P. Severinghaus, E. J. Brook, J. Barnola, and A. M. Grachev (2007), Precise timing and characterization of abrupt climate change 8200 years ago from air trapped in polar ice, Quaternary Science Reviews, 26(9-10), 1212-1222, doi: DOI: 10.1016/j.quascirev.2007.01.009. 8.

Lemieux-Dudon, B., E. Blayo, J. Petit, C. Waelbroeck, A. Svensson, C. Ritz, J. Barnola, B. M. Narcisi, and F. Parrenin (2010), Consistent dating for Antarctic and Greenland ice cores, Quaternary Science Reviews, 29(1-2), 8-20, doi: DOI: 10.1016/j.quascirev.2009.11.010.

Liu, Z., and M. Alexander (2007), Atmospheric bridge, oceanic tunnel, and global climatic teleconnections, Rev.Geophys., 45(2), RG2005, doi: 10.1029/2005RG000172.

Marchitto, T. M., S. J. Lehman, J. D. Ortiz, J. Fluckiger, and A. van Geen (2007), Marine Radiocarbon Evidence for the Mechanism of Deglacial Atmospheric CO_2 Rise, Science, , 1138679.

McManus, J. F., R. Francois, J. M. Gherardi, L. D. Keigwin, and S. Brown-Leger (2004), Collapse and rapid resumption of Atlantic meridional circulation linked to deglacial climate changes, Nature, 428(6985), 834-837.

Milankovitch, M. (1941), Kanon der Erdbestrahlung und seine Anwendung auf das Eiszeitenproblem, Royal Serbian Academy Special Publication 132, Belgrade, Serbia.

Monnin, E., A. Indermuhle, A. Dallenbach, J. Fluckiger, B. Stauffer, T. F. Stocker, D. Raynaud, and J. Barnola (2001), Atmospheric CO_2 Concentrations over the Last Glacial Termination, Science, 291(5501), 112-114, doi: 10.1126/science.291.5501.112.

Peltier, W. R. (2004), Global glacial isostasy and the surface of the ice-age Earth- The ICE-5 G(VM 2) model and GRACE, Annu.Rev.Earth Planet.Sci., 32(1), 111-149.

Peltier, W. R., and R. G. Fairbanks (2006), Global glacial ice volume and Last Glacial Maximum duration from an extended Barbados sea level record, Quaternary Science Reviews, 25(23-24), 3322-3337.

Pisias, N. G., and N. J. Shackleton (1984), Modelling the global climate response to orbital forcing and atmospheric carbon dioxide changes, Nature, 310(5980), 757-759.

Rahmstorf, S., M. Crucifix, A. Ganopolski, H. Goosse, I. Kamenkovich, R. Knutti, G. Lohmann, R. Marsh, L. A. Mysak, and Z. Wang (2005), Thermohaline circulation hysteresis: A model intercomparison, Geophys.Res.Lett., 32, L23605.

Rasmussen, S. O., et al (2006), A new Greenland ice core chronology for the last glacial termination, J.Geophys.Res., 111, D06102, doi: 10.1029/2005JD006079.

Severinghaus, J. P., and E. J. Brook (1999), Abrupt Climate Change at the End of the Last Glacial Period Inferred from Trapped Air in Polar Ice, Science, 286(5441), 930-934, doi: 10.1126/science.286.5441.930.

Skinner, L. C., S. Fallon, C. Waelbroeck, E. Michel, and S. Barker (2010), Ventilation of the Deep Southern Ocean and Deglacial CO_2 Rise, Science, 328(5982), 1147-1151, doi: 10.1126/science.1183627.

Stanford, J. D., E. J. Rohling, S. E. Hunter, A. P. Roberts, S. O. Rasmussen, E. Bard, J. McManus, and R. G. Fairbanks (2006), Timing of meltwater pulse 1a and climate responses to meltwater injections, Paleoceanography, 21(4), PA4103.

Stenni, B., et al (2011), Expression of the bipolar see-saw in Antarctic climate records during the last deglaciation, Nature Geosci, 4(1), 46-49.

Stommel, H. (1961), Thermohaline convection with two stable regimes of flow, Tellus, 13(2), 224-230.

Stouffer, R. J., D. Seidov, and B. J. Haupt (2007), Climate Response to External Sources of Freshwater: North Atlantic versus the Southern Ocean, J.Clim., 20(3), 436-448.

Stouffer, R. J., J. Yin, J. M. Gregory, K. W. Dixon, M. J. Spelman, W. Hurlin, A. J. Weaver, M. Eby, G. M. Flato, and H. Hasumi (2006), Investigating the Causes of the Response of the Thermohaline Circulation to Past and Future Climate Changes, J.Clim., 19(8), 1365-1387.

Weaver, A. J., O. A. Saenko, P. U. Clark, and J. X. Mitrovica (2003), Meltwater Pulse 1A from Antarctica as a Trigger of the Bølling-Allerød Warm Interval, Science, 299(5613), 1709-1713, doi: 10.1126/science.1081002.

Yokoyama, Y., K. Lambeck, P. De Deckker, P. Johnston, and L. K. Fifield (2000), Timing of the Last Glacial Maximum from observed sea-level minima, Nature, 406(6797), 713-716.
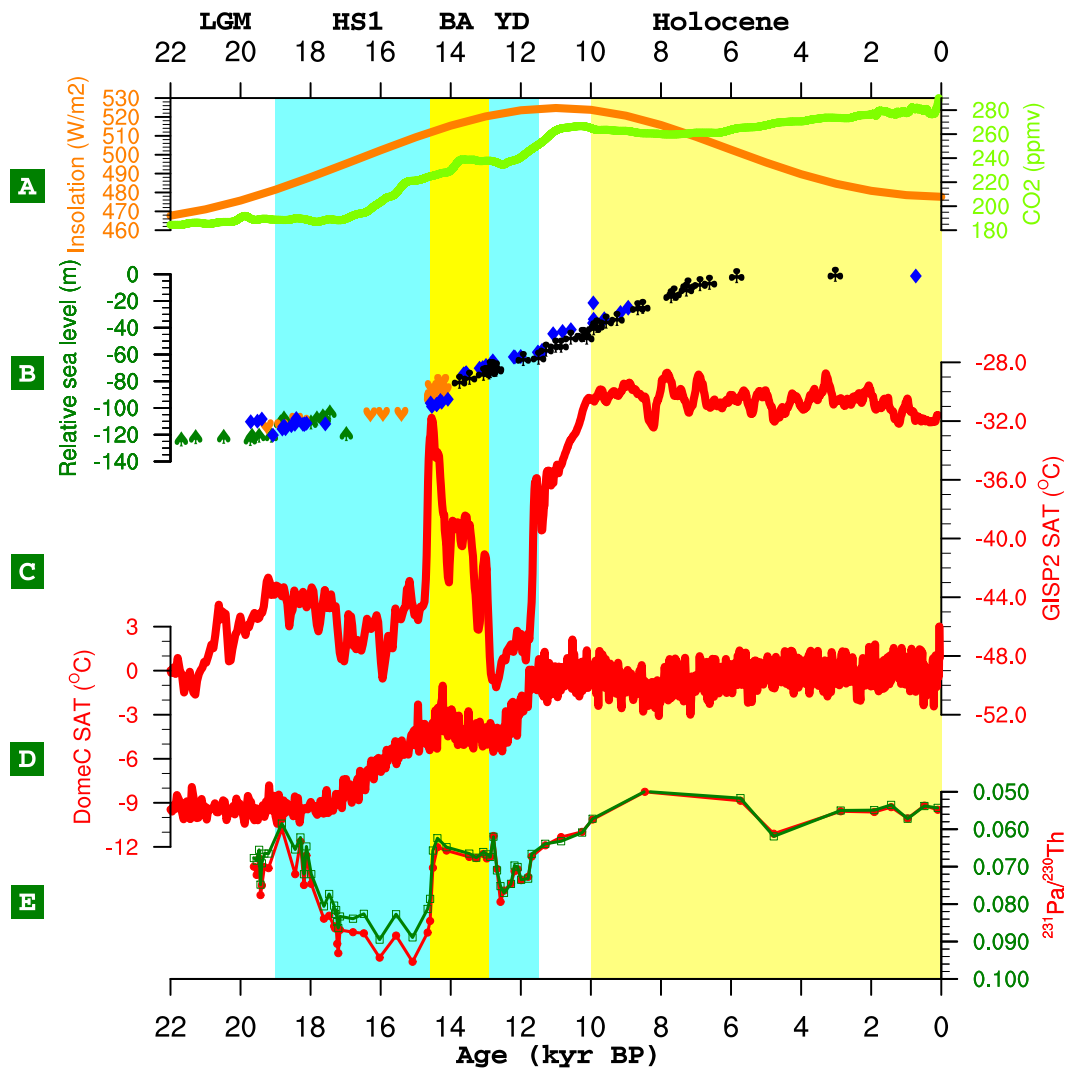
Figures

Figure 1: Climate evolution during the last deglaciation. (**A**) June 21st insolation at 60°N (orange) [Berger, 1978] and atmospheric CO₂ concentration (green) [Joos and Spahni, 2008]. ppmv, parts per million by volume. (**B**) Relative sea level. Sea level data are from Barbados (blue) [Peltier and Fairbanks, 2006], Bonaparte Gulf (green) [Yokoyama et al., 2000], Sunda Shelf (orange) [Hanebuth et al., 2000] and Tahiti (black) [Bard et al., 1996]. (**C**) Greenland surface air temperature (SAT) based on Greenland Ice Sheet Project 2 (GISP2) δ^{18}O reconstruction with borehole temperature calibration [Cuffey and Clow, 1997]. (**D**) Antarctic SAT based on Dome C δD reconstruction [Jouzel et al., 2007]. (**E**) Pa/Th ratio at Bermuda Rise (core GGC5) as a proxy for AMOC export [McManus et al., 2004].
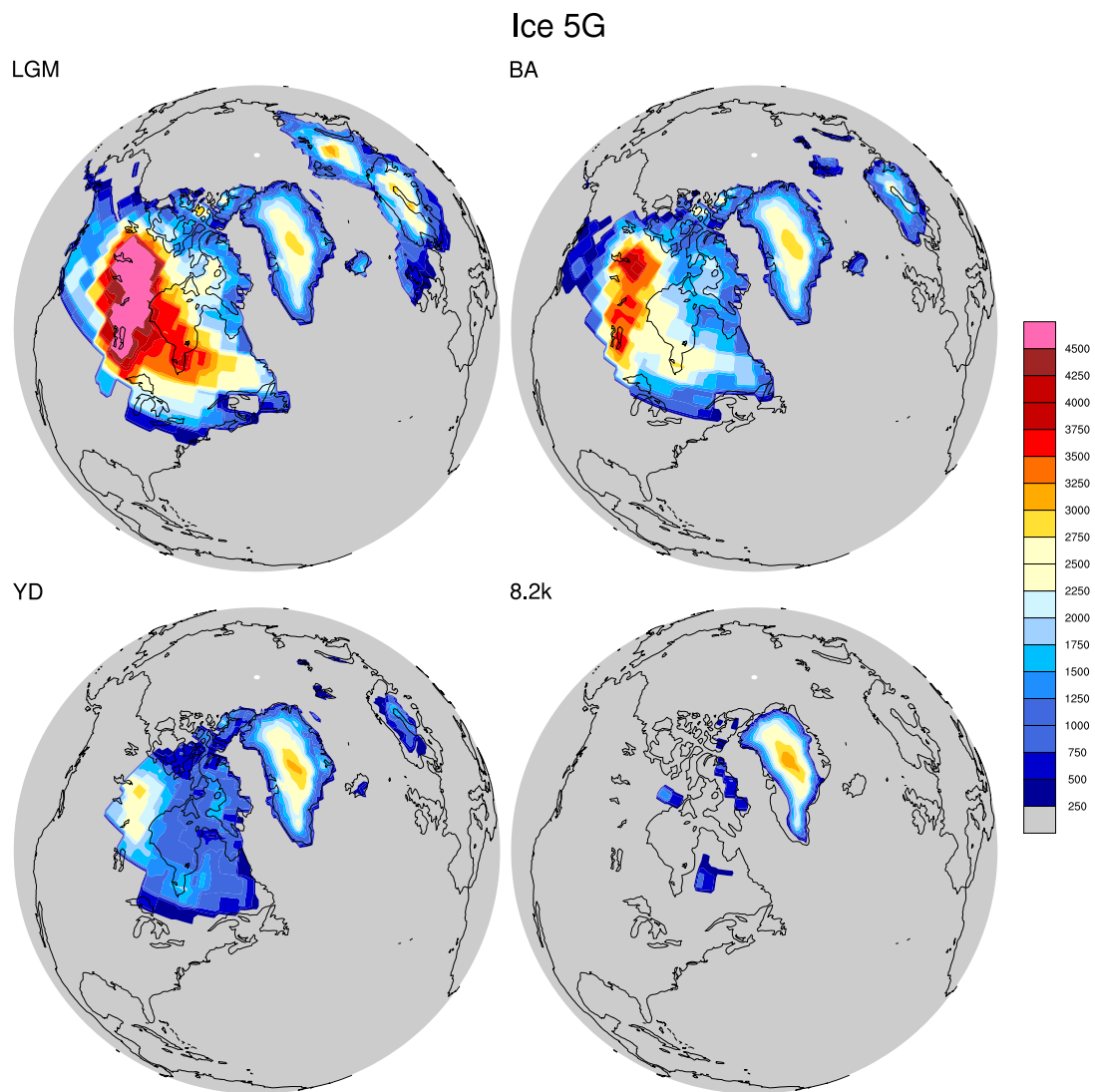
Figure 2: The height (in m) of the Northern Hemisphere Ice Sheet based on Ice5G reconstruction [Peltier, 2004] during the LGM (upper left), BA (upper right), YD (lower left) and 8.2 ka (lower right).

Chapter 2   TraCE-21K simulation

2.1   Introduction

The last deglaciation is one of the most dramatic natural climate warming events in the last 800,000 years. The abundance of paleoclimate proxy records during this period makes the last deglaciation an ideal case study of the transient response of the earth system to the abrupt increase of atmospheric CO_2 and the associated global warming. What is learned through this study sheds lights on the puzzles and challenges we are facing as a result of anthropogenic global warming due to the fossil fuel burning and deforestation.

The overall strategy of simulating the last deglaciation is to perform one of the best simulations that reproduce the paleoclimatic variations inferred from high-quality proxies, such as the SAT reconstructions from the polar ice cores. Challenged by the insufficient knowledge of meltwater discharge during the last deglaciation, I performed several sensitivity experiments with same initial condition but different rates or locations of meltwater discharges during several abrupt climate change events (Fig. 1): 19 ka, HS1, BA, YD events and early Holocene. I select the run that best resembles the proxy reconstructions to continue the transient simulation.

2.2   Model setup

The coupled atmosphere-ocean general circulation model (CGCM) employed is the Community Climate System Model version 3 (CCSM3), centered at the National Center for Atmospheric Research (NCAR). CCSM3 is a global, coupled ocean–atmosphere–sea ice–land surface climate model without flux adjustment [Collins et al., 2006]. All the simulations were

performed at T31_gx3v5 resolution [Yeager et al., 2006] and with a dynamic global vegetation module. The atmospheric model is the Community Atmospheric Model 3 (CAM3) with 26 hybrid coordinate levels in the vertical and ~3.75-degree resolution in the horizontal. The land model uses the same resolution as the atmosphere, and each grid box includes a hierarchy of land units, soil columns, and plant types. Glaciers, lakes, wetlands, urban areas, and vegetated regions can be specified in the land units. The ocean model is the NCAR implementation of the Parallel Ocean Program (POP) in vertical z-coordinate with 25 levels. The longitudinal resolution is 3.6-degree and the latitudinal resolution is variable, with finer resolution near the equator (~0.9 degrees). The sea ice model is the NCAR Community Sea Ice Model (CSIM), a dynamic-thermodynamic model that includes a subgrid-scale ice thickness distribution. The resolution of CSIM is identical to that of POP.

The preindustrial control simulation reproduces the major features of the global climate, notably in the deep ocean [Otto-Bliesner et al., 2006]. The LGM CCSM3 simulation has a global cooling of 4.5°C compared to the pre-industrial controls, with amplified cooling at high latitudes and over the continental ice sheets [Otto-Bliesner et al., 2006]. The LGM control run also simulates a shoaling of North Atlantic Deep Water (NADW) and farther northward penetration of Antarctic Bottom Water (AABW) [Otto-Bliesner et al., 2007]. A 1,800-year LGM equilibrium simulation was branched off from an earlier LGM simulation in order to incorporate the dynamic global vegetation model CLM-DGVM [Levis et al., 2004] and to reduce the model drift in the deep ocean. The transient simulation then started at the end of the 1,800-year LGM/CLM-DGVM equilibrium run with the transient orbital parameter starting at 22 ka. The transient concentrations of the GHGs (CO_2, CH_4 and N_2O) were adopted from Joos and Spahni [2008].

The height and extent of the continental ice sheets were modified approximately once per 500 years according to the ICE-5G reconstruction [Peltier, 2004]. The coastlines at the LGM were also taken from the ICE-5G reconstruction and were modified at 13.1 ka with the removal of the Fennoscandian Ice Sheet from the Barents Sea and at 12.9 ka with the opening of the Bering Strait. In the Holocene, the coastlines were modified at 7.6 ka with the opening of Hudson Bay. The last modification of the coastline occurred at 6.2 ka with the opening of the Indonesian throughflow, after which the transient simulation adopted the present-day coastlines (Table 1).

2.3   Meltwater forcing

One of the challenges of simulating the last deglaciation is the still-high uncertainty with respect to meltwater fluxes from retreating glaciers during the last deglaciation. On one hand, sea level records cannot constrain the location of meltwater fluxes, and on the other hand, there are also 5 to 15 m large uncertainties in the sea level reconstructions. In our transient simulation, I conducted sensitivity experiments with the meltwater forcing during millennial events, such as 19-ka, BA, mwp-1A, YD etc. The sensitivity experiments for each millennial event used the same initial condition, but different meltwater schemes in terms of the location and the rate of meltwater discharge. I chose the simulation to continue the transient simulation that best matched the proxy records of sea-level rise, AMOC and Greenland SAT. Several suites of sensitivity experiment will be discussed to show how I derive the meltwater flux for the simulation of TraCE-21K. For the results shown here, the meltwater scheme of DGL-A in Liu et al. [2009] is extended into the Holocene. Meltwater fluxes from the retreating ice sheets were derived from the record of sea level rise [Peltier, 2004; Clark and Mix, 2002] and geological indicators of ice sheet retreat and meltwater discharge [Clark et al., 2002; Clark et al., 2004; Licciardi et al., 1999;

Clark et al., 2001; Carlson et al., 2007; Carlson, 2008; Carlson et al., 2009; Clark et al., 2009; Carlson, 2009; Obbink et al., 2010]. The meltwater forcing during mwp-1A includes contributions from the Antarctic (15 m of equivalent sea-level volume) and Laurentide (5 m of equivalent sea-level volume) Ice Sheets [Clark et al., 2002; Bassett et al., 2005; Carlson, 2009]. Any larger (>5 m) Northern Hemisphere contribution results in a complete shutdown of AMOC and is inconsistent with proxy records [McManus et al., 2004; Stanford et al., 2006; Praetorius et al., 2008], which constrains the northern hemisphere's contribution to be <25 % of the total meltwater pulse volume (~20 m). We also adopted the sequence of freshwater discharge of Carlson et al. [2007] for the Younger Dryas.

In CCSM3, the meltwater discharge is added to the ocean model as a freshwater flux on the surface of the ocean. For the specific region, the intended freshwater flux is divided by the total area to get the unit freshwater flux to be added onto each grid point of the ocean model in that specific region during the transient simulation. The units for the meltwater discharge can be either m/kyr (meters of equivalent sea-level volume per thousand years) or Sv (1 Sv = 10^6 m^3 s^{-1}). Since the area of the ocean is about 3.61×10^{14} m^2, 1 m of the sea level rise per thousand years (m/kyr) means 3.61×10^{14} m^3 volume of meltwater in 10^3 years, which is 0.011 m3 s^{-1}, or 0.011 Sv.

2.4   TraCE-21K spin-up: the LGM simulation with CLM-DGVM

TraCE-21K was initialized from a low resolution (T31_gx3v5) LGM equilibrium simulation without dynamic vegetation [Otto-Bliesner et al., 2006]. For multi-millennial transient simulation, the vegetation feedback can be very significant due to its modification of the surface albedo, evapotranspiration, etc. [Peteet 2000; Horton et al., 2010]. Therefore I

included the dynamic global vegetation module CLM-DGVM [Levis et al., 2004] in TraCE-21K, which "allows vegetation cover and structure to be simulated instead of prescribed from data". In CLM-DGVM, "annual (or slow) processes include the update of vegetation biogeography and structure. The plant-atmosphere exchange of carbon (in the form of CO_2) occurs at a sub-hourly time step. Plant phenology is calculated daily". The dynamic vegetation module helps us compare the transient simulation directly with vegetation indicators, such as the pollen records. It also helps with the study of the ecological evolution during the last deglaciation. The equilibrium LGM simulation with CLM-DGVM was integrated for 1,800 years to reach the equilibrium.

2.5   TraCE-21K between LGM and 19 ka: the role of transient orbital forcing

The transient forcing of GHG and orbital variations spanning from 22 ka to 0 ka was turned on at the year 1,700 of the equilibrium LGM/CLM-DGVM simulation. Between 22 and 19 ka, all ice sheets were kept at the LGM condition (Table 2) and the change of GHGs is minimal (Fig. 11 A). As a result, the transient climate evolution during these 3,000 years is dominated by the orbital forcing (Fig. 2). The Northern Hemisphere and Tropics share similar features of the insolation changes, with the increase of insolation during the local spring and summer and the decrease of insolation during local fall and winter (Fig. 2 A1-A3). Furthermore, the insolation change is much larger during local spring and fall than local summer and winter: there is 11~14 W m^{-2} increase during local spring, but only less than 3 W m^{-2} increase during local summer; there is 7~12 W m^{-2} reduction during the local fall, but only less than 4 W m^{-2} during local winter. However, the response of SAT to the changes of the insolation shows non-linear responses in seasons: even though the increase of the local summer insolation is much less than local spring insolation, there are slightly larger changes in local summer SAT than in local

spring SAT in the Northern Hemisphere and Tropics (Fig. 2 A1-A3 vs. B1-B3). The spatial distribution of the SAT changes between 19 and 22 ka also shows larger warming during local summer than local spring, with over 3 $^{\circ}$C warming in Arctic and Eurasian in local summer versus less than 2 $^{\circ}$C warming in local spring (Fig. 3 A2 and A3). A similar non-linear response is also observed in local winter and fall, with larger SAT changes in local winter than local fall in Tropics and similar changes in local fall and local winter in Northern Hemisphere extratropical regions, despite the fact that the decrease of the local winter insolation is much less than that of local fall in these regions (Fig. 2 A1-A3 vs. B1-B3). The nonlinear response of the SAT to the seasonal insolation change can be attributed to the sea ice change in the Arctic and the snow change in Eurasian, which persists from the local spring/fall to the local summer/winter [Stott et al., 2007]. With the amplifications by the positive feedbacks from ice albedo and vegetation, the SAT changes can be much larger during local summer and winter than local spring and fall.

The changes of the insolation in southern hemisphere mid-latitude and polar regions are about half of the size of their Northern Hemisphere counterparts, with 5-7 W m^{-2} increase during local summer (DJF) and fall (MAM), and 7 W m^{-2} reductions during local spring (SON). As a result, the southern hemisphere mid-latitude is the region with the smallest SAT changes from 22 to 19 ka. In the Antarctic, SAT increases in all four seasons, amounting to ~0.5 $^{\circ}$C at 19 ka, with the warming during the warm seasons (SON and DJF) is slightly less than that from the cold season. In contrast, the warming of Northern Hemisphere polar region reaches 0.6 to 0.9 during the warm season (MAM and JJA). Overall, the largest warming at the end of the LGM, which amounts to over 3 $^{\circ}$C, is extensively located in Northern Hemisphere extratropical regions during the Northern Hemisphere summer (JJA) (Fig. 3). The largest warming in southern hemisphere

occurs during local fall (MAM), with mild warming (less than 2 ^{o}C) in the small fraction of the Southern Ocean around the Antarctica (Fig. 3). Our modeling results thus support the Milankovitch theory that the glacial-interglacial transition is triggered by the increase of the Northern Hemisphere summer insolation [Milankovitch, 1941]. For the case of the last deglaciation, our transient simulation demonstrates that the last deglaciation originates from Northern Hemisphere due to its larger increase of high latitude spring-summer insolation. The Northern Hemisphere warming is further enhanced by the larger proportion of land area, resulting in more widespread warming over the Northern Hemisphere than its southern hemisphere counterpart. The Northern Hemisphere summer warming at the end of the LGM in the transient simulation is consistent with the early retreat of the Scandinavian Ice Sheet [Clark et al., 2009] as well as the early reactivation of European rivers [Menot et al., 2006], which probably provided one of the first pulses of Northern Hemisphere meltwater (NHMW) at the onset of the last deglaciation. However, a more thorough test of the Milankovitch theory, with the full complexity of insolation, greenhouse gases and deglacial warming, needs to be performed using the next-generation climate models with both interactive ice sheet module and biogeochemical module.

2.6   The sensitivity of AMOC and Greenland temperature to meltwater forcing

2.6.1   The sensitivity to locations of meltwater forcing

Since both the location and the rate of the meltwater discharge have substantial uncertainties during the last deglaciation, I need to derive the meltwater forcing based on the reconstructions of its impact on climate. In this regards, I use the reconstructions of Greenland SAT [Cuffey and Clow, 1997], the AMOC [McManus et al., 2004] and the sea level rise [Peltier, 2004; Clark and Mix, 2002; Clark et al., 2009] as the main constraints for the meltwater forcing,

with further constraints from geological indicators of ice sheet retreat and meltwater discharge [Clark et al., 2002; Clark et al., 2004; Licciardi et al., 1999; Clark et al., 2001; Carlson et al., 2007; Carlson, 2008; Carlson et al., 2009; Clark et al., 2009; Carlson, 2009; Obbink et al., 2010].

In order to translate the climate impacts into the meltwater forcing, I need to know the sensitivity of the AMOC and Greenland SAT to the location and magnitude of meltwater forcing (Figs. 4 and 5). In this study, I consider eight locations for meltwater discharge (Fig. 4B and Table 3). With 0.1 Sv (Sv, Sverdrup. 1 Sv = 10^6 m^3 s^{-1}) meltwater forcing during the LGM, the Beaufort Sea/Mackenzie River discharge, Nordic Sea, and 50-70° N of North Atlantic are the three regions with the largest sensitivity among the eight study regions. In less than 300 years, the AMOCs with 0.1 Sv meltwater forcing in these three regions reduce by over 50% from 12.5 to 6 Sv. When meltwater is discharged from St. Lawrence River, the AMOC reduces by 44% from 12.5 to 7 Sv. Meltwater discharge into Gulf of Mexico can reduce AMOC by 36% from 12.5 to 8 Sv. The sensitivity of AMOC to the meltwater discharge is very small in the Southern Ocean, with less than 1 Sv AMOC reduction forced by the 0.1 Sv meltwater discharge in either Ross Sea or Weddell Sea.

The lower sensitivity of AMOC to Southern Ocean meltwater forcing is consistent with the results from other Coupled General Circulation Model (CGCM) [Stouffer et al., 2007; Seidov et al., 2005], but inconsistent with the results from Ocean General Circulation Models (OGCM) and EMICs (Earth system Model of Intermediate Complexity) [Seidov et al., 2001; Weaver et al., 2003], which found that a Southern Ocean meltwater forcing can result in the strengthening of AMOC. The evolution of the upper ocean salinity anomaly is responsible for the different responses to the Southern Ocean meltwater forcing [Seidov et al., 2005]. In OGCM and EMICs,

the low salinity anomaly is prescribed in the Southern Ocean as the boundary condition for the ocean model. Therefore, the results from OGCM and EMICs are essentially the equilibrium solution with unlimited freshwater forcing. While in CCSM3 and other CGCMs, the low salinity anomaly results from the freshwater discharge and therefore can spread freely in the global ocean. When this low salinity anomaly reaches the North Atlantic Ocean, it slows down the AMOC. In this respect, the evolution of the upper ocean salinity anomaly in CGCMs is more suitable for the transient simulation of the response of climate system to the meltwater discharge from ice sheet retreats during the last deglaciation. However, the CGCM (NCAR-CCSM3) employed in TraCE-21K cannot simulate the sudden resumption of AMOC at the onset of BA via the Antarctic meltwater discharge during mwp-1A [Weaver et al., 2003]. A new mechanism for the BA warming needs to be explored.

In the Gulf of Mexico, the meltwater discharge through the Mississippi River is less effective than that from the more northerly sources, e.g. the 50-70°N of the North Atlantic. The higher sensitivity of AMOC to the high latitude meltwater forcing is consistent with the results from high-resolution (T42_gx1) NCAR-CCSM3 [Otto-Bliesner and Brady, 2010], but is in disagreement with the EMIC result from CLIMBER-3a [Goelzer et al., 2006], which found larger sensitivity of the AMOC to meltwater discharge in the Tropics than high latitude North Atlantic. The reason for this difference is unclear.

The eight study regions display a general trend of lower sensitivity of AMOC to the meltwater forcing in more southerly latitudes. The dependence of the AMOC sensitivity on the locations of meltwater discharge supports the hypothesis that changes in meltwater routing may be the mechanism for the abrupt climate change, such as that during YD. Recent studies have

reported the evidence of YD meltwater discharge from the Laurentide Ice Sheet to both the east via the St. Lawrence River [Carlson et al., 2007] and the north via the Mackenzie River [Murton et al., 2010]. The sensitivity result in CCSM3 does not resolve this discrepancy but suggests that the north route is more effective in slowing down the AMOC.

The sensitivity of SAT to the location of the meltwater forcing is generally similar to the AMOC, with low sensitivity to the meltwater forcing in the Southern Ocean, intermediate sensitivity in the Gulf of the Mexico and St. Lawrence River and high sensitivity in the Arctic, Nordic Sea and 50-70° N of the North Atlantic (Fig. 5). The SAT sensitivity differences between the meltwater forcing of Gulf of the Mexico and St. Lawrence River is quite small, which suggests that rerouting meltwater from the Gulf of the Mexico to St. Lawrence River [Broecker et al., 1989] is not capable of producing abrupt climate changes. Over Greenland, 0.1 Sv meltwater forcing in Southern Ocean, Tropics/St. Lawrence River and high latitude regions results in the reduction of SATs of 0, 3.5, 5.0 ^{o}C. For Northern Hemisphere and global average temperatures, the reduction of the SAT is 0.12, 0.9, 1.2 and 0.1, 0.35, 0.40 in the low, intermediate and high sensitivity regions, respectively.

2.6.2   The sensitivity to magnitudes of meltwater forcing

In order to translate the climate impacts into the meltwater forcing, I also need to know the sensitivity of the AMOC and Greenland SAT to the magnitude of meltwater forcing. I choose 3, 9 and 33 m/kyr (1m/kyr = 0.0115 Sv; 1m/kyr refers to 1 meter of equivalent global sea level rise per thousand year) as the three scenarios of meltwater discharge in 50-70° N of the North Atlantic. Based on the estimate of 120~135 m of sea level rose between 19 and 6 ka, the average rate of sea level rise through the last deglaciation was 9 m/kyr (~0.1 Sv). On the other hand, the

sea level rise at the rate of 33 m/kyr approximates the rate of the sea level rise during the abrupt sea level rise events, such as the 19ka event and the meltwater pulse la (mwp-1A): during the 19ka event, sea level rose 10~15 m in 100~500 years [Clark et al., 2004], and in mwp-1A, sea level rose 20 m in 300~500 years [Fairbanks, 1989]. We use 3 m/kyr freshwater forcing as the representative for scenarios with weak meltwater discharge.

AMOC reduces by 1.5 (12%), 6.5 (52%) and 10 Sv (80%) and Greenland SAT drops by 1, 5 and 7 $^{\circ}$C with the small, intermediate and large magnitude of the meltwater forcing (Fig. 6). There appears to be a quasi-linear relationship between the drop of the AMOC and the reduction of the SAT over the Summit Greenland (see section **2.9.3**). It takes 200 to 300 years for the AMOC to reach equilibrium, and similar adjustment time is also found in the sensitivity runs for the study regions in the Northern Hemisphere (Fig. 4). At the LGM, the AMOC streamfunction (a function of latitude and depth for volume transport of the zonally averaged flow) shows that over 12-Sv clockwise circulation is associated with the NADW in the top two kilometers and over 6 Sv anti-clockwise circulation is associated with AABW below two kilometers (Fig. 7). The 3 m/kyr meltwater forcing doesn't change the pattern of the AMOC streamfunction, but the 9 m/kyr forcing shoals the circulation of NADW by ~300 meters. The 33m/kyr forcing induces a near-total collapse of AMOC, with only 2 Sv circulation of NADW confined between 600 and 1600 meters below surface. Note that there is also a significant reduction in AABW (negative value between 2 and 5 km in Fig. 7) in the 33m/kyr scenario, presumably due to the meltwater transport from the North Atlantic to the Southern Ocean.

2.7   TraCE-21K simulation of H1

The AMOC reconstruction [McManus et al., 2004] suggests AMOC started to decrease at ~19 ka and reached the near-collapse state during Heinrich event 1 (H1) at ~17 ka. In the sensitivity experiment (Fig. 6), AMOC collapses with the meltwater forcing between 9 and 33m/kyr. In TraCE-21K, I adopted the following plausible meltwater discharge scheme (TraCE-H1 in Table 4): a constant 3m/kyr meltwater goes into the North Atlantic between 19.0 and 18.4 ka. Between 18.5 and 17.5 ka, the total meltwater discharge ramps up to 10 m/kyr, with the North Atlantic and Gulf of Mexico each sharing half of the discharge. Between 17.5 and 17 ka, meltwater in the North Atlantic is increased from 5 to 15m/kyr (Fig. 8). With this scheme, the total sea level rise between 19 and 17 ka in TraCE-21K amounts to 15 m, in agreement with the 17 ± 5 m estimate from sea level reconstructions [Yokoyama et al., 2000]. With a total rate of 20m/kyr NHMW discharge by 17 ka, AMOC in the model decreases to ~3 Sv, close to the minimum AMOC of 2.5 Sv found in the experiment with 33m/kyr NHMW. With the reduction of AMOC from the LGM level to the near-collapse state at H1, the simulated Greenland SAT drops 5.5 ^{o}C within 2,000 years, agreeing with the GISP2 SAT reconstruction and suggesting that the model has good regional climate sensitivity in Greenland during HS1.

Because of the fast adjustment of AMOC to the meltwater forcing, our model has difficulty in reconciling a scenario of abrupt sea level rise caused by 19-ka NHMW discharge with the observed trends in AMOC and Greenland SAT between 19 and 17 ka. In the sensitivity experiment DGL-19ka simulation (blue lines in Fig. 8), the imposition of an instantaneous meltwater pulse of 33 m/kyr at 19 ka induces a near-total collapse of AMOC at 18.7 ka and a 7-degree plummet of the Greenland SAT around 18.7 ka. Both the simulated reductions of AMOC

and Greenland SAT under the scenario of abrupt NHMW discharge at 19 ka are at least 1,000 years earlier than the corresponding observations [Cuffey and Clow, 1997; McManus et al., 2004] (Fig. 8 B and C). There are four possible reasons for the inconsistency between the 19 ka sea level rise and our simulations. First, the sensitivity of the AMOC to the meltwater forcing in 50-70°N of the North Atlantic might be too high in the model. Second, the meltwater discharge might go to other regions in the Northern Hemisphere with less impact on the AMOC. Third, there might be a non-linear relationship between AMOC and the rate of the sea level rise that is not captured by the model. Fourth, the meltwater discharge for the 19 ka abrupt sea level rise might come from the melting of the Antarctic.

2.8   AMOC hysteresis

The proxy data suggest that the AMOC stayed in a state of near-collapse between the H1 and the onset of the BA, while Greenland SAT returned to the LGM level during the cooling following H1 (Fig. 8). At the onset of the BA, AMOC abruptly recovered to the LGM level and Summit Greenland experienced one of the most abrupt climate changes during the last deglaciation, with SAT abruptly increasing by ~13 $^{\circ}$C in less than 150 years. According to box model and EMIC simulations, the abrupt changes of the AMOC can be attributed to a hysteresis behavior that involves multiple equilibriums, thresholds, and nonlinear responses to the meltwater discharges [Stommel, 1961; Stocker and Marchal, 2000; Rahmstorf et al., 2005]. Under this conceptual framework, even a smooth meltwater forcing can cause the AMOC to change abruptly from one equilibrium to another if thresholds are passed. An earlier modeling study with EMIC has suggested that the continuation of the 2,000-year near-collapse state followed by the sudden resumption of AMOC at the BA onset can be attributed to the hysteresis

of AMOC [Weaver et al., 2003]. In this study, the near-collapse of the AMOC at ~17 ka pushes AMOC into a new stable state, where it remains even when the meltwater in the North Atlantic is totally switched off. For this particular EMIC model, the threshold of AMOC hysteresis can only be reached by further increase of the northward density gradient. Weaver et al. [2003] managed to increase the northward density gradient by freshwater flux discharge into the Southern Ocean, which eventually push the northward density gradient to pass the threshold of AMOC hysteresis and trigger the sudden resumption of AMOC at the onset of BA. One advantage of invoking AMOC hysteresis between H1 and the onset of BA is to reconcile the AMOC and sea level reconstructions during this period. Between H1 and the onset of BA, sea level plateaued, suggesting minimal meltwater discharge during this period, yet AMOC did not recover during this time period (Fig. 8). The hysteresis of AMOC can provide a plausible solution to maintain the near-collapse state of the AMOC between 17 and 15 ka. However, the hysteresis structure is highly model-dependent [Manabe and Stouffer, 1999]. Furthermore, current state-of-art global climate models fail to exhibit hysteresis behavior and multi-equilibriums [Stouffer et al., 2006; Yin and Stouffer, 2007], leaving open the question whether hysteresis is a fundamental feature of the real-world AMOC as suggested by EMICs, or not as suggested in current CGCMs [Liu et al., 2009].

I performed four sensitivity experiments (Table 5) at 17 ka to find the optimal meltwater discharge to keep AMOC in the near-collapsed state (Fig. 9). In DGL-17ka-A, meltwater ramps up from 20 to 40 m/kyr between 17 and 16 ka. The doubling of the meltwater forcing results in 1.5 Sv reduction of the AMOC from 3.5 Sv to 2.0 Sv, suggesting that the impact of meltwater discharge on the reduction of the AMOC already saturates at the level of 20 m/kyr. In DGL-

17ka-B, meltwater ramps down from 20 to 12.5 m/kyr between 17 and 16 ka. AMOC drops ~0.5 Sv in the first few hundred years before it starts to slowly increase due to the reduction of the meltwater forcing. In DGL-17ka-C, the meltwater in the Gulf of the Mexico is switched off at 17 ka, leaving 15 m/kyr meltwater discharge in the North Atlantic as the only NHMW. AMOC increases by a few tens Sv, and stays in the near-collapsed state between 17 and 16 ka in this scheme. DGL-17ka-C suggests 15m/kyr NHMW discharge in the North Atlantic is capable of keeping AMOC in the near-collapse state. In DGL-17ka-D, NHMW discharge reduces by 10 m/kyr at 17 ka, with the switch-off of the 5m/kyr meltwater from the Gulf of the Mexico and another 5m/kyr reduction in the North Atlantic. AMOC increases quickly from 3.5 Sv to 5.5 Sv in 300 years, suggesting that 10m/kyr NHMW discharge is not sufficient to keep the AMOC in the near-collapsed state. In all cases, the Greenland summit temperature reverses the cooling trend since 19 ka and starts to rise at 17 ka, presumably as the result of the deglacial rise of the atmospheric CO_2 (Fig. 11 A).

Because the reduction of AMOC saturates around 15 m/kyr, the meltwater forcing of 40m/kyr is more than adequate to keep AMOC in its minimum level within the range of reasonable NHMW. If the AMOC in CCSM3 has hysteresis, the 40m/kyr NHMW discharge should have switched the AMOC from the "active" to the "off" mode, and the AMOC can maintain the "off" mode as long as the reduction of the NHMW does not pass the threshold. Two sensitivity experiments (Fig. 10 and Table 5) were performed to test the hypothesized threshold value. In DGL-16ka-A and DGL-16ka-B, NHMW discharge reduces from 40 m/kyr to 0 and 10 m/kyr, respectively. In both cases, the reduction of the NHMW results in the immediate rebound of the AMOC, with 2 Sv increase of the AMOC in 100 years in DGL-16ka-A and 1.5 Sv

increase in 300 years in DGL-16ka-B. The increase of Greenland SAT in both cases is not substantial, but might get larger if both sensitivity experiments are extended further. The quick rebounds of AMOC under 0 and 10 m/kyr NHMW discharge suggest either there is no hysteresis in CCSM3, or the threshold for hysteresis is higher than 10m/kyr. In either situation, CCSM3 cannot keep AMOC in near-collapsed state between H1 and BA without inducing substantial sea level rise.

2.9   TraCE-21K simulation between H1 and BA

Based on the responses of AMOC to the different magnitude of meltwater forcing in the four sensitivity experiments, I opted to use two meltwater schemes for TraCE-21K between H1 and BA (Fig. 11). The first scheme (TraCE-BA, same as DGL_A in Liu et al. [2009]) is the extension of DGL-17ka-C with 15m/kyr meltwater discharge in the North Atlantic (Tables 4 and 5). The meltwater discharge switches off at 14.67 ka to set off the abrupt resumption of the AMOC at the onset of BA. In the second scheme (DGL-H1-BA), the 20m/kyr meltwater discharge in both the North Atlantic and Gulf of Mexico ramps down to 0 m/kyr between 17 and 14.2 ka (Table 5). On average, the magnitude of NHMW discharge in DGL-H1-BA is 10m/kyr, which is 5m/kyr weaker than that from TraCE-BA. As a result, the sea level rise in DGL-H1-BA is more than 10 m smaller than that in TraCE-BA between H1 and the onset of BA (Fig. 11).

Atmospheric CO_2 increased by 35 ppmv from 190 to 225 ppmv between H1 and BA, which is half of the deglacial CO_2 rise during the last deglaciation, when atmospheric CO_2 increased from 190 ppmv to 260 ppmv between the LGM and early Holocene. The CO_2 rise accounts for most of the ~3.5 ^{o}C increase of the Greenland SAT from -48.5 to -45 ^{o}C in TraCE-BA between H1 and BA, in which AMOC is kept in the off mode (Fig. 11).

2.9.1 The AMOC overshoot

In TraCE-BA, AMOC stays in the near-collapsed mode between H1 and BA, consistent with the AMOC reconstruction. Immediately after the switch-off of the meltwater discharge at the onset of the BA (14.67 ka), AMOC starts to rebound (Fig. 11 and 13). In ~350 years, AMOC increases from 3 to 19 Sv. The recovery of the AMOC occurs in two stages [Renold et al., 2010], with full recovery of AMOC to the LGM level in the first stage and the overshoot of AMOC in the second stage (red in Fig. 13 B). The overshoot of the AMOC is defined as the increased strength of the AMOC that is over the LGM level (~12.5 Sv). The rate of the AMOC recovery in the first stage has a good agreement with the AMOC reconstruction using ^{231}Pa/^{230}Th [McManus et al., 2004] (red in Fig. 13 B). At the onset of BA, the simulated Greenland SAT increases abruptly as a result of the rapid resumption of the AMOC. In ~350 years, it increases by ~13 $^{\circ}$C from -45 to -32 $^{\circ}$C, and exhibits excellent agreement with the SAT reconstructions in terms of the amplitude of the abrupt warming (red in Fig. 13 C). However, the rate of the simulated Greenland warming is about 40% slower than that from the reconstruction, which shows the abrupt warming over Greenland occurred in ~200 years.

The overshoot of the AMOC at the onset of the BA is not recorded in AMOC reconstruction using ^{231}Pa/^{230}Th at a site near Bermuda Rise in the deep western subtropical Atlantic [McManus et al., 2004], but is recorded in the flow speed reconstruction of the NADW through grain size distribution near Eirik Drift south of the Greenland [Stanford et al., 2006]. The two records may be discrepant because the resolution of the grain size record during BA is higher than the ^{231}Pa/^{230}Th record, which possibly misses the overshoot signal at the onset of BA.

Alternatively, the overshoot of AMOC might be restricted to the high-latitudes, and so is only recorded in high latitude proxies.

The AMOC overshoot is further investigated in another three sensitivity experiments, DGL-Overshoot-A, DGL-Overshoot-B and DGL-Overshoot-C (Figs. 12, 13 and Table 5) to shed light on the processes that control its magnitude as well as the abruptness. DGL-Overshoot-C is the extension of the BA simulation of TraCE-21K (TraCE-BA) from 14.35 to 13.0 ka to show the results from AMOC overshoot to its final equilibrium state. DGL-Overshoot-A and DGL-Overshoot-B are similar to DGL-Overshoot-C, but the collapse and overshoot of the AMOC started ~4,000 and ~2,000 years earlier than DGL-Overshoot-C (Fig. 12). In all of the above sensitivity experiments, the sudden switch-off of the meltwater discharge induces rapid resumption of the AMOC and abrupt increase of the Greenland SAT. In addition, AMOCs in all three cases overshoot the LGM level at the peak of the resumption. After the overshoot, AMOC starts to decrease and takes between 500 and 100 years to reach equilibrium. The final AMOC equilibrium is the same as the LGM in DGL-Overshoot-A, but significantly stronger in DGL-Overshoot-B and DGL-Overshoot-C. The reason for the different equilibriums is presumably due to deglacial atmosphere CO_2 forcing, which is at the LGM level in DGL-Overshoot-A, but significantly stronger in the other two experiments.

Greenland SAT increases abruptly when AMOC recovers in the three sensitivity experiments (Figs. 12 and 13). Only in DGL-Overshoot-C does the simulated Greenland SAT achieve the level of the warming recorded in reconstructions. The other two experiments fail to reach the level of warming mainly because of the lack of the precondition of the deglacial CO_2

rise before the abrupt warming, which amounts to 3~5 ^{o}C warming between H1 and the onset of BA in TraCE-BA and DGL-Overshoot-C (Fig. 11 D and Fig. 12 C).

In order to compare the amplitude and the rate of overshoot in the three cases, I line up the simulation results in DGL-Overshoot-A and DGL-Overshoot-B with that in DGL-Overshoot-C, such that the onset of the AMOC and SAT resumption occurs at the same time (Fig. 13). Due to the increase of the CO_2, the simulated SAT also needs to be increased by ~5 ^{o}C for the resumption to start with the same initial value. It takes 390, 500 and 550 years for the AMOCs to reach maximum of 19, 17.5 and 17 Sv in the three sensitivity runs. Given the LGM AMOC strength of 12.5 Sv, the overshoot of AMOC is 6.5, 5.0 and 4.5 Sv, or 52%, 40% and 36% of the LGM strength. This result suggests that the rate and the final amplitude of the AMOC resumption is dependent on the history of the meltwater forcing, with faster recovery and larger AMOC overshoot in the simulations that undergo longer meltwater forcing. Compared with the AMOC in DGL-Overshoot-A, the faster recovery and larger overshoot in DGL-Overshoot-B and DGL-Overshoot-C might result from the following two reasons. First, the magnitude of deep and subsurface ocean warming increases along with meltwater forcing (see section 3.4). With larger warming of the subsurface ocean, the stability of the water column reduces and is prone to deeper convection than before. The intensified convection results in a larger overshoot for DGL-Overshoot-B and DGL-Overshoot-C. Secondly, the longer meltwater forcing in DGL-Overshoot-B and DGL-Overshoot-C is also accompanied by the increase of the atmospheric CO_2 and higher temperatures, which results in the sea ice retreats in the North Atlantic and Nordic Sea and exposes water surfaces that is prone to open ocean convections. With more locations for deep ocean convection, AMOC overshoots its LGM value after the meltwater discharge disappears.

After the switch-off of the meltwater flux, the warming of the Greenland SAT reaches 11, 12 and 13 ^{o}C when the AMOC overshoots reach the maximum in the three sensitivity experiments. The 13 ^{o}C warming in TraCE-BA/DGL-Overshoot-C is consistent with GISP2 Greenland SAT reconstruction. In TraCE-BA/DGL-Overshoot-C, 7 ^{o}C warming occurs during the stage of AMOC recovery and 6 ^{o}C warming occurs during AMOC overshoot, suggesting the AMOC overshoot is as important as AMOC recovery in CCSM3 in simulating the abrupt warming of Greenland SAT on the onset of BA warming.

2.9.2   The AMOC hysteresis loop between 19ka and BA

In TraCE-21K, the ramped increase of meltwater forcing between 19 ka and H1, together with the ramped reduction of meltwater forcing in the second scheme (DGL-H1-BA, see Table 5) for the simulation between H1 and BA, forms the forcing for the investigation of the hysteresis of AMOC. Between H1 and BA, the meltwater reduces from 20 to 0 m/kyr in 2800 model years, which is equivalent to the ramped reduction of meltwater forcing of 0.08 Sv per 1,000 years. Compared with the EMIC study [Rahmstorf et al., 2005], which uses the ramped reduction of meltwater forcing of 0.05 Sv per 1,000 model years, the ramped forcing in our simulation is 60% faster. I argue that the faster reduction of the meltwater is more appropriate in TraCE-21K, because it is consistent with AMOC reconstruction between H1 and BA.

The recovery of simulated AMOC in DGL-H1-BA (Fig. 11, blue) is not linearly dependent on the ramped reduction of the meltwater forcing, and exhibits two stages of abrupt

increases at 15.4 ka with ~10m/kyr meltwater forcing and at 14.6 ka with ~3m/kyr meltwater forcing. Between 17 and 15.4 ka, the simulated AMOC recovers slowly and the modeled Greenland SAT isn't substantially different from that in TraCE-BA (red in Fig. 11). The abrupt increase of the simulated AMOC at 15.4 ka in DGL-H1-BA results in the divergence of AMOC and SAT simulation between TraCE-BA and DGL-H1-BA. It is unexpected that the divergence between TraCE-BA and DGL-H1-BA disappears at 14.6 ka, when the trajectory of the simulated AMOC and SAT in DGL-H1-BA crosses that in TraCE-BA. It is even more surprising that the simulated AMOC and SAT in DGL-H1-BA increase abruptly at the onset of the BA, similar to that in TraCE-BA. The overshoot of simulated AMOC in DGL-H1-BA is about 1.5 Sv smaller than that in TraCE-BA, and the simulated warming of the Greenland summit is 1 degree weaker in DGL-H1-BA as well.

The recovery of AMOC to the ramped meltwater forcing was also investigated in another sensitivity experiment DGL-H1-BA-2 with larger rate of meltwater reduction (Fig. 14). Similar to DGL-H1-BA, the simulated AMOC and Greenland SAT abruptly increase when meltwater discharges reduce to 10 m/kyr, suggesting that 10 m/kyr freshwater forcing might be a threshold for AMOC in CCSM3. But there is no second abrupt increase of AMOC and Greenland SAT in DGL-H1-BA. As a result, AMOC and SAT almost increase linearly with the reduction of the meltwater after 10 m/kyr. When the meltwater fades away, the AMOC in DGL-H1-BA-2 reaches 17.5 Sv, similar to that in DGL-H1-BA. However, the maximum of Greenland SAT in DGL-H1-BA-2 is ~2 ^{o}C smaller than DGL-H1-BA, presumably due to the smaller deglacial CO_2 rise in DGL-H1-BA-2.

The hysteresis curves between AMOC and meltwater in DGL-H1-BA and DGL-H1-BA-2 confirm that CCSM3 shows only a weak hysteresis (Fig. 15). In both cases, AMOC decreases almost linearly with the increase of the meltwater forcing before AMOC reaches its minimum. In DGL-H1-BA-2, when AMOC reduces to its minimum of ~3 Sv, the response of AMOC to meltwater forcing saturates, and stays at ~3 Sv even though meltwater keeps increasing. Compared with the hysteresis curve from EMIC studies [Rahmstorf et al., 2005], the hysteresis curve in CCSM3 lacks the abrupt reduction of AMOC when the increase of the meltwater forcing exceeds certain threshold.

Although the simulated response of AMOC to the reduction of the meltwater forcing shows only weak hysteresis, it is nonlinear. Both hysteresis curves exhibit abrupt increase of AMOC when meltwater forcing drops below 10 m/kyr or 0.11 Sv. In addition, when meltwater is fading away, there is also another abrupt increase of AMOC that is found only in the case with slower meltwater reduction. Compared with the hysteresis curve from EMIC studies [Rahmstorf et al., 2005], the CCSM3 hysteresis curve with meltwater forcing larger than 10 m/kyr suggests CCSM3 does have double equilibriums, with abrupt transition occurring during the phase of AMOC increase. However, the double equilibriums in AMOC with meltwater forcing larger than 10 m/kyr have negligible effect on Greenland SAT, which exhibit single equilibrium with meltwater forcing larger than 10 m/kyr (Fig. 16). The abrupt increase of AMOC at 10m/kyr of meltwater forcing causes abrupt warming of Greenland SAT in both cases, with further abrupt warming near the end of the meltwater forcing in the slow meltwater reduction case.

2.9.3 The convective instability and abrupt AMOC changes

I attribute the abrupt increase of AMOC at 10 m/kyr of meltwater forcing to convective instability, which is caused by the positive feedbacks that make convection self-sustaining once it has been established [Rahmstorf, 1995]. One of the positive feedbacks is the sea ice-open ocean convection feedback. Sea ice acts as the insulator between the polar cold air and the sea water, which prevents the surface ocean from becoming cold and dense as a result of heat exchange with the polar cold air. The retreat of the sea ice exposes new surface ocean that is prone to open ocean convection. The convection of the ocean increases the strength of AMOC and polarward heat transport that induces further sea ice retreat. The hysteresis curve between sea ice and meltwater forcing in DGL-H1-BA shows that the first abrupt increase of AMOC is solely associated with the abrupt reduction of the sea ice in North Atlantic region, while the second abrupt increase of the AMOC is solely associated with the abrupt sea ice reduction in the Nordic Sea (Fig. 17). In other words, the two-step recovery of AMOC is associated with two-step sea ice retreats, with sea ice retreat occurring first at the North Atlantic region and later in the Nordic Sea. The regional dependence of the AMOC recovery provides further support that the convective instability rather than the "Stommel" conveyor hysteresis [Stommel, 1961; Rahmstorf, 1995] is responsible for the abrupt increase of the AMOC under linearly varying meltwater forcing.

The hysteresis curve between AMOC and Greenland SAT shows there is strong linear dependence of Greenland SAT on the strength of AMOC (Fig. 18), which provides support that the variability of AMOC is the dominant control on deglacial variations in Greenland SAT. In both cases, there are two linear relationships between AMOC and Greenland SAT. When

meltwater is increasing, the relationship between Greenland SAT and AMOC in both cases can be expressed as

$$SAT_{Greenland\ summit} = 0.6 * AMOC - 46 \qquad (eq.1)$$

And during the phase of the meltwater reduction, the relationship becomes as

$$SAT_{Greenland\ summit} = 1.1 * AMOC - 47 \qquad (eq.2)$$

$$SAT_{Greenland\ summit} = 0.9 * AMOC - 46 \qquad (eq.3)$$

in the slow and fast meltwater reduction case, respectively. The differences between the relationships in the meltwater reduction and increase phase presumably result from the CO_2 rise during the phase of meltwater reduction, with orbital forcing playing a less important role.

2.10   TraCE-21K simulation of mwp-1A

The most rapid sea level rise during last deglaciation occurred during mwp-1A, when the global sea level rose by ~20 m in less than 500 years [Weaver et al., 2003]. Because sea level data alone does not constrain the location of the meltwater, it is still under debate whether mwp-1A originates from northern or southern hemisphere [Clark et al., 2002; Carlson, 2009; Weaver et al., 2003; Fairbanks, 1989; Peltier, 1994; Clark et al., 1996; Bassett et al., 2005]. Given that TraCE-21K has a reasonable simulation of BA, it is valuable in TraCE-21K to investigate whether northern versus southern sources of mwp-1A have different impacts on the AMOC and Greenland temperature.

Four sensitivity experiments are performed with the same initial condition, but different rates and locations of meltwater forcing (Fig. 19 and Table 5). DGL-Overshoot-C serves as a control run for mwp-1A, in which I did not impose any meltwater after BA to investigate the climate evolution without mwp-1A. In DGL-mwp-1A-A, all of the meltwater during the mwp-1A is sourced from Northern Hemisphere with the duration of 300 years. In DGL-mwp-1A-B and DGL-mwp-1A-C, all of the meltwater during the mwp-1A is sourced from southern hemisphere with the duration of either 100 years or 300 years.

Without mwp-1A, the simulated AMOC in DGL-Overshoot-A gradually gets back from the BA overshoot to the level during the LGM, but still becomes 2 Sv stronger when AMOC approaches equilibrium 1,300 years after the overshoot during BA. The simulated Greenland SAT also gradually reduces by 2 ^{o}C from BA warming, and is 8.5 ^{o}C warmer than the LGM at the end of BA period. Compared with proxy records, the scenario with no mwp-1A is in good agreement with AMOC reconstruction from GGC5 [McManus et al., 2004]. However, this scenario cannot simulate the Older Dryas cooling recorded in Greenland.

With mwp-1A solely sourced from the Northern Hemisphere, the simulated AMOC in DGL-mwp-1A-A rapidly reduced by 15 Sv from the BA overshoot to the level of 2.5 Sv, even weaker than the level during H1 (3.5 Sv). The simulated Greenland SAT quickly drops by 9 ^{o}C, following closely with the relationship between AMOC and Greenland SAT in eq. 1 during the phase of AMOC reduction. Compared with the proxy record, the scenario with all of mwp-1A sourced from Northern Hemisphere has a good agreement with Older Dryas cooling recorded in Greenland, but cannot simulate the vigorous AMOC recorded from GGC5 [McManus et al., 2004]. Alternatively, the Pa/Th record at GGC5 might miss the rapid change of the AMOC

during Older Dryas due to the response time of Pa/Th to AMOC changes as well as its lower resolution during this period.

With mwp-1A solely sourced from southern hemisphere with a duration of 100 years, the simulated AMOC and Greenland SAT in DGL-mwp-1A-B exhibits similar transient evolution as that with mwp-1A solely sourced from the Northern Hemisphere. The simulated AMOC rapidly reduces by 16 Sv from the BA overshoot to the level of 3.0 Sv. The simulated Greenland SAT quickly drops by 10 $^{\circ}$C. Because it takes time for the meltwater to transport from the southern hemisphere to the North Atlantic to slow down the AMOC, the onset of the AMOC is delayed in these two experiments. However, both experiments exhibit similar rate of the AMOC and Greenland SAT reduction after the meltwater from the Southern Ocean reaches the North Atlantic [Seidov et al., 2005]. Because the duration of the meltwater discharge in DGL-mwp-1A-B is only 100 years, AMOC quickly recovers after the meltwater in the Southern Ocean switches off, which induces the warming of the Greenland that mimics the rebound of the reconstructed Greenland SAT at the end of the Older Dryas.

The response of the AMOC and Greenland SAT to the meltwater discharge in the Antarctic strongly depends on the rate of meltwater input. With the same 20 m mwp-1A solely from southern hemisphere, but with the duration of 300 years, the reduction of simulated AMOC and Greenland SAT is only about 50% of its counterpart with meltwater solely from the Northern Hemisphere in DGL-mwp-1A-A. Notice that the reduction of AMOC to the Southern Ocean meltwater forcing is much larger in DGL-mwp-1A-B and DGL-mwp-1A-C than that in Fig. 4, which is due to the fact that the magnitude of the meltwater discharge is 2.3 Sv and 0.76

Sv in DGL-mwp-1A-B and DGL-mwp-1A-C, respectively, much larger than the 0.1 Sv meltwater discharge shown in Fig. 4.

The results from the four sensitivity experiments suggest that, with fast discharge and large magnitude, the impact of a given amount of meltwater discharge in the southern hemisphere can be as significant as that in the Northern Hemisphere, and in the extreme case, can shut off the AMOC completely. Therefore, based on climate impact alone, it is also not possible to differentiate the origin of the mwp-1A between the Northern Hemisphere and southern hemispheres. Furthermore, there is also strong disagreement among proxy records during the mwp-1A. The AMOC reconstruction from Bermuda GGC5 [McManus et al., 2004] and other marine records [Clark et al., 1996; Bard et al., 2000; Waelbroeck et al., 1998] suggest AMOC does not slow down and there is not a significant meltwater discharge in the Northern Hemisphere during the mwp-1A, but the Greenland SAT reconstruction and the marine record southern of Iceland [Stanford et al., 2006; Thornalley et al., 2010] show the existence of meltwater discharge and AMOC slowdown during Older Dryas. The disagreement among the proxy data can be due to the resolution of the marine record, with the possibility that the short events like Older Dryas can be simply missed in the low-resolution reconstructions.

With the challenge of the disagreement of proxy data, I adopted in TraCE-21K the estimate from sea level fingerprinting and earth model studies that Antarctic could contribute as much as 15 m to the mwp-1A and the other 5 m came from the Northern Hemisphere [Clark et al., 2002; Bassett et al., 2005]. Two schemes of the meltwater discharge were applied to simulate the mwp-1A (Fig. 20, Table 4 and 5). The first scheme (TraCE-mwp-1A) mimics a 500-year meltwater pulse in both hemispheres, and the rate of meltwater discharge in southern hemisphere

is three times of that in the Northern Hemisphere, such that 5 meter of mwp-1A came from north and 15 meter came from south. The second scheme (DGL-mwp-1A-D) is a simpler version of the first, with constant meltwater discharge in both hemispheres for 500 years and the rate of meltwater discharge in the south is three times of that in the north. In the first scheme with pulse-like meltwater discharge, the reduction of the simulated AMOC and Greenland SAT to the mwp-1A is very similar to, but a bit less than that with mwp-1A solely from the Northern Hemisphere. The simulated AMOC reduces by 14 Sv from the BA overshoot to the level of 4.5 Sv, and the Greenland SAT reduces by 10 ^{o}C, which agrees with the SAT reduction during Older Dryas from GISP2 SAT reconstruction. In the second scheme with constant meltwater discharge, the reduction of the simulated AMOC and Greenland SAT to the mwp-1A is much less than that in the first "pulse-like" scheme. The simulated AMOC reduces by 11 Sv from the BA overshoot to the level of 8 Sv, and the Greenland SAT reduces by 7 ^{o}C, which is 30% less than the ~11 ^{o}C SAT reduction during Older Dryas from GISP2 SAT reconstruction. The larger reduction of the AMOC results from the larger amplitude of meltwater discharge in the pulse-like case. Note that both the pulse-like scheme and the constant meltwater discharge scheme release the same amount of meltwater in the same number of years (500), but the responses of AMOC and Greenland SAT in these two schemes still differ. The dependence of AMOC on the maximum amplitude of meltwater discharge suggests that high-resolution as well as high-precision reconstruction of meltwater discharge is needed to relate AMOC to the meltwater discharge. Since the pulse-like scheme for mwp-1A has a better simulation of the Older Dryas, I adopted this scheme to simulate the climate evolution between mwp-1A and YD.

2.11   TraCE-21K simulation between mwp-1A and YD

The transient climate evolution over Summit Greenland exhibits strong centennial variability between mwp-1A and YD (Fig. 21). The cooling of the Older Dryas is ended at 14 ka by the warming of the Allerød oscillation, which itself is interrupted at ~13.5 ka by the IACP. The end of the IACP marks the beginning of YD. Since the focus of the current phase of TraCE-21K is not on the centennial simulation, which can be investigated later by coupled climate models with much higher resolution, I opted to use simple meltwater scheme to simulate the climate transition from Older Dryas to the beginning of YD. Since the average sea level rise during this period is close to 10 m/kyr, I performed three experiments with 10m/kyr meltwater discharge from Northern Hemisphere in DGL-mwp-1A-YD-A, from southern hemisphere in DGL-mwp-1A-YD-B and from both hemispheres in TraCE-preYD.

The response of the AMOC and Greenland SAT is consistent with earlier investigations, with largest (least) reduction in the case of 10m/kyr meltwater discharge from northern (southern) hemisphere and intermediate reduction with 10m/kyr meltwater from both hemispheres. Compared with the proxy data, the case with meltwater from Northern Hemisphere has a reasonable simulation of Greenland SAT at the onset of YD, but the simulated AMOC is too weak. The case with meltwater from southern hemisphere has a better simulation of AMOC, but the simulated Greenland SAT is a bit too high. On the other hand, 10m/kyr meltwater discharge from southern hemisphere during 13.87~12.9 ka implies that the melting of Antarctic Ice sheets accounts for 10 m of global sea level rise in this period; with the 15-m sea level rise contribution from the southern hemisphere during mwp-1A, the total sea level rise due to Antarctic melting amounts to 25 m during the last deglaciation, which is above the estimated

maximum excess ice-equivalent sea level (24.5 m) for the LGM Antarctic Ice Sheets [Clark and Mix, 2002], and leaves no room for Antarctic Ice Sheet melting during the Holocene. Therefore, I decided to choose the case with meltwater discharge from both hemispheres to continue the simulation of TraCE-21K.

2.12   TraCE-21K simulation of YD

2.12.1 The insufficiency of AMOC reduction in simulating the YD cooling

YD has been regarded as the poster child for abrupt climate change. According to the temperature reconstruction from GISP2 [Cuffey and Clow, 1997], YD started at ~12.9 ka with a ~8 ^{o}C drop of temperature over Summit Greenland in ~200 years. The ending of YD started at ~11.7 ka with a 10 ^{o}C increase of Summit Greenland temperature within 150 years. High resolution analysis of the NGRIP ice core [Steffensen et al., 2008] suggested that the abrupt climate changes into and out of YD were actually triggered by even more abrupt climate shifts that occurred within three years. The magnitude of 10 ^{o}C abrupt warming at the end of YD agrees with independent temperature reconstructions through the ratio of nitrogen and argon isotopes during the last deglaciation [Severinghaus et al., 1998; Grachev and Severinghaus 2005].

The trigger of the AMOC reductions in the YD cold interval is still under debate, with the hypotheses of the meltwater discharge from the proglacial Lake Agassiz through either the St. Lawrence River or Mackenzie river [Carlson et al., 2007; Murton et al., 2010; Broecker et al., 1989]. Regardless of the trigger, more and more evidences have shown that the YD cooling recorded at Summit Greenland is associated with the reduction of AMOC and its associated polarward heat transport [McManus et al., 2004; Stanford et al., 2006; Broecker et al., 1985;

Piotrowski et al., 2004], which causes the cooling of the North Atlantic region [Bard et al., 2000; Waelbroeck et al., 1998], the southward shift of the precipitation from the Intertropical Convergence Zone (ITCZ) [Peterson et al., 2000] as well as the weakening of the east Asian monsoon system [Wang et al., 2001].

The focus of the TraCE-21K during YD is to investigate whether the reduction of AMOC alone can account for the magnitude of the YD cooling recorded over Summit Greenland. In fact, three lines of evidences suggest that this might not be true. The strongest evidence is actually from the GISP2 SAT reconstruction itself, which shows the cooling at the onset of YD (8~10 ^{o}C) is twice as large as that during H1 (4~5 ^{o}C). All other things being equal, this implies that a similar collapse of AMOC at the onset of YD can only account for half of the cooling from the record. Secondly, all three recent AMOC reconstructions [McManus et al., 2004; Stanford et al., 2006; Piotrowski et al., 2004] indicate that AMOC did not collapse during YD, which implies that the reduction of the AMOC during YD is less severe than H1 and cannot even account for half of the YD cooling from the reconstructions. Thirdly, atmospheric CO_2 had risen by 50 ppmv between H1 and YD, and should have induced considerable warming through radiative forcing and associated polar amplification. However, the Summit Greenland temperature reconstruction shows that the minimum SAT over Summit Greenland is essentially the same during the H1 and YD (-50 ^{o}C). If both cold events are solely induced by the reduction of AMOC, this implies that the CO_2 sensitivity over Greenland is close to zero.

One possible solution for the larger cooling during YD is the stronger sensitivity of Greenland SAT to the reduction of AMOC, presumably due to the change of the mean state. I performed four sensitivity experiments with meltwater discharge of the 10, 15, 20 and 30 m/kyr

(Fig. 22 and Table 5). The response of the AMOC to the meltwater forcing is similar to the sensitivity experiments I performed during H1 (Fig. 9). AMOC has been reduced to the near-collapse state in the experiments with meltwater forcing over 15 m/kyr. In the case of 10 m/kyr meltwater forcing, AMOC reduces to ~50% of its LGM level at the onset of YD, which agrees with the reduction of AMOC from the reconstruction [McManus et al., 2004]. The simulated Greenland SAT during YD is -41 ^{o}C in the case of the 10 m/kyr meltwater forcing and ranges between -42 to -44 ^{o}C in the cases with collapsed AMOC. Since the simulated Greenland SAT is -39 ^{o}C before the onset of YD, the simulated cooling is 3-5 ^{o}C with the total collapse of the AMOC, which is in the same range of the cooling in the simulation of the H1. For the case with less AMOC reduction, the simulated cooling is merely 2 ^{o}C. The four sensitivity simulations show that the sensitivity of AMOC and Greenland SAT to the meltwater forcing does not exhibit significant change between H1 and YD. As such, the four sensitivity simulations confirm the aforementioned challenges for the simulation of ~9 ^{o}C cooling at the onset of YD: with a total collapse of AMOC, the cooling of Summit Greenland can reach as much as that from H1, but still only half of what is needed; without a total collapse of AMOC as suggested by AMOC reconstructions, the cooling of Summit Greenland is even less!

2.12.2 The reduction of the AMOC due to the opening of the Bering Strait

Due to the insufficiency of AMOC reduction in simulating the full amplitude of YD cooling, I decided to search for other possibilities. Among all the boundary conditions, the transient GHGs and orbital forcing have low uncertainty and do not trigger abrupt Greenland SAT changes in the completed simulations before YD. The retreat of the Northern Hemisphere Ice Sheet might trigger abrupt Greenland SAT changes. But I did not observe any further cooling

other than that is from the AMOC reductions in the previous four sensitivity experiments, in which the YD topography change had already been applied. Abrupt change of the atmospheric aerosol might be another possibility, but there is no data reconstruction for the atmospheric aerosol change at the onset of YD. So far, the only option left to examine seems to be the change of the land/ocean configuration, i.e. the opening of the marginal sea as well as the ocean straits, among which the opening of the Bering Strait is the best candidate.

Between the LGM and present-day, four marginal sea or ocean straits needs to be changed in low-resolution CCSM3 based on Ice-5G paleotopography reconstructions [Peltier, 2004] (Table 1). Among these four changes, the Bering Strait opening occurred just prior to the onset of YD [England and Furze, 2008]. Two sensitivity experiments were performed with and without Bering Strait opening to simulate YD climate evolution using the modified meltwater reconstructions through St. Lawrence River during YD [Carlson et al., 2007] (Fig. 23). The St. Lawrence River discharge during YD exhibited two large pulses of runoff in the early and late YD, separated by one routine event in the middle of YD. Because the St. Lawrence River discharge is the only freshwater forcing considered in these two experiments, the response of AMOC and Greenland SAT also exhibit two periods of the reductions at the early and late YD, with a brief rebound during the middle of YD. Even though the maximum amplitude of the meltwater discharge during YD is 20 m/kyr in the early YD, the simulated AMOC is not collapsed during YD due to the less sensitivity of AMOC to the meltwater discharge through St. Lawrence River (Fig. 4). However, the simulated SAT reduction is ~5 ^{o}C, the same as that with total collapse of the AMOC.

Consistent with earlier box-model studies [Shaffer and Bendtsen, 1994], the opening of the Bering Strait can induce the weakening of AMOC as shown in the two sensitivity experiments (Fig. 23). With the opening of the Bering Strait at 12 ka in the open Bering Strait case, the AMOC starts to drop below the closed Bering Strait case, with the maximum difference of 2 Sv in the late YD. However, the comparison of the simulated Greenland SAT suggests that even though the AMOC is further reduced in the open Bering Strait case, it still fails to induce further cooling over Summit Greenland, questioning the role of the Bering Strait opening in producing further cooling at the onset of YD.

2.12.3 The lack of AMOC overshoot due to the opening of the Bering Strait

Another robust feature of the Bering Strait opening is its ability of preventing AMOC overshoot from the switch-off of the meltwater forcing. After the switch-off the meltwater discharge at the end of YD, the AMOC abruptly recovers and overshoots its LGM level in the case with the closed Bering Strait. Note that the AMOC overshoot at the end of YD is similar to that during the onset of the BA, confirming the overshoot results from earlier experiments that AMOC overshoot is very robust in CCSM3, regardless of changes of ice sheets, atmospheric CO_2 and orbital forcing. However, AMOC overshoot is eliminated in the case of the open Bering Strait (Fig. 23). With the switch-off the meltwater forcing, AMOC recovers much more slowly than in the closed Bering Strait case. When the AMOC in the closed Bering Strait case reaches the maximum of 18 Sv at 11 ka, the AMOC in the open Bering Strait case is only about 10 Sv (Fig. 23 B).

The elimination of the overshoot in the open Bering Strait case is presumably due to the freshwater transport from the Pacific Ocean into the Nordic Sea, where the convective instability

that is responsible for AMOC overshoot occurs. With the closed Bering Strait, the positive surface density anomaly triggered by the switch-off the meltwater discharge induces Nordic Sea sea level drops as a result of the geostrophic adjustment. The lower sea level induces more inflow of the salty and warmer Atlantic water into Nordic Sea. Because salinity has a stronger effect on water density than does temperature in polar region, the inflow of salty and warmer water further increases the density of surface water and acts as a positive feedback to the original density anomaly. In contrast, with the opening of Bering Strait, the sea level drops from the original density anomaly in the Nordic Sea induces inflow of both the salty Atlantic and fresh Pacific water. The fresh Pacific water acts as a negative feedback to slow down the positive feedback induced by the Atlantic inflow, and eventually prevents the convective instability and overshoots in the Nordic Sea.

In summary, Bering Strait opening can induce further weakening of the AMOC through meltwater transport from the Pacific, but its effect on temperature reduction is still minimal. Because the climate impact of Bering Strait opening still relies on its effect on AMOC, it cannot resolve the challenge that AMOC reduction is insufficient to produce the 8~10 $^{\circ}$C cooling reconstructed from the GISP2 oxygen isotopes [Cuffey and Clow, 1997].

In TraCE-YD, I opened Bering Strait at 12.9 ka (Table 1) and adopted the original meltwater discharge reconstruction from St. Lawrence River with a 14 m/kyr routing event between Mackenzie River and St. Lawrence River occurring between 12.2 and 12.0 ka [Carlson et al., 2007] (Fig. 24). Compared with the previous open Bering Strait case, the major difference in TraCE-YD is the collapse of the AMOC in the middle of YD as the result of the routing through Mackenzie River. The sensitivity of AMOC to the meltwater discharge in the Mackenzie

River is significantly larger than that in St. Lawrence River, which results in further reduction and the collapse of AMOC between 12.2 and 12.0 ka. The simulated Greenland SAT reaches -45 °C within the routing event, which is the coldest Greenland SAT simulation among all the YD sensitivity experiments I have performed so far. I therefore choose TraCE-YD for further simulation of TraCE-21K.

2.13   TraCE-21K simulation of the Holocene

2.13.1 Cold biases in the simulation of the early Holocene

The end of the YD cold period marks the transition of the last deglaciation into the Holocene. One of the challenges in the Holocene simulation is the different rate and timings of the YD/Holocene transition at different locations. In Greenland, the transition occurred between 11.7 and 10.0 ka in ~1,700 years. In Cariaco basin of the Tropical Atlantic, the transition occurred within several hundred years at the end of YD [Peterson et al., 2000]. The sea level records as well as the reconstruction of the North American Ice Sheet retreats indicate that more than 20 m sea level rise occurred after 10 ka and the ice sheet melting ended at 6 ka. In TraCE-Holocene, even though both AMOC and Greenland SAT reconstructions show the Holocene transition completed by 10 ka, I opted to keep significant meltwater discharge in the Northern Hemisphere between 10 and 7 ka as suggested by the record of sea level rise [Peltier, 2004; Clark and Mix, 2002] and geological indicators of ice sheet retreat and meltwater discharge [Clark et al., 2002; Clark et al., 2004; Licciardi et al., 1999; Clark et al., 2001; Carlson et al., 2007; Carlson, 2008; Carlson et al., 2009; Clark et al., 2009; Carlson, 2009; Obbink et al., 2010] (Table 4 and Fig. 25). As a result, the simulated Greenland SAT is significantly cooler than the reconstructions between 10 and 7 ka. It is only after the diminishing of the Northern Hemisphere meltwater that the simulated Greenland SAT reaches the Holocene level. Note that the simulated

Holocene Greenland SAT has an excellent agreement with that from the reconstructions and the modern day observations. Since TraCE-21K started from the LGM and integrated forward with prescribed transient greenhouse and orbital forcing, the successful simulation of the Holocene Summit Greenland temperature suggests that CCSM3 has reasonable regional earth system sensitivities over Greenland to radiative forcing of greenhouse gases, notably the CO_2. On the other hand, the comparison between the simulated YD and present-day Summit Greenland temperature shows the YD cooling in TraCE-21K is 12 ^{o}C, which is consistent with the 10$\pm$4 ^{o}C estimation through the ratio of nitrogen and argon isotopes during the last deglaciation [Grachev and Severinghaus, 2005]. In contrast, the GISP2 estimation of the YD cooling is 18 ^{o}C [Cuffey and Clow, 1997] (Fig. 25), which is much higher than the 10$\pm$4 ^{o}C estimation from the ratio of nitrogen and argon isotopes.

2.13.2 The role of Bering Strait in Holocene AMOC stability

The simulation of AMOC failed to reach the reconstructed Holocene level even after the Northern Hemisphere meltwater switches off at 7 ka. Furthermore, the simulated Holocene AMOC is only 11 Sv, even weaker than that at the LGM. A close comparison between the simulated LGM and Holocene shows that the variability of simulated AMOC during the Holocene is enhanced, ranging between 9 and 13 Sv in the late Holocene and between 12 and 13 Sv in the LGM. In other words, the decrease of simulated minimum AMOC is responsible for the weaker AMOC simulation in TraCE-21K during the late Holocene. Note that the simulated AMOC has been able to reach the Holocene level in the AMOC reconstruction during the BA overshoot, and the failure to reach the reconstructed Holocene level is due to the lack of the overshoot at the end of YD with an open Bering Strait. However, with closed Bering Strait, the

simulated AMOC should reach the reconstructed Holocene level, but the associated increase of polarward heat transport should induce extra warming over Summit Greenland and result in the disagreement of Greenland SAT between the model and reconstructions.

To confirm the vital role of Bering Strait opening in simulating the Holocene level of AMOC, two sensitivity experiments were performed with closed Bering Strait in the Holocene (Fig. 26 and Table 5). Holocene-A is the Holocene extension of DGL-YD-CBS-E, with no meltwater forcing during the Holocene. After the AMOC overshoot at the end of YD in Holocene-A, AMOC starts to recover back and reach around 14.5 Sv in the early Holocene, which is ~2 Sv stronger than the LGM level. There is another 1 Sv increase of AMOC during middle Holocene, presumably due to and sea ice retreat associated with CO_2 rise in middle and late Holocene. The simulated Greenland SAT in Holocene-A reaches the reconstructed Holocene level during the AMOC overshoot at the end of YD and stays in this level until 8 ka. The topography changes with the complete removal of the Laurentide Ice Sheet induces ~3.5 ^{o}C warming over Summit Greenland, with no significant change of the AMOC being found at this time. Greenland SAT remains at this level through the rest of Holocene-A simulation. The comparison of Holocene-A with TraCE-Holocene suggests that CCSM3 might have multi-equilibriums in the Holocene (Fig. 26). I use Holocene-B to investigate the possibility of multi-equilibrium in CCSM3 during the Holocene. Holocene-B is similar to Holocene-A, except that there is extra 5 m/kyr meltwater forcing in Holocene-B in the North Atlantic between 10.9 and 7.0 ka. The results from Holocene-B shows that the imposed meltwater forcing can shift both AMOC and Greenland SAT in Holocene-A to the level found in TraCE-Holocene, and the removal of the meltwater forcing is also capable of shifting both back from TraCE-Holocene to

the level of Holocene-A. Two conclusions can be drawn from Holocene-B. First, based on our experiment, no multi-equilibrium was found in CCSM3 during the Holocene with the closed Bering Strait: after the switch-off the meltwater, AMOC jumps back to the previous state immediately. Secondly, the failure of AMOC overshoot after switch-off of the meltwater in TraCE-Holocene is due to the open Bering Strait. The implication is that the mild Holocene climate of the last 10,000 years that human culture were successfully developed might be due to the stabilizing effect of an opened Bering Strait. And the wild D/O (Dansgaard-Oeschger) events during marine isotope stage 3 (MIS3) are potentially due to the Bering Strait closing as the result of the sea level reductions.

In summary, CCSM3 produces reasonable simulation of the Greenland SAT during the Holocene, and exhibit satisfactory regional climate sensitivity to radiative forcing from greenhouse gas, notably CO_2. No multi-equilibriums are found in CCSM3 Holocene simulations with closed Bering Strait. The Bering Strait opening prior to the Holocene is responsible for the lack of abrupt warming events induced by the AMOC overshoot after meltwater discharge diminishes in the early Holocene.

2.14   Summary

The meltwater fluxes from the retreat of the ice sheets have a profound impact on the AMOC as well as global climate [Rahmstorf, 2002; Clark et al., 2002]. The lack of the coupled ice sheet model brings another challenge to TraCE-21K, as explicit modeling of the routines and magnitudes of the meltwater fluxes is not feasible. The reconstruction of the meltwater flux through the last deglaciation is limited and mostly constrained by the sea level rise. However, sea

level rise only constrains the amount of the meltwater flux and, in most cases, does not constrain the location where the water was originated.

Between the LGM and the onset of BA, the meltwater flux from the retreat of the ice sheets is not well constrained and I adopted simple meltwater flux schemes in this simulation (Figs. 27 and 28). I considered only two regions to impose meltwater fluxes: one in the North Atlantic region between 50~70°N, and the other in the Gulf of Mexico. From 19 to 18.4 ka, the first pulse of meltwater fluxes is imposed at the rate of 3 m/kyr over the North Atlantic. From 18.4 to 17.5 ka, the meltwater flux is linearly increased from 0 to 5m/kyr in the Gulf of Mexico and from 3 to 5 m/kyr in the North Atlantic. From 17.5 to 17.0 ka, the meltwater fluxes remains at 5 m/kyr in the Gulf of Mexico and linearly increased from 5 to 15 m/kyr in the North Atlantic. Starting from 17 ka, the meltwater flux in the Gulf of Mexico is shut off, while the meltwater flux in the North Atlantic remains at 15 m/kyr until 14.67 ka before it is abruptly shut off.

In TraCE-21K, the ending of the Bølling warming is attributed to mwp-1A [Fairbanks, 1989], which is responsible for the Northern Hemisphere cooling during Older Dryas. The sources of mwp-1A are uncertain in terms of its origin of northern or southern hemisphere [Weaver et al., 2003; Peltier, 2005]. I adopted the estimates based on sea level fingerprinting technique [Clark et al., 2002; Bassett et al., 2005] that about 5 m of sea level rise came from Northern Hemisphere and 15 m from Antarctic during mwp-1A. The Northern Hemisphere meltwater is routed with similar fluxes into both Mackenzie River and Gulf of Mexico and the southern hemisphere meltwater goes into both Ross Sea and Weddell Sea with similar flux of discharge. A ramped scheme is used to mimic the pulse of mwp-1A. In Northern Hemisphere, meltwater flux increases from 0 to 20 m/kyr between 14.35 and 14.1 ka and decreases from 20

m/kyr to 1.6 m/kyr between 14.1 and 13.87 ka. In southern hemisphere, meltwater flux increases from 0 to 60 m/kyr between 14.35 and 14.1 ka and decreases from 60 m/kyr to 5 m/kyr between 14.1 and 13.87 ka.

Between mwp-1A and the onset of YD, sea level rises at the rate of 10 m/kyr. Because the climate in Northern Hemisphere is rebounding from the Older Dryas into Allerød warming, I attributed half of the sea level rise into southern hemisphere to minimize the cooling effect of meltwater fluxes on Northern Hemisphere climate during this time. Between 13.87 and 12.9 ka, meltwater fluxes in southern hemisphere keeps at 5m/kyr level, but discharges solely into Ross Sea. In the meantime in Northern Hemisphere, meltwater flux of 5m/kyr is routed into Nordic Sea, St. Lawrence River and Gulf of Mexico.

The meltwater scheme during YD (12.9~11.7 ka) is adopted from Carlson et al. [2007], with maximum meltwater of 20m/kyr occurring between 12.5 and 12.0 ka that induces the Northern Hemisphere cooling during YD. Majority of meltwater during YD is routed into the St. Lawrence River, with a brief routing event occurring between 12.2 and 12.0 that part of meltwater from St. Lawrence River is routed into Mackenzie river. With the opening of the Bering Strait at the onset of YD, the termination of meltwater flux at the end of YD fails to produce the abrupt warming during YD/early Holocene transition [Severinghaus et al., 1998].

In the early Holocene, sea level kept rising at the rate of close to 10m/kyr until 8 ka [Clark and Mix, 2002, Clark et al., 2009]. The meltwater associated with sea level should have slowed down AMOC and the associated ocean heat transport, resulting in the cooling of Northern Hemisphere. However, both AMOC reconstruction [McManus et al., 2004] and

Greenland ice core record [Cuffey and Clow, 1997] suggest the glacial climate was terminated around 10 ka, about 2,000 years before Northern Hemisphere completed its full deglaciation. In order to minimize the effect of meltwater on Northern Hemisphere climate, I attributed that 2.5 m/kyr meltwater flux came from the Antarctica and went into the Ross Sea and Weddell Sea between 11.7 and 5 ka (Fig. 25).

In the Northern Hemisphere, the meltwater during the early Holocene is routed into St. Lawrence River, Arctic and Hudson Bay. Before 8.2-ka event, the Northern Hemisphere meltwater exhibits enhanced discharges of ~10 m/kyr between 11.3 and 10 ka and between 9 and 8 ka. At the onset of 8.2-ka cold event, a strong flood of 5 Sv in 0.5 year occurred at 8.47 ka [Barber et al., 1999]. The last major Northern Hemisphere meltwater discharge during the Holocene has the magnitude of 5 m/kyr and occurs between 7.6 and 6.8 ka at the end of Northern Hemisphere deglaciation (Fig. 25).

Overall, TraCE-21K reproduces many major features of the deglacial climate evolution in Greenland, Antarctic, tropical Pacific, Southern and Deep Ocean, suggesting our model exhibits reasonable climate sensitivity in those regions and is capable of simulating abrupt climate change events.

References

Barber, D. C., et al (1999), Forcing of the cold event of 8,200 years ago by catastrophic drainage of Laurentide lakes, Nature, 400(6742), 344-348.

Bard, E., B. Hamelin, M. Arnold, L. Montaggioni, and G. Cabioch (1996), Deglacial sea-level record from Tahiti corals and the timing of global meltwater discharge, Nature, 382, 241.

Bard, E., F. Rostek, J. L. Turon, and S. Gendreau (2000), Hydrological Impact of Heinrich Events in the Subtropical Northeast Atlantic, Science, 289(5483), 1321-1324.

Bassett, S. E., G. A. Milne, J. X. Mitrovica, and P. U. Clark (2005), Ice Sheet and Solid Earth Influences on Far-Field Sea-Level Histories, Science, 309(5736), 925-928, doi: 10.1126/science.1111575.

Broecker, W. S., J. P. Kennett, B. P. Flower, J. T. Teller, and S. Trumbore (1989), Routing of meltwater from the Laurentide Ice Sheet during the Younger Dryas cold episode, Nature, 341, 318.

Broecker, W. S., D. M. Peteet, and D. Rind (1985), Does the ocean-atmosphere system have more than one stable mode of operation? Nature, 315(6014), 21-26.

Carlson, A. E., P. U. Clark, B. A. Haley, G. P. Klinkhammer, K. Simmons, E. J. Brook, and K. J. Meissner (2007), Geochemical proxies of North American meltwater routing during the Younger Dryas cold event, Proceedings of the National Academy of Sciences, 104(16), 6556.

Carlson, A. E. (2008), Rapid early Holocene deglaciation of the Laurentide Ice Sheet, Nature Geosci., 1, 620-624.

Carlson, A. E. (2009), Geochemical constraints on the Laurentide Ice Sheet contribution to Meltwater Pulse 1A, Quaternary Science Reviews, 28(17-18), 1625-1630, doi: DOI: 10.1016/j.quascwerev.2009.02.011.

Carlson, A. E., P. U. Clark, B. A. Haley, and G. P. Klinkhammer (2009), Routing of western Canadian Plains runoff during the 8.2 ka cold event, Geophys.Res.Lett., 36(14), L14704, doi: 10.1029/2009GL038778.

Clark, P. U., and A. C. Mix (2002), Ice sheets and sea level of the Last Glacial Maximum, Quaternary Science Reviews, 21(1-3), 1-7.

Clark, P. U., R. B. Alley, L. D. Keigwin, J. M. Licciardi, S. J. Johnsen, and H. X. Wang (1996), Origin of the first global meltwater pulse following the last glacial maximum, Paleoceanography, 11, 563.

Clark, P. U., A. S. Dyke, J. D. Shakun, A. E. Carlson, J. Clark, B. Wohlfarth, J. X. Mitrovica, S. W. Hostetler, and A. M. McCabe (2009), The Last Glacial Maximum, Science, 325(5941), 710-714, doi: 10.1126/science.1172873.

Clark, P. U., S. J. Marshall, G. K. C. Clarke, S. W. Hostetler, J. M. Licciardi, and J. T. Teller (2001), Freshwater Forcing of Abrupt Climate Change During the Last Glaciation, Science, 293(5528), 283-287, doi: 10.1126/science.1062517.

Clark, P. U., A. M. McCabe, A. C. Mix, and A. J. Weaver (2004), Rapid Rise of Sea Level 19,000 Years Ago and Its Global Implications, Science, 304(5674), 1141-1144, doi: 10.1126/science.1094449.

Clark, P. U., J. X. Mitrovica, G. A. Milne, and M. E. Tamisiea (2002), Sea-Level Fingerprinting as a Direct Test for the Source of Global Meltwater Pulse IA, Science, 295(5564), 2438-2441, doi: 10.1126/science.1068797.

Clark, P. U., and A. C. Mix (2002), Ice sheets and sea level of the Last Glacial Maximum, Quaternary Science Reviews, 21(1-3), 1-7, doi: DOI: 10.1016/S0277-3791(01)00118-4.

Clark, P. U., N. G. Pisias, T. F. Stocker, and A. J. Weaver (2002), The role of thermohaline circulation in abrupt climate change, Nature, 415(6874), 863-869.

Collins, W. D., et al (2006), The Community Climate System Model Version 3 (CCSM3), J.Climate, 19(11), 2122-2143, doi: 10.1175/JCLI3761.1.

Cuffey, K. M., and G. D. Clow (1997), Temperature, accumulation, and ice sheet elevation in central Greenland through the last deglacial transition, Journal of Geophysical Research, 102(C12), 26383-26396.

Cutler, K. B., R. L. Edwards, F. W. Taylor, H. Cheng, J. Adkins, C. D. Gallup, P. M. Cutler, G. S. Burr, and A. L. Bloom (2003), Rapid sea-level fall and deep-ocean temperature change since the last interglacial period, Earth Planet.Sci.Lett., 206(3-4), 253-271, doi: DOI: 10.1016/S0012-821X(02)01107-X.

England, J. H., and M. F. A. Furze (2008), New evidence from the western Canadian Arctic Archipelago for the resubmergence of Bering Strait, Quatern.Res., 70(1), 60-67, doi: DOI: 10.1016/j.yqres.2008.03.001.

Fairbanks, R. G. (1989), A 17,000-year glacio-eustatic sea level record: influence of glacial melting rates on the Younger Dryas event and deep-ocean circulation, Nature, 342(6250), 637-642.

Goelzer, H., J. Mignot, A. Levermann, and S. Rahmstorf (2006), Tropical versus high latitude meltwater influence on the Atlantic circulation, Clim.Dyn., 27(7), 715-725.

Grachev, A. M., and J. P. Severinghaus (2005), A revised +10±4 °C magnitude of the abrupt change in Greenland temperature at the Younger Dryas termination using published GISP2 gas isotope data and air thermal diffusion constants, Quaternary Science Reviews, 24(5-6), 513-519, doi: DOI: 10.1016/j.quascirev.2004.10.016.

Hanebuth, T., K. Stattegger, and P. M. Grootes (2000), Rapid Flooding of the Sunda Shelf: A Late-Glacial Sea-Level Record, Science, 288(5468), 1033-1035, doi: 10.1126/science.288.5468.1033.

Horton, D. E., C. J. Poulsen, and D. Pollard (2010), Influence of high-latitude vegetation feedbacks on late Palaeozoic glacial cycles, Nature Geosci, 3(8), 572-577.

Joos, F., and R. Spahni (2008), Rates of change in natural and anthropogenic radiative forcing over the past 20,000 years, Proceedings of the National Academy of Sciences, 105(5), 1425-1430, doi: 10.1073/pnas.0707386105.

Jouzel, J., et al (2007), Orbital and Millennial Antarctic Climate Variability over the Past 800,000 Years, Science, , doi: 10.1126/science.1141038.

Licciardi, J. M., J. T. Teller, and P. U. Clark (1999), Freshwater routing by the Laurentide Ice Sheet during the last deglaciation, in Mechanisms of Global Climate Change at Millennial Time Scales edited by P. U. Clark, R. S. Webb and L. D. Keigwin, pp. 177–201, American Geophysical Union, Washington, DC, .

Levis, S., G. Bonan, M. Vertenstein, K. W. Oleson (2004), The Community Land Model's Dynamic Global Vegetation Model (CLM-DGVM): Technical Description and User's Guide. NCAR Technical Notes, TN-459+IA

Liu, Z., et al (2009), Transient Simulation of Last deglaciation with a New Mechanism for Bølling-Allerød Warming, Science, 325(5938), 310-314, doi: 10.1126/science.1171041.

Manabe, B. S., and R. J. Stouffer (1999), Are two modes of thermohaline circulation stable? Tellus A, 51(3), 400-411, doi: 10.1034/j.1600-0870.1999.t01-3-00005.x.

McManus, J. F., R. Francois, J. M. Gherardi, L. D. Keigwin, and S. Brown-Leger (2004), Collapse and rapid resumption of Atlantic meridional circulation linked to deglacial climate changes, Nature, 428(6985), 834-837.

Menot, G., E. Bard, F. Rostek, J. W. H. Weijers, E. C. Hopmans, S. Schouten, and J. S. S. Damste (2006), Early Reactivation of European Rivers During the Last deglaciation, Science, 313(5793), 1623-1625, doi: 10.1126/science.1130511.

Milankovitch, M. (1941), Kanon der Erdbestrahlung und seine AnIndung auf das Eiszeitenproblem, Royal Serbian Academy Special Publication 132, Belgrade, Serbia.

Murton, J. B., M. D. Bateman, S. R. Dallimore, J. T. Teller, and Z. Yang (2010), Identification of Younger Dryas outburst flood path from Lake Agassiz to the Arctic Ocean, Nature, 464(7289), 740-743.

Obbink, E. A., A. E. Carlson, and G. P. Klinkhammer (2010), Eastern North American meltwater discharge during the Bølling-Allerød warm periods, Geology, 38(2), 171-174, doi: 10.1130/G30389.1.

Otto-Bliesner, B., C. D. Hewitt, T. M. Marchitto, E. Brady, A. Abe-Ouchi, M. Crucifix, S. Murakami, and S. L. Weber (2007), Last Glacial Maximum ocean thermohaline circulation: PMIP2 model intercomparisons and data constraints, Geophys.Res.Lett., 34(12), L12706, doi: 10.1029/2007GL029475.

Otto-Bliesner, B., E. C. Brady, G. Clauzet, R. Tomas, S. Levis, and Z. Kothavala (2006), Last Glacial Maximum and Holocene Climate in CCSM3, J.Clim., 19(11), 2526-2544.

Otto-Bliesner, B. L., and E. C. Brady (2010), The sensitivity of the climate response to the magnitude and location of meltwater forcing: last glacial maximum experiments, Quaternary Science Reviews, 29(1-2), 56-73, doi: DOI: 10.1016/j.quascwerev.2009.07.004.

Peltier, W. R. (1994), Ice Age Paleotopography, Science, 265(5169), 195-201, doi: 10.1126/science.265.5169.195.

Peltier, W. R. (2004), Global glacial isostasy and the surface of the ice-age Earth- The ICE-5 G(VM 2) model and GRACE, Annu.Rev.Earth Planet.Sci., 32(1), 111-149.

Peltier, W. R. (2005), On the hemispheric origins of meltwater pulse 1a, Quaternary Science Reviews, 24(14-15), 1655-1671, doi: DOI: 10.1016/j.quascwerev.2004.06.023.

Peltier, W. R., and R. G. Fairbanks (2006), Global glacial ice volume and Last Glacial Maximum duration from an extended Barbados sea level record, Quaternary Science Reviews, 25(23-24), 3322-3337.

Peteet, D. (2000), Sensitivity and rapidity of vegetational response to abrupt climate change, Proceedings of the National Academy of Sciences of the United States of America, 97(4), 1359-1361.

Peterson, L. C., G. H. Haug, K. A. Hughen, and U. Rohl (2000), Rapid Changes in the Hydrologic Cycle of the Tropical Atlantic During the Last Glacial, Science, 290(5498), 1947-1951.

Piotrowski, A. M., S. L. Goldstein, S. R. Hemming, and R. G. Fairbanks (2004), Intensification and variability of ocean thermohaline circulation through the last deglaciation, Earth Planet.Sci.Lett., 225(1-2), 205-220, doi: DOI: 10.1016/j.epsl.2004.06.002.

Praetorius, S. K., J. F. McManus, D. W. Oppo, and W. B. Curry (2008), Episodic reductions in bottom-water currents since the last ice age, Nature Geosci, 1(7), 449-452.

Rahmstorf, S. (1995), Bifurcations of the Atlantic thermohaline circulation in response to changes in the hydrological cycle, Nature, 378(6553), 145-149.

Rahmstorf, S. (2002), Ocean circulation and climate during the past 120,000 years, Nature, 419(6903), 207-214.

Rahmstorf, S., M. Crucifix, A. Ganopolski, H. Goosse, I. Kamenkovich, R. Knutti, G. Lohmann, R. Marsh, L. A. Mysak, and Z. Wang (2005), Thermohaline circulation hysteresis: A model intercomparison, Geophys.Res.Lett., 32, L23605.

Renold, M., C. C. Raible, M. Yoshimori, and T. F. Stocker (2010), Simulated resumption of the North Atlantic meridional overturning circulation – Slow basin-wide advection and abrupt local convection, Quaternary Science Reviews, 29(1-2), 101-112, doi: DOI: 10.1016/j.quascwerev.2009.11.005.

Seidov, D., E. Barron, and B. J. Haupt (2001), Meltwater and the global ocean conveyor: northern versus southern connections, Global Planet.Change, 30(3-4), 257-270, doi: DOI: 10.1016/S0921-8181(00)00087-4.

Seidov, D., R. J. Stouffer, and B. J. Haupt (2005), Is there a simple bi-polar ocean seesaw? Global Planet.Change, 49(1-2), 19-27, doi: DOI: 10.1016/j.gloplacha.2005.05.001.

Severinghaus, J. P., T. Sowers, E. J. Brook, R. B. Alley, and M. L. Bender (1998), Timing of abrupt climate change at the end of the Younger Dryas interval from thermally fractionated gases in polar ice, Nature, 391, 141.

Shaffer, G., and J. Bendtsen (1994), Role of the Bering Strait in controlling North Atlantic ocean circulation and climate, Nature, 367(6461), 354-357.

Stanford, J. D., E. J. Rohling, S. E. Hunter, A. P. Roberts, S. O. Rasmussen, E. Bard, J. McManus, and R. G. Fairbanks (2006), Timing of meltwater pulse 1a and climate responses to meltwater injections, Paleoceanography, 21(4), PA4103.

Steffensen, J. P., et al (2008), High-Resolution Greenland Ice Core Data Show Abrupt Climate Change Happens in Few Years, Science, 321(5889), 680-684, doi: 10.1126/science.1157707.

Stocker, T. F., and O. Marchal (2000), Abrupt climate change in the computer: Is it real? Proceedings of the National Academy of Sciences of the United States of America, 97(4), 1362-1365.

Stommel, H. (1961), Thermohaline convection with two stable regimes of flow, Tellus, 13(2), 224-230.

Stott, L., A. Timmermann, and R. Thunell (2007), Southern Hemisphere and Deep-Sea Warming Led Deglacial Atmospheric CO_2 Rise and Tropical Warming, Science, 318(5849), 435-438.

Stouffer, R. J., D. Seidov, and B. J. Haupt (2007), Climate Response to External Sources of Freshwater: North Atlantic versus the Southern Ocean, J.Clim., 20(3), 436-448.

Stouffer, R. J., J. Yin, J. M. Gregory, K. W. Dixon, M. J. Spelman, W. Hurlin, A. J. Weaver, M. Eby, G. M. Flato, and H. Hasumi (2006), Investigating the Causes of the Response of the Thermohaline Circulation to Past and Future Climate Changes, J.Clim., 19(8), 1365-1387.

Thornalley, D. J. R., I. N. McCave, and H. Elderfield (2010), Freshwater input and abrupt deglacial climate change in the North Atlantic, Paleoceanography, 25, doi: 10.1029/2009PA001772.

Waelbroeck, C., L. Labeyrie, J. C. Duplessy, J. Guiot, M. Labracherie, H. Leclawere, and J. Duprat (1998), Improving past sea surface temperature estimates based on planktonic fossil faunas, Paleoceanography, 13, 272-283.

Wang, Y. J., H. Cheng, R. L. Edwards, Z. S. An, J. Y. Wu, C. -. Shen, and J. A. Dorale (2001), A High-Resolution Absolute-Dated Late Pleistocene Monsoon Record from Hulu Cave, China, Science, 294(5550), 2345-2348, doi: 10.1126/science.1064618.

Weaver, A. J., O. A. Saenko, P. U. Clark, and J. X. Mitrovica (2003), Meltwater Pulse 1A from Antarctica as a Trigger of the Bølling-Allerød Warm Interval, Science, 299(5613), 1709-1713, doi: 10.1126/science.1081002.

Yeager, S. G., C. A. Shields, W. G. Large, and J. J. Hack (2006), The Low-Resolution CCSM3, J.Clim., 19(11), 2545-2566.

Yin, J., and R. J. Stouffer (2007), Comparison of the Stability of the Atlantic Thermohaline Circulation in Two Coupled Atmosphere–Ocean General Circulation Models, J.Clim., 20(17), 4293-4315.

Yokoyama, Y., K. Lambeck, P. De Deckker, P. Johnston, and L. K. Fifield (2000), Timing of the Last Glacial Maximum from observed sea-level minima, Nature, 406(6797), 713-716.

Tables

Table 1: The evolution of the land-sea configuration in TraCE-21K based on Ice5G reconstructions.

TraCE Age (ka)	Bathymetry change
22.0-13.1	Initial LGM state
13.1	Barents Sea opens
12.9	Bering Strait opens
07.6	Hudson Bay opens
06.2	Indonesian Throughflow begins

TraCE case name	Bathymetry change
b30.22_0kaDVT	The LGM
b30.13_1kaDVT	Barents Sea opening
b30.12_9kaDVTn	Bering Strait opening
b30.07_6kaDVT	Hudson Bay opening
b30.06_2kaDVT	Indonesian Throughflow

Table 2: The evolution of the Global Ice Sheet in TraCE-21K based on Ice5G reconstructions.

TraCE-21K Age (ka)	Ice5G Topography (ka)
22.0-18.5	The LGM
18.5-17.5	19.0
17.5-17.0	18.0
17.0-16.0	17.0
16.0-15.0	16.0
15.0-13.87	15.0
13.87-13.1	14.0
13.1-12.5	13.0
12.5-12.0	12.5
12.0-11.7	12.0
11.7-11.3	11.5
11.3-10.8	11.0
10.8-10.2	10.5
10.2-09.7	10.0
09.7-09.2	09.5
09.2-08.7	09.0
08.7-08.0	08.5
08.0-07.6	08.0
07.6-07.2	07.5
07.2-06.7	07.0
06.7-06.2	06.5
06.2-05.7	06.0
05.7-05.0	05.5
05.0-04.0	04.5
04.0-03.2	03.5
03.2-02.4	02.5
02.4-01.4	02.0
01.4-00.4	00.5
00.4-00.0	Present-day

TraCE-21K case name	Ice5G Topography (ka)
b30.22_0kaDVT	The LGM
b30.18_5kaDVTa	19.0
b30.17_5kaDVT	18.0
b30.17_0kaDVTd	17.0
b30.16_0kaDVTd	16.0
b30.15_0kaDVTd	15.0
b30.13_87kaDVT	14.0
b30.13_1kaDVT	13.0
b30.12_5kaDVTn	12.5
b30.12_0kaDVTn	12.0
b30.11_7kaDVTa	11.5
b30.11_3kaDVT	11.0
b30.10_8kaDVT	10.5
b30.10_2kaDVT	10.0
b30.09_7kaDVT	09.5
b30.09_2kaDVT	09.0
b30.08_7kaDVT	08.5
b30.08_0kaDVT	08.0
b30.07_6kaDVT	07.5
b30.07_2kaDVT	07.0
b30.06_7kaDVT	06.5
b30.06_2kaDVT	06.0
b30.05_7kaDVT	05.5
b30.05_0kaDVT	04.5
b30.04_0kaDVT	03.5
b30.03_2kaDVT	02.5
b30.02_4kaDVT	02.0
b30.01_4kaDVTc	00.5
b30.00_4kaDVTd	Present-day

Table 3: Latitude and longitude information for the location of the meltwater forcing

Location	Longitude	Latitude
North Atlantic	$80^oW \sim 20^oE$	$50^oN \sim 70^oN$
Mackenzie river	$210^oE \sim 240^oE$	$65^oN \sim 75^oN$
Nordic Sea	$15^oW \sim 30^oE$	$55^oN \sim 75^oN$
St. Lawrence River	$270^oE \sim 310^oE$	$38^oN \sim 60^oN$
Gulf of Mexico	$255^oE \sim 280^oE$	$15^oN \sim 33^oN$
Ross Sea	$140^oE \sim 220^oE$	$60^oS \sim 80^oS$
Weddell Sea	$70^oW \sim 30^oE$	$60^oS \sim 80^oS$
Half Weddell Sea	$70^oW \sim 15^oE$	$65^oS \sim 80^oS$
Hudson Strait	$280^oE \sim 312^oE$	$55^oN \sim 70^oN$
Arctic	$200^oE \sim 275^oE$	$70^oN \sim 76^oN$
Barents Sea	$25^oE \sim 55^oE$	$65^oN \sim 80^oN$
North Sea	$0^oE \sim 12^oE$	$45^oN \sim 62^oN$

Table 4: Evolution of meltwater flux in TraCE-21K

Exp Name	Age (ka)	NHMW (m/kyr)	NHMW location	SHMW (m/kyr)	SHMW location
TraCE-the LGM	**22-19**	/	/	/	/
TraCE-H1	**19-18.4**	**3**	**North Atlantic**	/	/
	18.4-17.5	**Ramping 3 to 5**	**North Atlantic**	/	/
		Ramping 0 to 5	**Gulf of Mexico**	/	/
	17.5-17.0	**Ramping 5 to 15**	**North Atlantic**	/	/
		5	**Gulf of Mexico**	/	/
TraCE-BA	**17-14.67**	**15**	**North Atlantic**	/	/
	14.67-14.35	/	/	/	/
TraCE-mwp-1A	**14.35-14.10**	**Ramping 0 to 10**	**MacKenzie River**	**Ramping 0 to 30**	**Ross Sea**
		Ramping 0 to 10	**Gulf of Mexico**	**Ramping 0 to 30**	**Weddell Sea**
	14.10-13.85	**Ramping 10 to 0**	**MacKenzie River**	**Ramping 30 to 0**	**Ross Sea**
		Ramping 10 to 0	**Gulf of Mexico**	**Ramping 30 to 0**	**Weddell Sea**
TraCE-preYD	**13.87-12.9**	**1**	**Nordic Sea**	**5**	**Ross Sea**
	13.87-13.4	**4**	**Gulf of Mexico**	/	/
	13.4-12.9	**2.4**	**Gulf of Mexico**	/	/
	13.4-12.9	**1.6**	**St.Lawrence River**	/	/

Exp Name	Age (ka)	NHMW (m/kyr)	NHMW location	SHMW (m/kyr)	SHMW location
TraCE-YD	12.9-12.5	14	St.Lawrence River	/	/
	12.5-12.2	20	St.Lawrence River	/	/
	12.2-12.0	6	St.Lawrence River	/	/
		14	MacKenzie River	/	/
	12.0-11.7	12	St.Lawrence River	/	/
	11.7-11.3	0.15	St.Lawrence River	1.12	Weddell Sea
		0.29	Hudson Strait	1.12	Ross Sea
		0.15	Arctic	/	/
		0.38	North Sea	/	/
		0.13	Barents Sea	/	/
TraCE-Holocene	11.3-10.8	0.55	Arctic	1.12	Weddell Sea
		0.55	St.Lawrence River	1.12	Ross Sea
		1.03	Hudson Strait	/	/
		1.32	Barents Sea	/	/
		3.96	North Sea	/	/
	10.8-10.0	0.55	Arctic	1.12	Weddell Sea
		0.55	St.Lawrence River	1.12	Ross Sea
		1.03	Hudson Strait	/	/
		0.68	Barents Sea	/	/
		2.03	North Sea	/	/

Exp Name	Age (ka)	NHMW (m/kyr)	NHMW location	SHMW (m/kyr)	SHMW location
TraCE-Holocene	10.0-09.8	0.55	Arctic	1.12	Weddell Sea
		0.55	St.Lawrence River	1.12	Ross Sea
		1.03	Hudson Strait	/	/
		0.20	Barents Sea	/	/
		0.60	North Sea	/	/
	09.8-09.0	0.55	Arctic	1.12	Weddell Sea
		0.55	St.Lawrence River	1.12	Ross Sea
		1.03	Hudson Strait	/	/
	09.0-08.0	0.42	Arctic	1.12	Weddell Sea
		0.42	St.Lawrence River	1.12	Ross Sea
		7.47	Hudson Strait	/	/
		438 (5 Sv) at 8.47ka for half a year	Hudson Strait	/	/
	08.0-07.6	0.02	Arctic	1.12	Weddell Sea
		0.02	St.Lawrence River	1.12	Ross Sea
		0.33	Hudson Strait	/	/
	07.6-06.85	0.17	Arctic	1.12	Weddell Sea
		0.17	St.Lawrence River	1.12	Ross Sea
		3.13	Hudson Strait	/	/
	06.85-06.0	0.01	Arctic	1.12	Weddell Sea
		0.01	St.Lawrence River	1.12	Ross Sea
		0.21	Hudson Strait	/	/

Exp Name	Age (ka)	NHMW (m/kyr)	NHMW location	SHMW (m/kyr)	SHMW location
TraCE-Holocene	06.0-05.0	/	/	1.12	Weddell Sea
		/	/	1.12	Ross Sea
	05.0-00.0	/	/	/	/

Table 5: Meltwater flux of the sensitivity experiments

Exp	Exp Name	Age (ka)	NHMW location	NHMW (m/kyr)	SHMW location	SHMW (m/kyr)
01	DGL-19ka	19-18.7	North Atlantic	33	/	/
02	DGL-17ka-A	17-16	North Atlantic	Ramping 20 to 40	/	/
03	DGL-17ka-B	17-16	North Atlantic	Ramping 20 to 12.5	/	/
04	DGL-17ka-C	17-16	North Atlantic	15	/	/
05	DGL-17ka-D	17-16.7	North Atlantic	10	/	/
06	DGL-16ka-A	16-15.9	North Atlantic	Switching 40 to 0	/	/
07	DGL-16ka-B	16-15.7	North Atlantic	Switching 40 to 10	/	/
08	DGL-H1-BA	17-14.2	North Atlantic	Ramping 15 to 0	/	/
		17-14.2	Gulf of Mexico	Ramping 5 to 0	/	/
09	DGL-H1-BA-2	16.7-15.0	North Atlantic	Ramping 21 to 0	/	/
		16.7-15.0	Gulf of Mexico	Ramping 5 to 0	/	/
10	DGL-Overshoot-A	18.7-17.5	North Atlantic	Switching 33 to 0	/	/

Exp	Exp Name	Age (ka)	NHMW location	NHMW (m/kyr)	SHMW location	SHMW (m/kyr)
11	DGL-Overshoot-B	16.7-15.6	North Atlantic	Switching 21 to 0	/	/
			Gulf of Mexico	Switching 5 to 0	/	/
12	DGL-Overshoot-C	14.67-13.0	North Atlantic	Switching 15 to 0	/	/
13	DGL-mwp-1A-A	14.2-13.9	North Atlantic	66	/	/
14	DGL-mwp-1A-B	14.2-14.1	/	/	Ross Sea	200
		14.1-13.8	/	/	/	/
15	DGL-mwp-1A-C	14.2-13.9	/	/	Southern Ocean	66
16	DGL-mwp-1A-D	14.2-13.9	MacKenzie River	5	Ross Sea	15
			Gulf of Mexico	5	Weddell Sea	15
17	DGL-mwp-1A-YD-A	13.87-13.1	Nordic Sea	2	/	/
		13.87-13.4	Gulf of Mexico	8	/	/
		13.4-13.1	Gulf of Mexico	4.8	/	/
		13.4-13.1	St. Lawrence River	3.2	/	/
18	DGL-mwp-1A-YD-B	13.87-13.4	/	/	Ross Sea	5
					Weddell	5
19	DGL-YD-CBS-A (CBS: Closed Bering Strait)	12.9-12.4	St. Lawrence River	10	/	/
20	DGL-YD-CBS-B	12.9-11.9	St. Lawrence River	15	/	/
		11.9-10.7	/	/	/	/

Exp	Exp Name	Age (ka)	NHMW location	NHMW (m/kyr)	SHMW location	SHMW (m/kyr)
21	DGL-YD-CBS-C	12.9-11.5	North Atlantic	20	/	/
		11.5-11.3	/	/	/	/
22	DGL- YD-CBS-D	12.9-12.5	North Atlantic	30	/	/
23	DGL- YD-CBS-E	12.9-12.5	St. Lawrence River	14	/	/
		12.5-12.3	St. Lawrence River	20	/	/
		12.3-11.9	St. Lawrence River	6	/	/
		11.9-11.5	St. Lawrence River	12	/	/
		11.5-10.0	/	/	/	/
24	DGL- YD-OBS OBS: (Open Bering Strait) Bering Strait opens at 12.0ka	12.0-11.9	St. Lawrence River	6	/	/
		11.9-11.5	St. Lawrence River	12	/	/
		11.5-10.8	/	/	/	/

Exp	Exp Name	Age (ka)	NHMW location	NHMW (m/kyr)	SHMW location	SHMW (m/kyr)
25	Holocene-A (Topography changed to Present-day state at 8ka)	12.9-12.5	St. Lawrence River	14	/	/
		12.5-12.3	St. Lawrence River	20	/	/
		12.3-11.9	St. Lawrence River	6	/	/
		11.9-11.5	St. Lawrence River	12	/	/
		11.5-04.5	/	/	/	/
26	Holocene-B (branched from Holocene-A, Topography changed to Present-day state at 8ka)	10.9-07.0	North Atlantic	5	/	/
		07.0-04.5	/	/	/	/

Figures
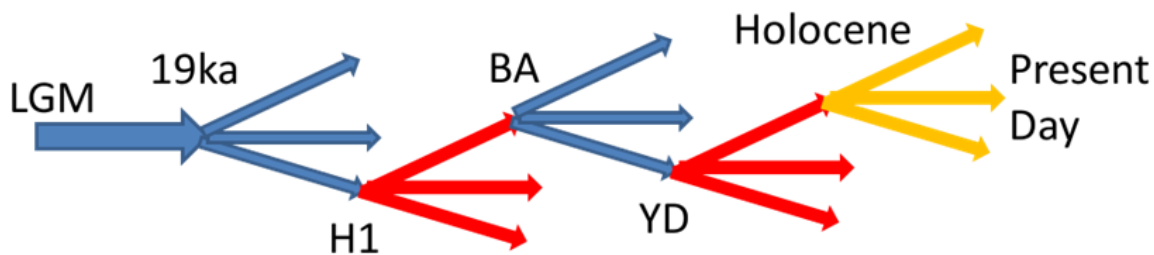
Figure 1: Schematic of the strategy for TraCE-21K. Special attentions are paid to the meltwater forcing during abrupt climate change events, such as 19 ka event for abrupt sea level rise [Clark et al., 2004], Heinrich event 1 (H1), Bølling-Allerød (BA), Meltwater Pulse 1a (mwp-1A), Younger Dryas (YD) and YD-Holocene transition. At each millennial event, several sensitivity experiments were performed with the same initial condition, but different meltwater schemes in terms of the location and the rate of meltwater discharge. After taking into consideration of sea level rise, Atlantic Meridional Overturning Circulation (AMOC) and Greenland surface air temperature (SAT), the sensitivity experiment that best simulates the proxy data were selected to continue the transient simulation.
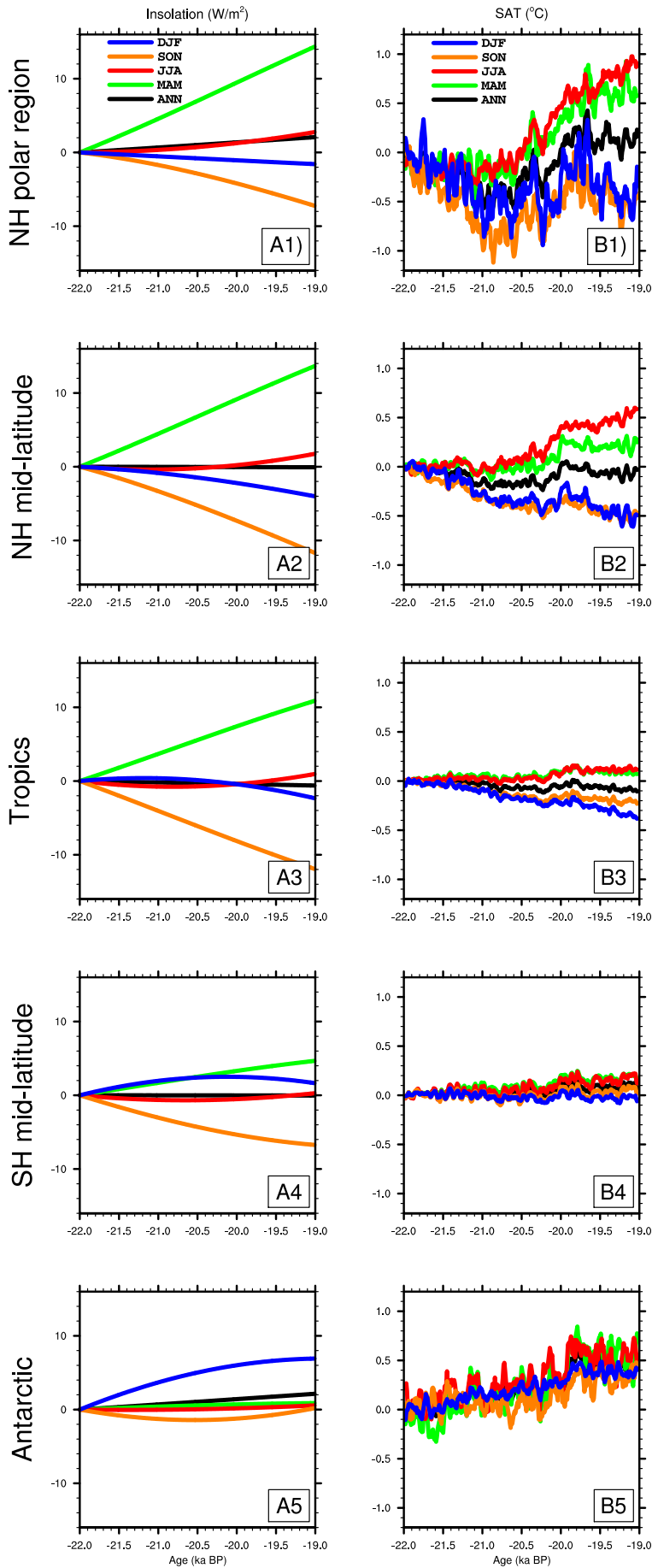
Figure 2: The evolution of the change of the area-averaged surface air temperature (SAT in °C) between 22 and 19 ka in TraCE-21K in seasonal and annual averages. **A1-A5:** Area–averaged insolation (in W m⁻²) in seasonal and annual averages in Northern Hemisphere (NH) polar region (60-90° N) (**A1**), NH midlatitude (30-60° N) (**A2**), Tropics (23.5° N-23.5° S) (**A3**), Southern Hemisphere (SH) midlatitude (30-60° S) (**A4**), and Antarctic (60-90° S) (**A5**). **B1-B5**, Same as **A1-A5**, but for SAT (in °C). SATs are decadal means with 50-year running average. ANN for annual, MAM for March-April-May, JJA for June-July-August, SON for September-October-November and DJF for December-January-February.
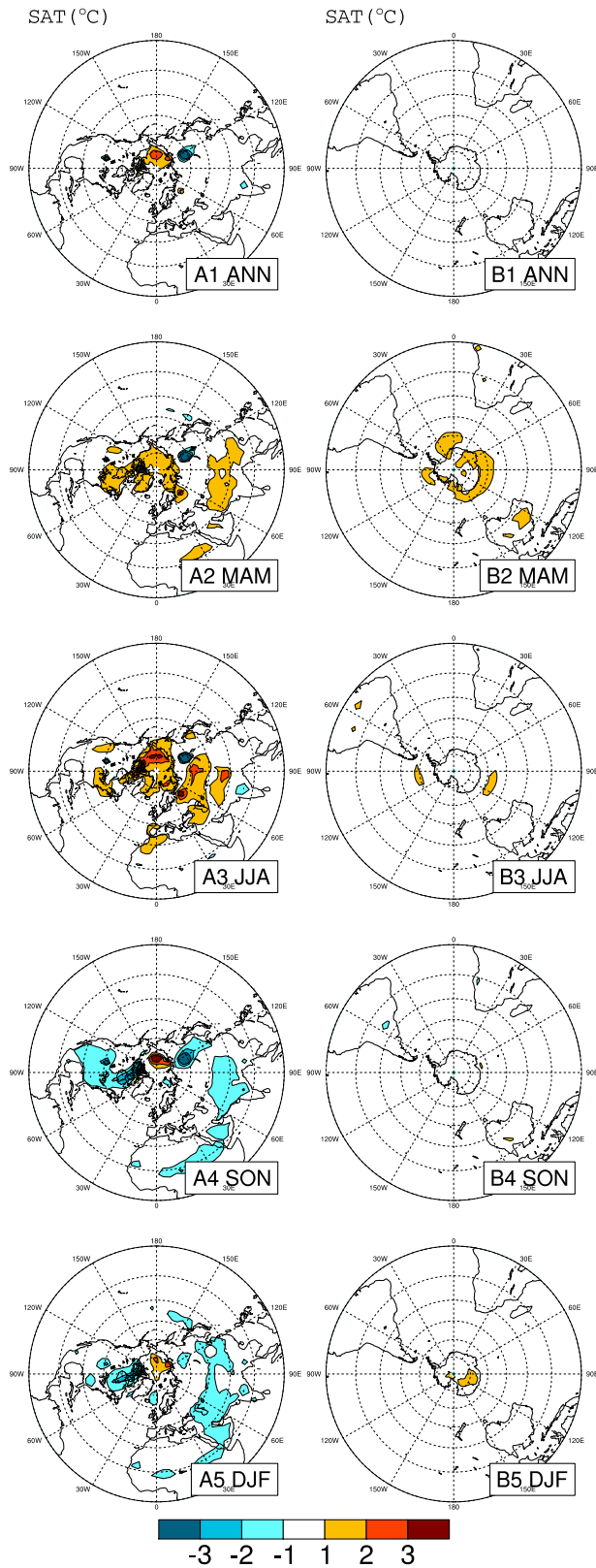
Figure 3: The change of the SAT in (^{o}C) between 22 and 19 ka in TraCE-21K in seasonal and annual averages. **A1-A5:** Northern Hemisphere SAT change in annual mean (**A1**), MAM (**A2**), JJA (**A3**), SON (**A4**), and DJF (**A5**). **B1-B5**, Same as **A1-A5**, but for southern hemisphere. 30-year average SATs are used to derive the differences.
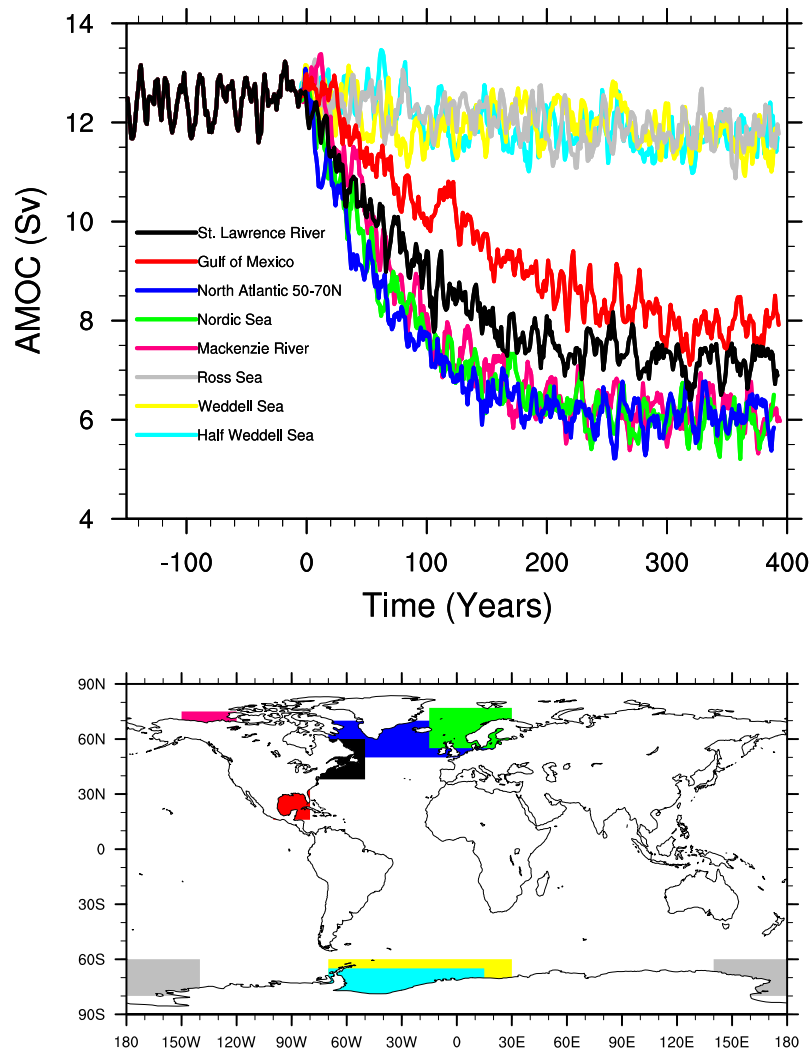
Figure 4: The sensitivity of the AMOC (top) to the locations (bottom) of the 0.1 Sv meltwater forcing. The locations of meltwater forcing includes the Beaufort Sea/Mackenzie River (pink), the Nordic Sea (green), 50 to 70° N of the North Atlantic (blue), the St. Lawrence River/western North Atlantic (black), the Gulf of Mexico (red), Ross Sea (gray), the Weddell Sea (yellow) and half of the Weddell Sea (light blue). The latitude and longitude information for each location is documented in Table 3.
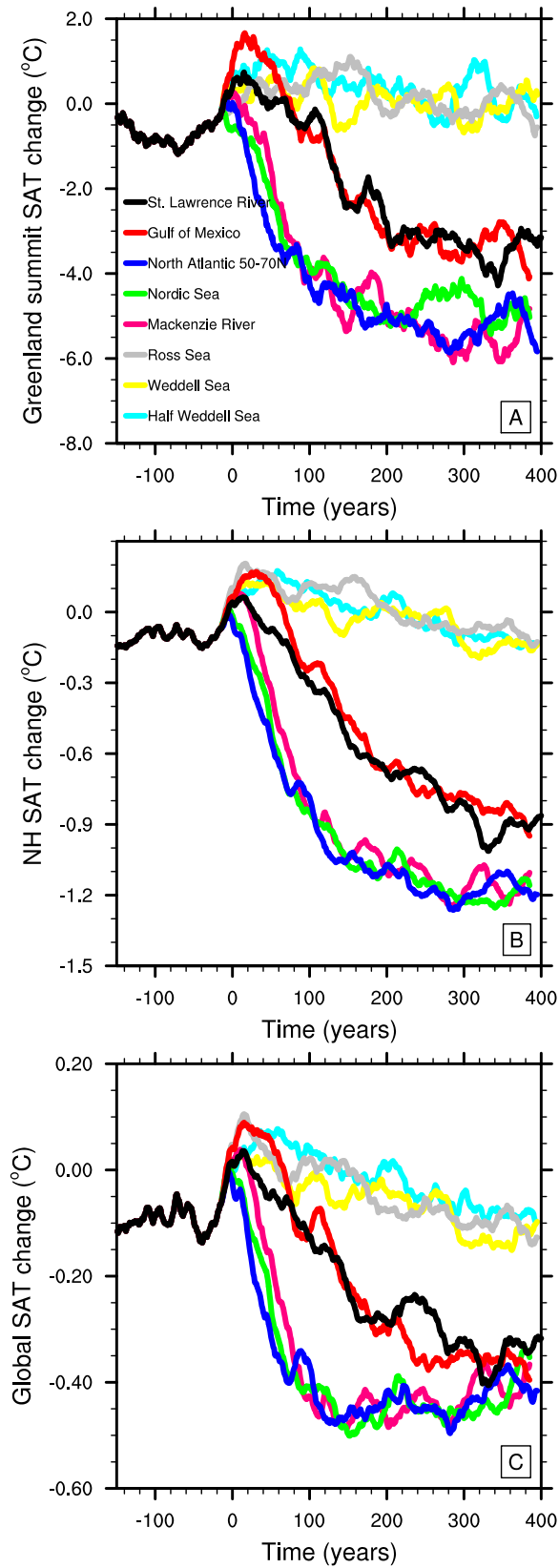
Figure 5: The sensitivity of the (**A**) Greenland Summit, (**B**) Northern Hemisphere and (**C**) global SAT to the locations of the 0.1 Sv meltwater forcing. The location of GISP2 station (38° W and 72° N) is used for the Greenland Summit.
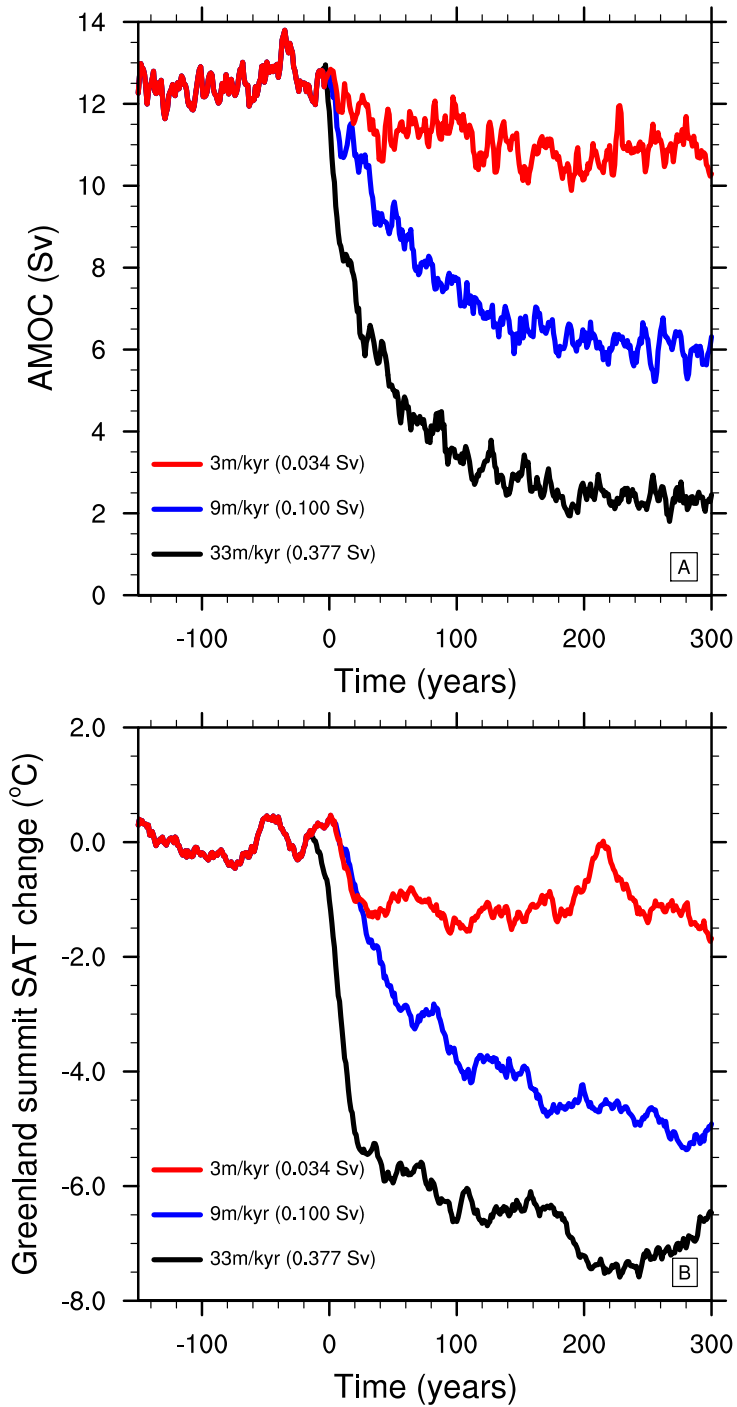
Figure 6: The sensitivity of the Greenland SAT to (**A**) 3 m/kyr, (**B**) 9 m/kyr and (**C**) 33 m/kyr meltwater forcing in 50 to 70° N of the North Atlantic. m/kyr: meters of global sea level rise per thousand years, 1 m/kyr is approximately 0.0114 Sv.
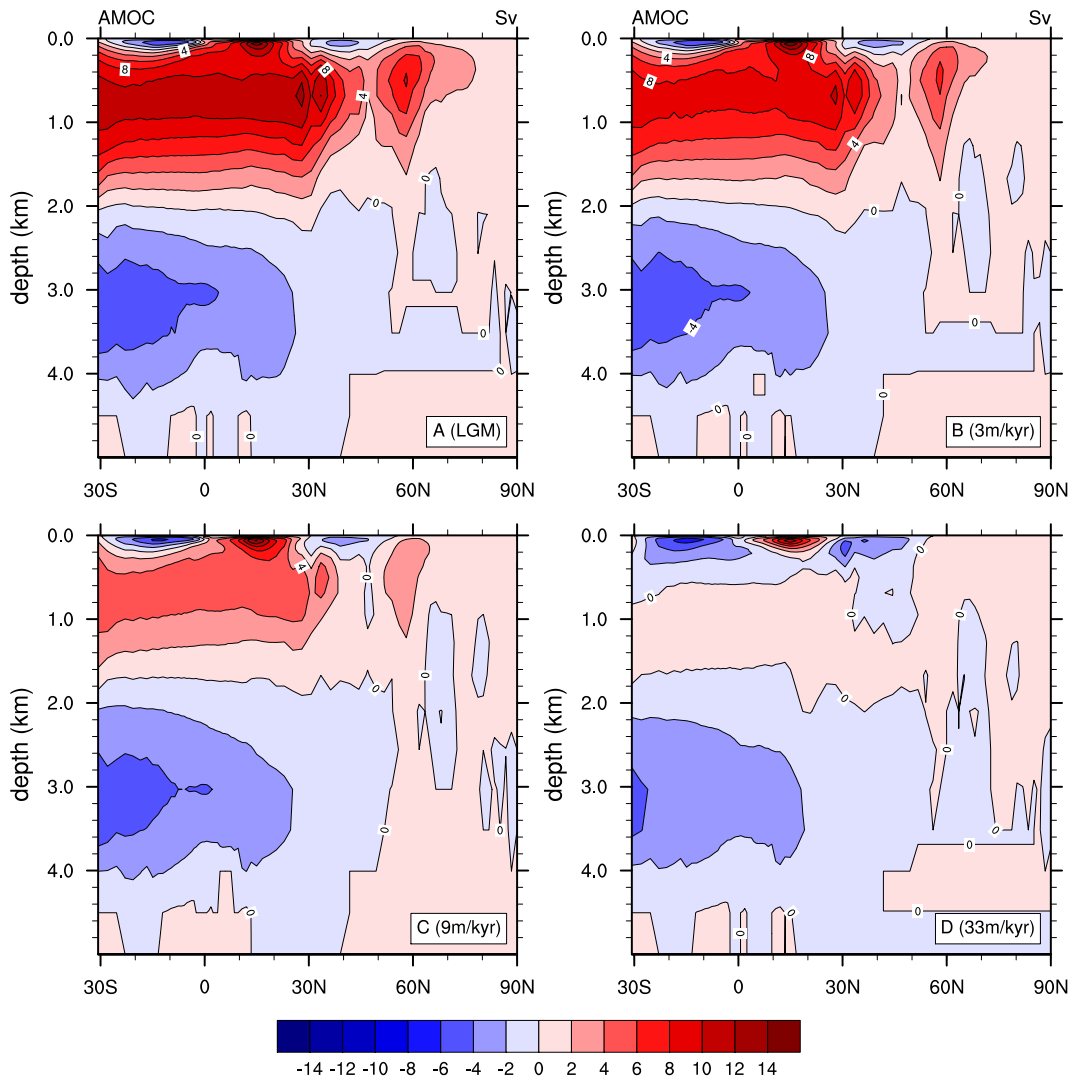
Figure 7: AMOC streamfunction (in sverdrup) at (**A**) the LGM and its response to (**B**) 3 m/kyr, (**C**) 9 m/kyr and (**D**) 33 m/kyr meltwater forcing in 50 to 70°N of the North Atlantic.
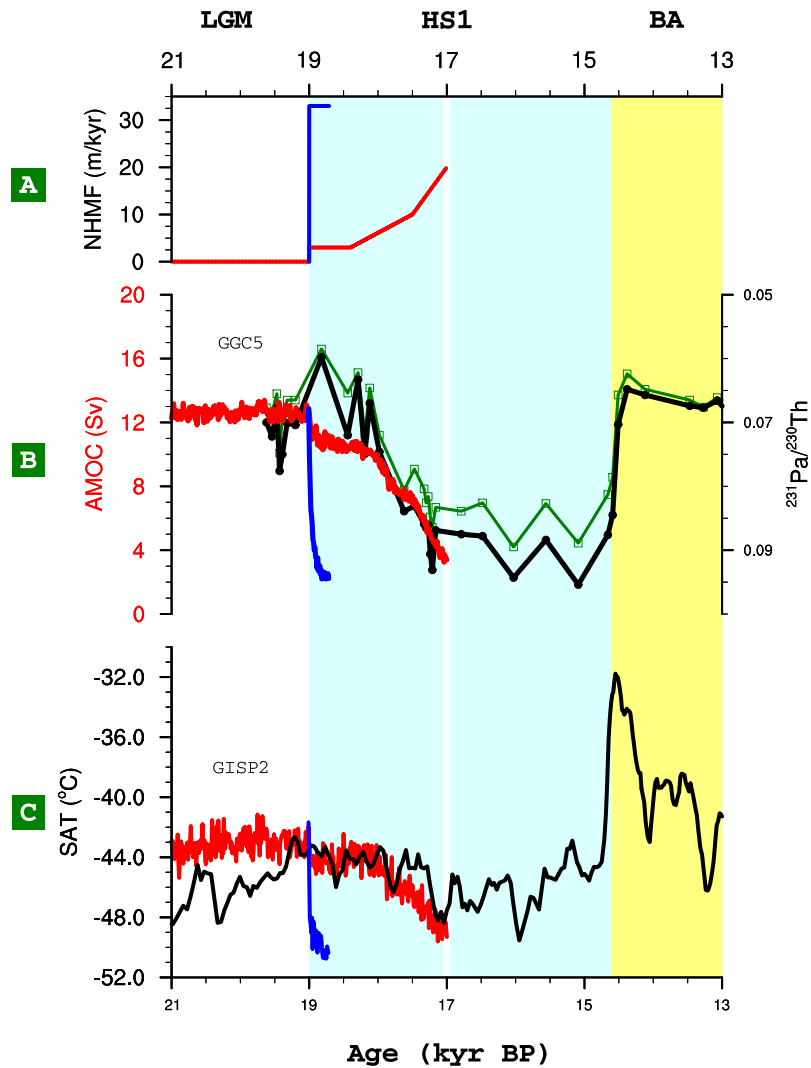
Figure 8: TraCE-21K between 21 and 17 ka. (**A**) NHMW in TraCE-21K (red) and sensitivity experiment DGL-19ka (blue). (**B**) AMOC in TraCE-21K (red) and DGL-19ka (blue), superimposed by AMOC reconstructions (black and green) [McManus et al., 2004]. (**C**) Greenland SAT in TraCE-21K (red) and DGL-19ka (blue), superimposed by Greenland SAT reconstruction based on Greenland Ice Sheet Project 2 (GISP2) δ^{18}O with borehole temperature calibration (black) [Cuffey and Clow, 1997]. Refer to Table 5 for details of DGL-19ka (Exp. 1).
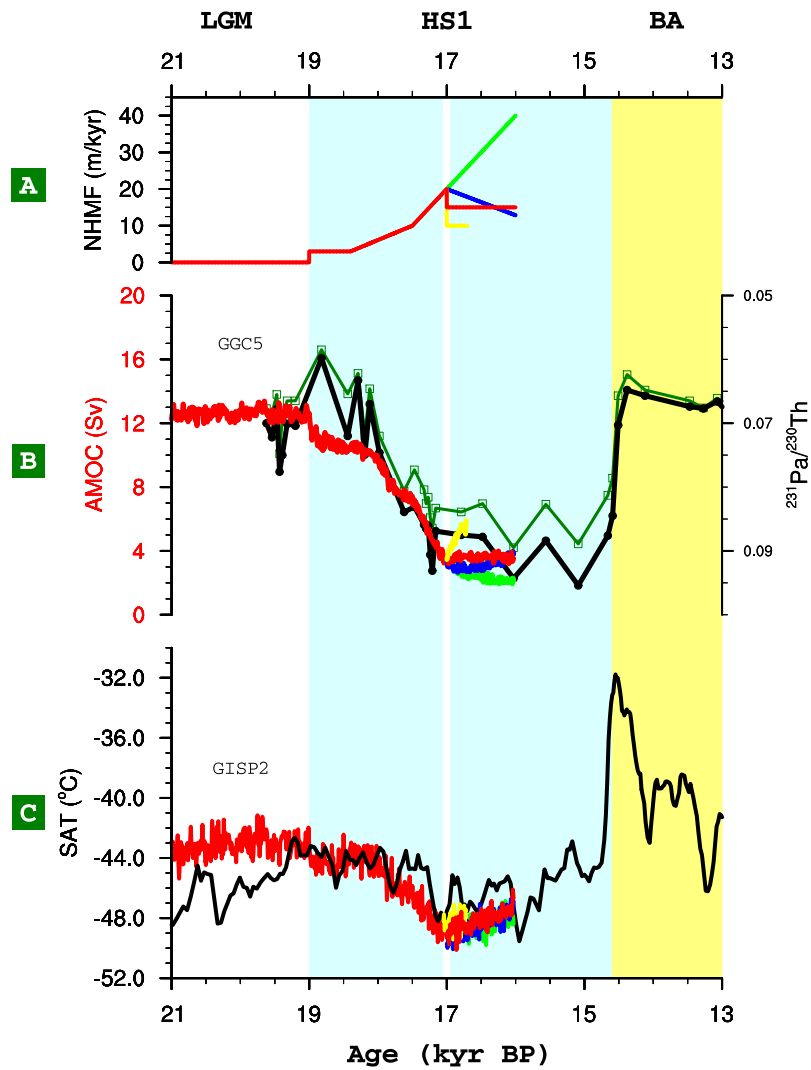
Figure 9: Sensitivity of AMOC (**B**) and Greenland SAT (**C**) to NHMW (**A**) during H1 (~17 ka). Refer to Table 5 for details of the four sensitivity experiments: DGL-17ka-A (green, Exp. 2), DGL-17ka-B (blue, Exp. 3), DGL-17ka-C (red, Exp. 4) and DGL-17ka-D (yellow, Exp. 5).
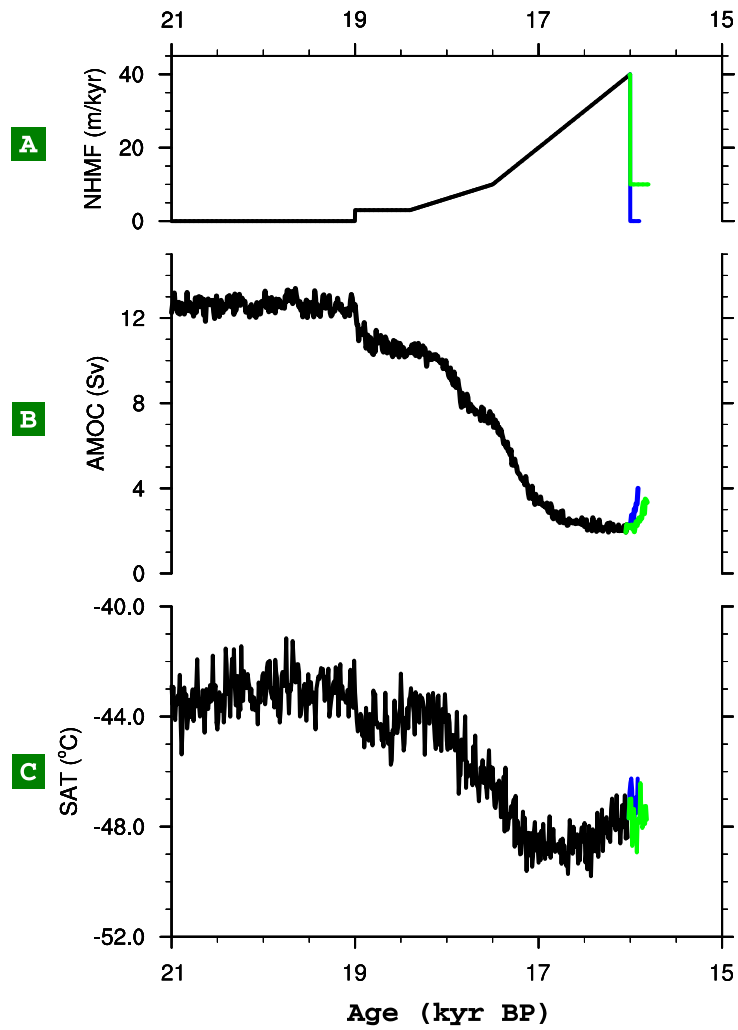
Figure 10: Response of AMOC (**B**) and Greenland SAT (**C**) to switch-off of NMWF (**A**). Refer to Table 5 for details of the two sensitivity experiments: DGL-16ka-A (blue, Exp. 6), DGL-16ka-B (green, Exp. 7).
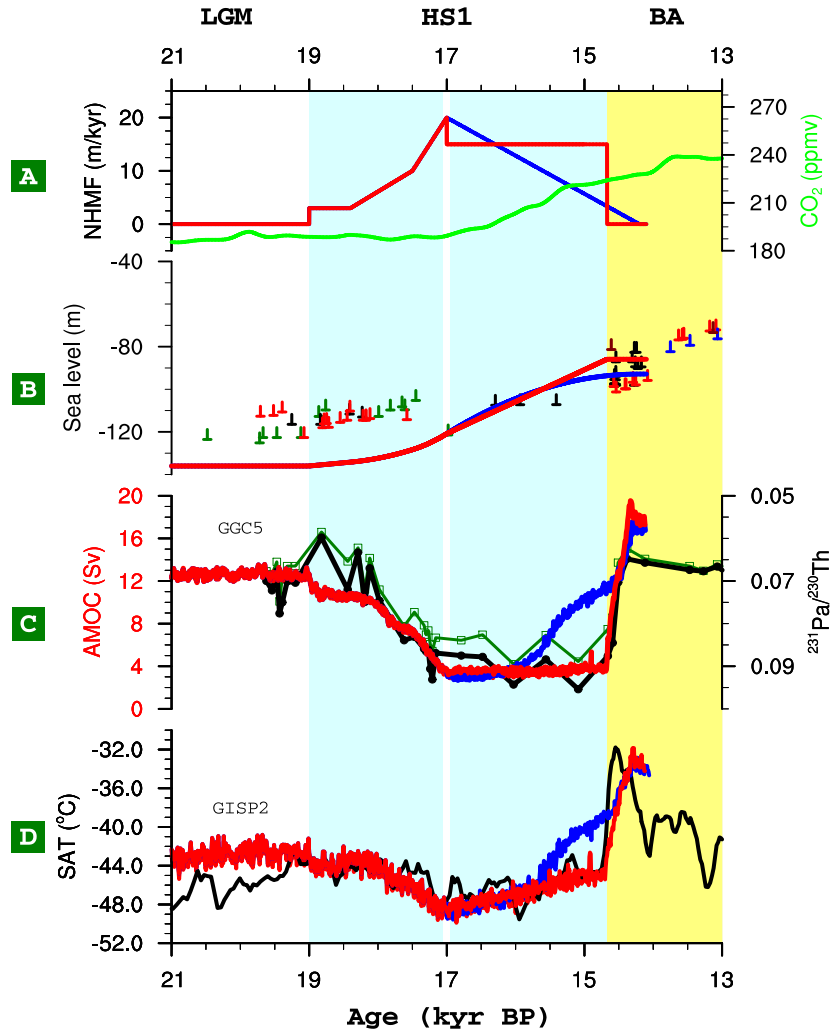
Figure 11: TraCE-21K between 21 and 14.35 ka. (**A**) Atmospheric CO_2 concentration [Joos and Spahni, 2008] (green) and NHMW in segment TraCE-BA of TraCE-21K (red) and sensitivity experiment DGL-H1-BA (blue). Segment TraCE-BA of TraCE-21K and DGL-H1-BA is referred to as DGL-A and DGL-B in Liu et al. [2009], respectively. (**B**) Eustatic sea level rise in segment TraCE-BA of TraCE-21K (red) and DGL-H1-BA (blue), superimposed by relative sea level reconstructions (half-pluses). Sea level data are from Bonaparte Gulf (green) [Yokoyama et al., 2000], Sunda Shelf (black) [Hanebuth et al., 2000], Barbados (red) [Peltier and Fairbanks, 2006], Tahiti (blue) [Bard et al., 1996] and New Guinea (dark red) [Cutler et al., 2003]. The half-pluses represent the 5 m depth uncertainty of the relative sea level records. (**C**) AMOC in scheme TraCE-BA of TraCE-21K (red) and DGL-H1-BA (blue), superimposed by AMOC reconstructions (black and green) [McManus et al., 2004]. (**D**) Greenland SAT in TraCE-21K (red) and DGL-H1-BA (blue), superimposed by Greenland SAT reconstruction based on Greenland Ice Sheet Project 2 (GISP2) $\delta^{18}O$ with borehole temperature calibration (black) [Cuffey and Clow, 1997]. Refer to Table 4 for details of TraCE-BA and Table 5 for DGL-H1-BA (Exp. 8).
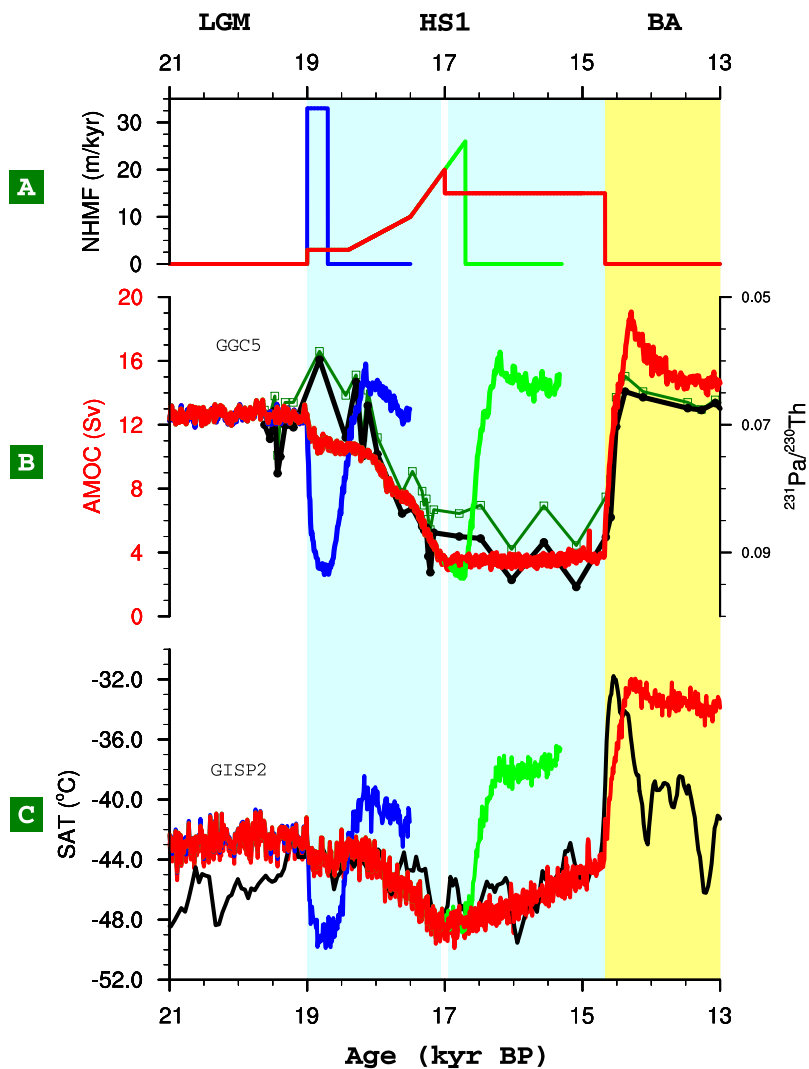
Figure 12: The overshoot of AMOC (**B**) and Greenland SAT (**C**) to the switch-off of NMWF (**A**) in TraCE-21K (red) and three sensitivity experiments. The reconstructions of AMOC (black and darkgreen) [McManus et al., 2004] and Greenland SAT (black) [Cuffey and Clow, 1997] are plotted for comparison. Refer to Table 5 for details of the sensitivity experiments DGL-Overshoot-A (blue, Exp. 10), DGL-Overshoot-B (green, Exp. 11) and DGL-Overshoot-C (red, Exp. 12).
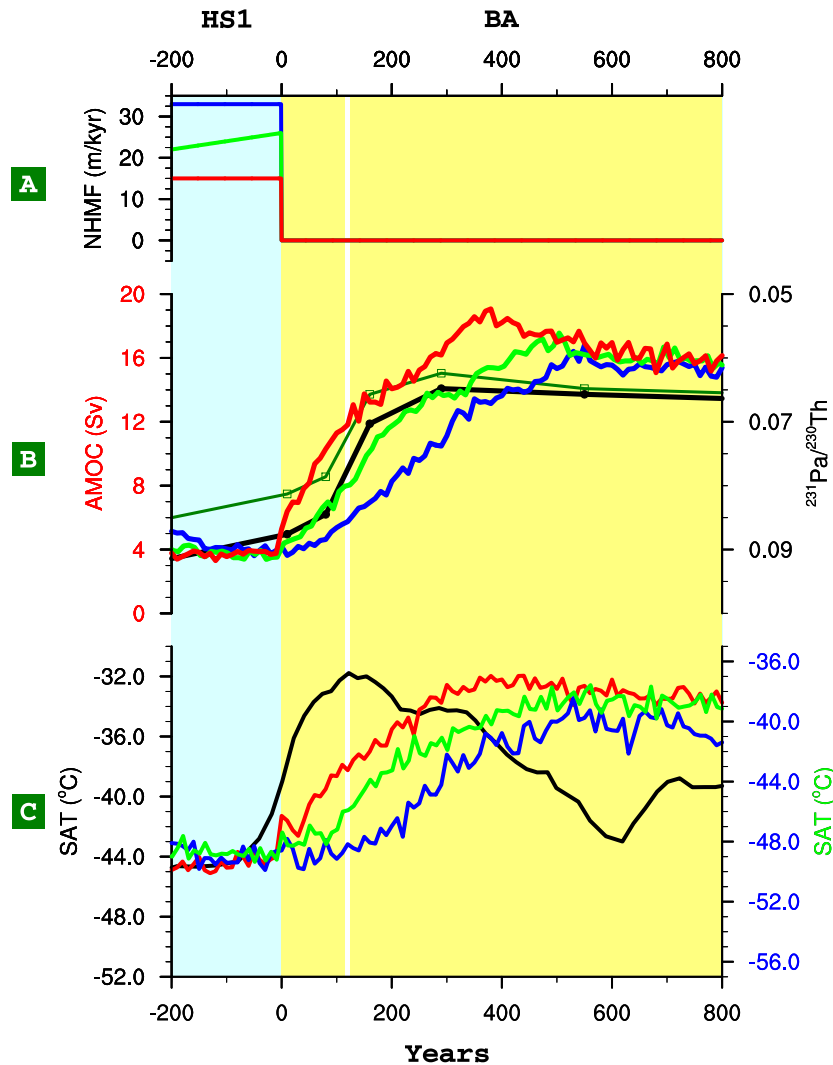
Figure 13: The response of AMOC (**B**) and Greenland SAT (**C**) to the switch-off of the meltwater forcing (**A**) in TraCE-21K and three sensitivity experiments. The white line delineates the time when the AMOC in TraCE-21K recovers to the LGM level of 12.5 Sv. Refer to Table 5 for details of the sensitivity experiments DGL-Overshoot-A (blue, Exp. 10) and DGL-Overshoot-B (green, Exp. 11) and DGL-Overshoot-C (red, Exp. 12). X-axis represents the time after the switch-off of the NHMW, which allows different experiments to be compared even though the NHMW are switched-off at different times during the transient simulations. Note the different y-axes in (**C**) for the three sensitivity experiments: DGL-Overshoot-A (right y-axis), DGL-Overshoot-B (right y-axis) and DGL-Overshoot-C (left y-axis).
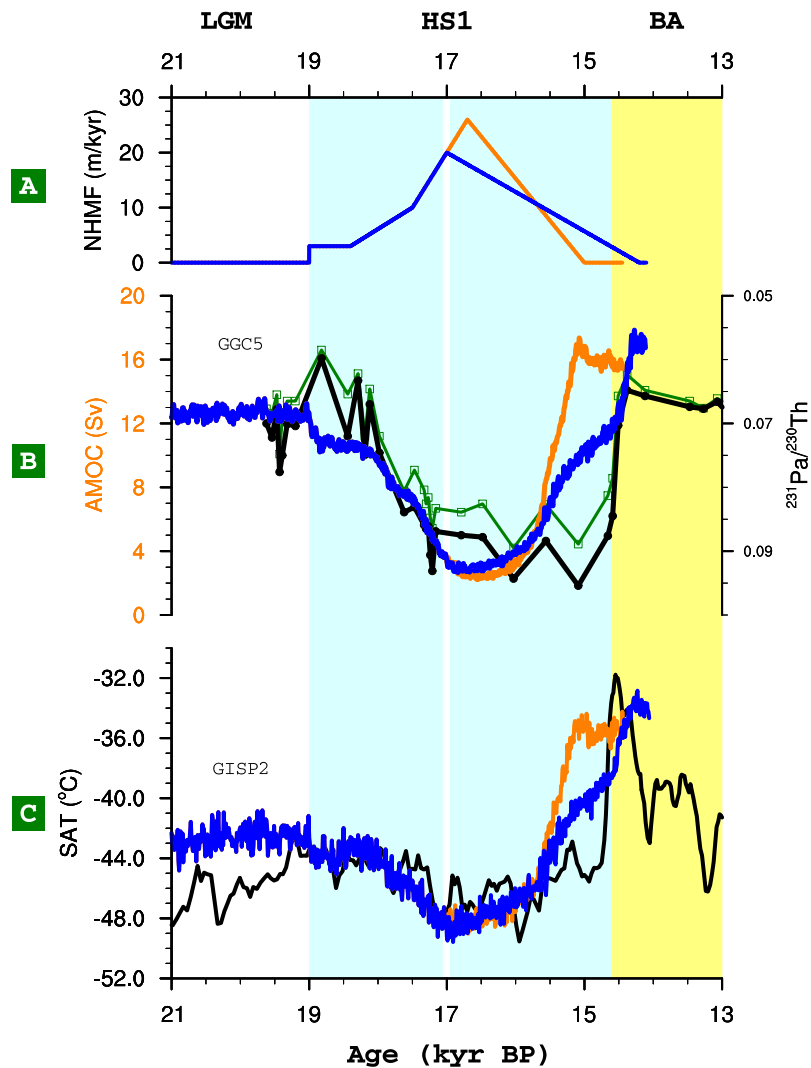
Figure 14: The overshoot of AMOC (**B**) and Greenland SAT (**C**) to the linear reduction of NMWF (**A**) in two sensitivity experiments. The reconstructions of AMOC (black and darkgreen) [McManus et al., 2004] and Greenland SAT (black) [Cuffey and Clow, 1997] are plotted for comparison. Refer to Table 5 for details of the sensitivity experiments DGL-H1-BA (blue, Exp. 8) and DGL-H1-BA-2 (orange, Exp. 9).
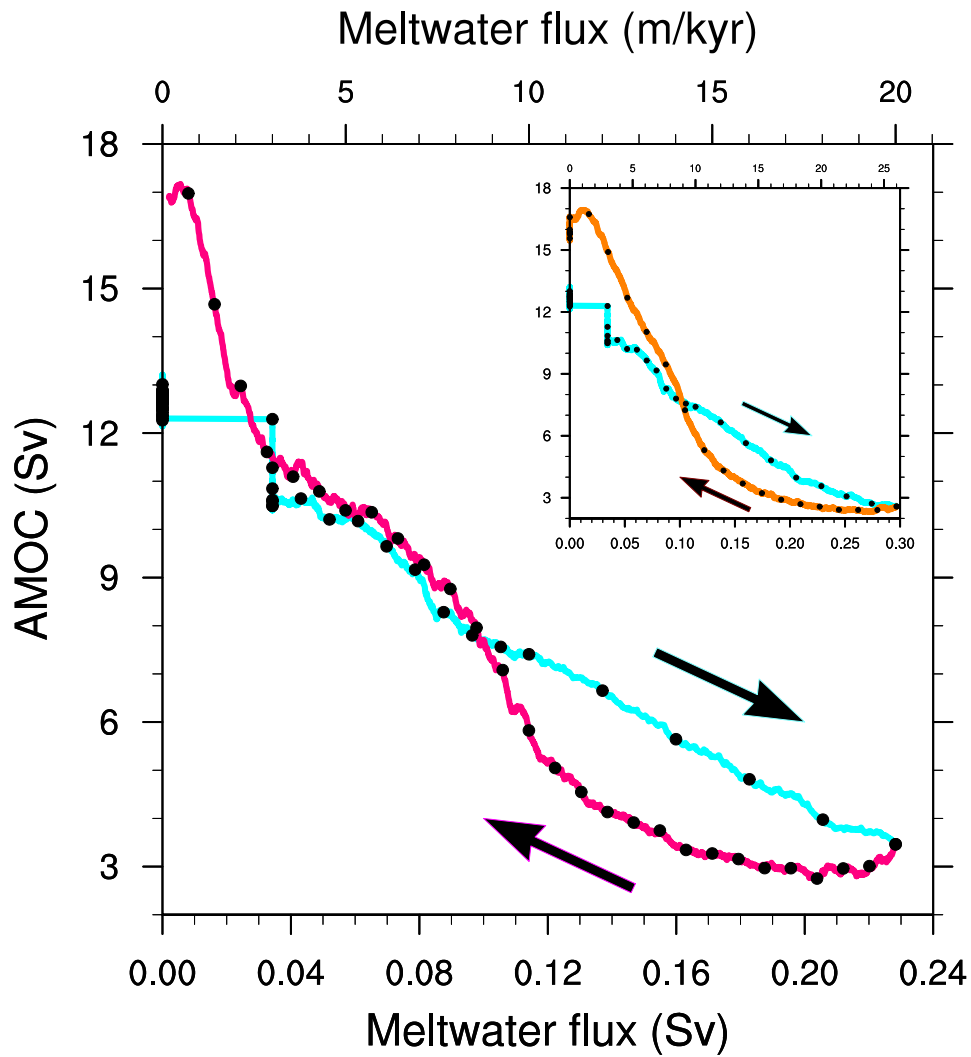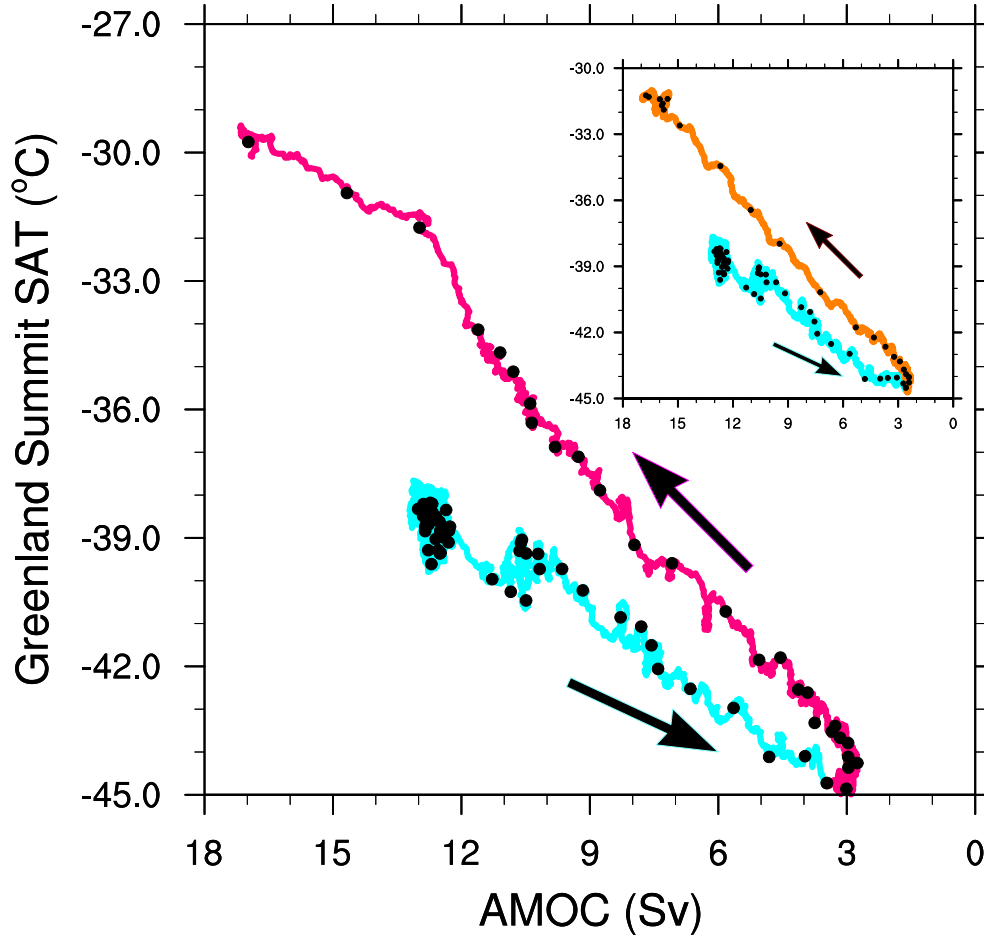
Figure 15: Hysteresis curve between AMOC and NHMW flux found in sensitivity experiment DGL-H1-BA. Each dot represents 100-year running mean. Blue line is for the early part with the increase of the NHMW and purple line for the latter part with the reduction of the NHMW. The inset shows the hysteresis curve for experiment DGL-H1-BA-2. Refer to Table 5 for details of the sensitivity experiments DGL-H1-BA (blue, Exp. 8) and DGL-H1-BA-2 (orange, Exp. 9).
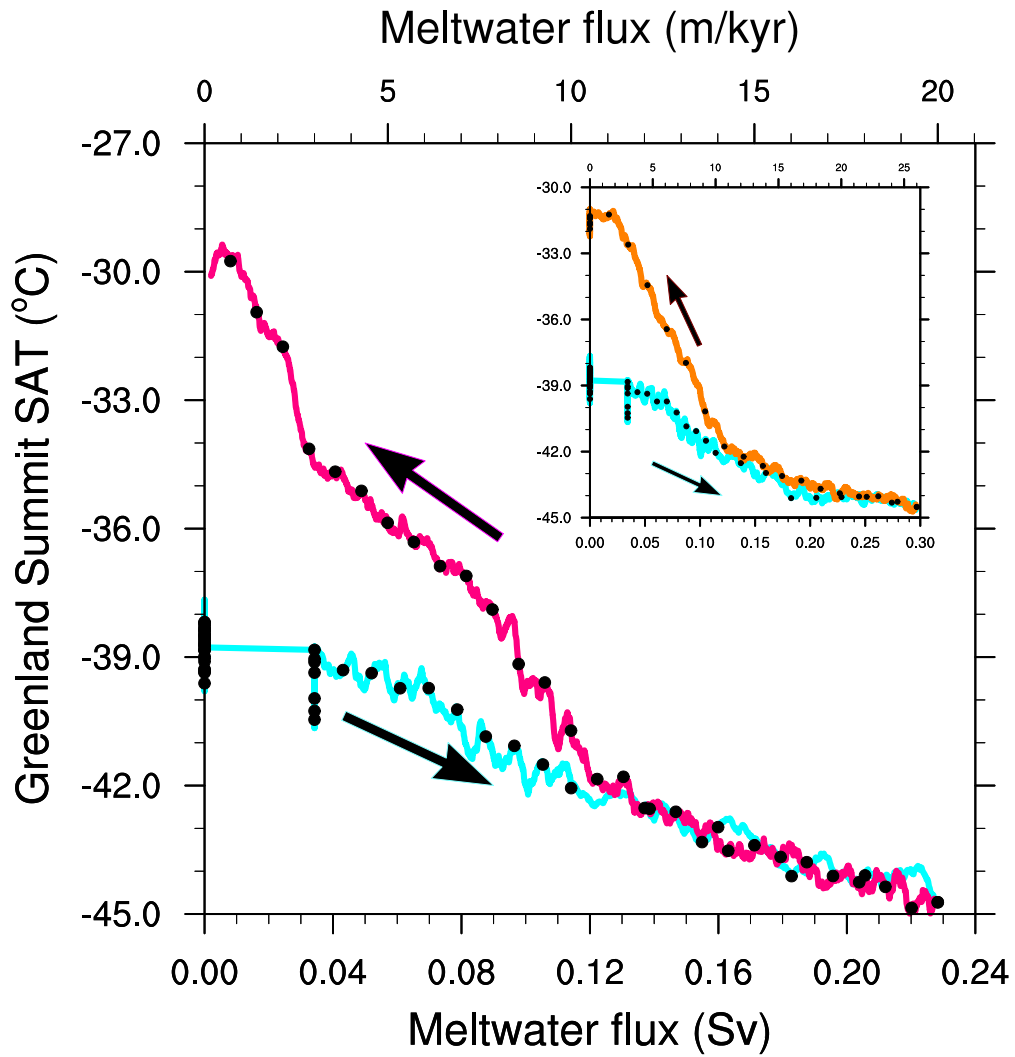
Figure 16: Same as Fig. 15, but for the hysteresis curves between Greenland SAT and NHMW.
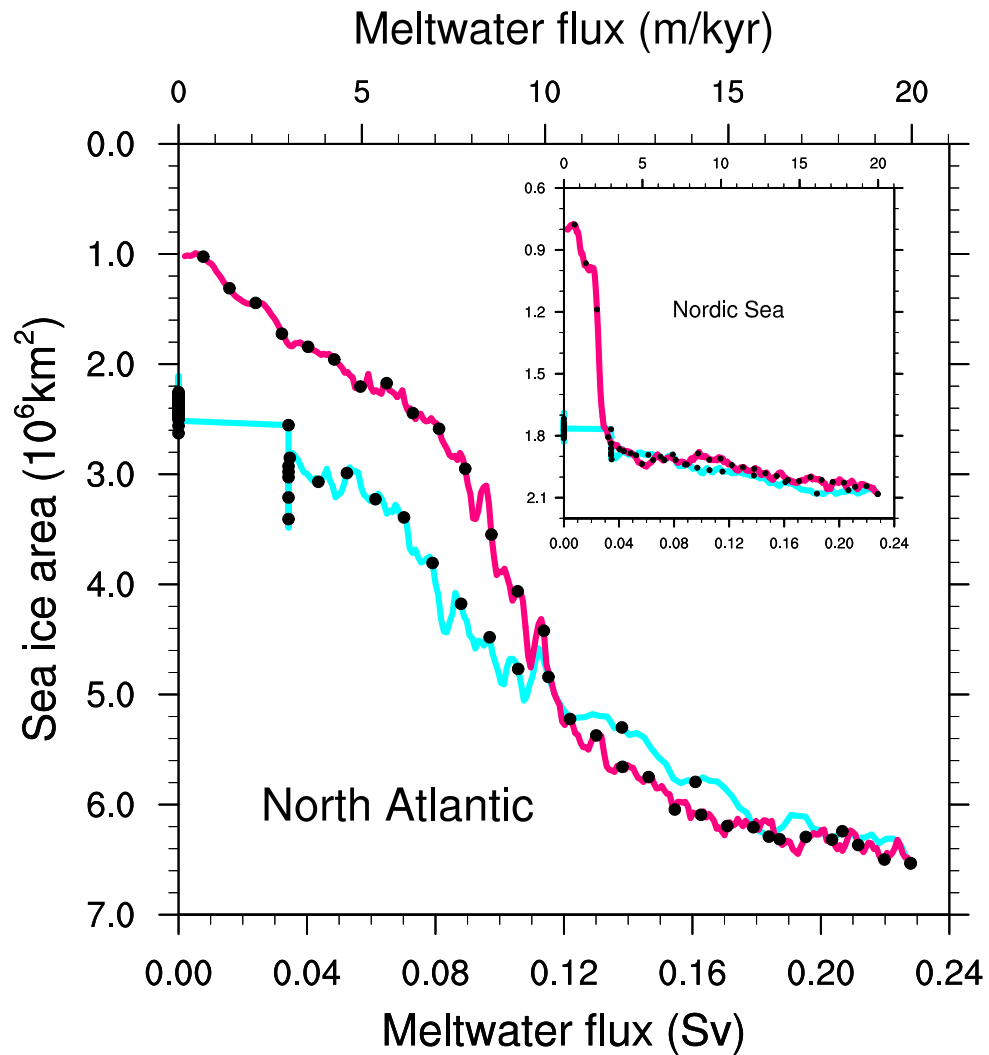
Figure 17: Hysteresis curve between North Atlantic sea ice area and NHMW flux in experiment DGL-H1-BA. Each dot represents 100-year running mean. Blue line is for the early part with the increase of the NHMW and purple line for the latter part with the reduction of the NHMW. The inset shows the hysteresis curve between Nordic Sea sea ice area and NHMW flux in experiment DGL-H1-BA. Refer to Table 5 for details of the sensitivity experiments DGL-H1-BA (blue, Exp. 8) and DGL-H1-BA-2 (orange, Exp. 9).

Figure 18: Linear relationship between Greenland SAT and AMOC in experiment DGL-H1-BA and DGL-H1-BA-2 (inset). Each dot represents 100-year running mean. Blue line is for the early part with the increase of the NHMW and purple (orange in inset) line for the latter part with the reduction of the NHMW. The larger SAT associated with AMOC in the latter part is mostly due to the deglacial CO_2 rise since 17 ka. Refer to Table 5 for details of the sensitivity experiments DGL-H1-BA (blue, Exp. 8) and DGL-H1-BA-2 (orange, Exp. 9).
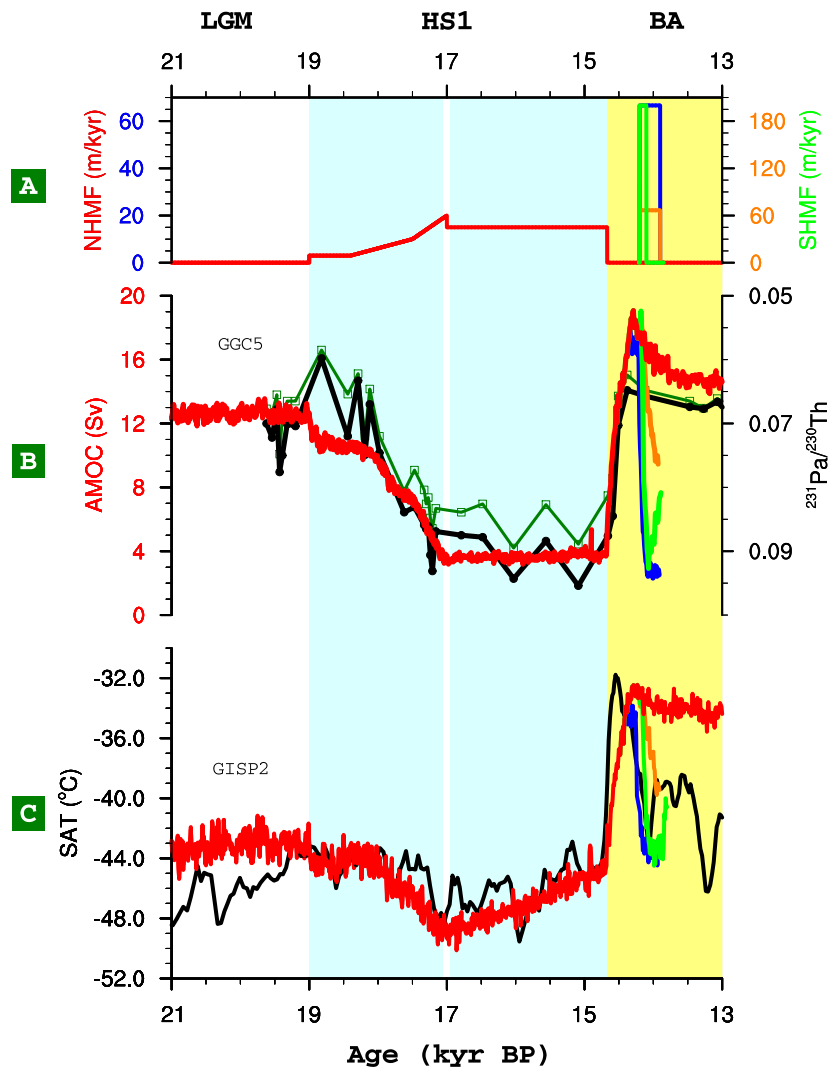
Figure 19: Sensitivity of AMOC (**B**) and Greenland SAT (**C**) to NHMW or SHMW (**A**) during mwp-1A. Refer to Table 5 for details of the four sensitivity experiments: DGL-Overshoot-C (red, Exp. 12), DGL-mwp-1A-A (blue, Exp. 13), DGL-mwp-1A-B (green, Exp. 14) and DGL-mwp-1A-C (orange, Exp. 15).
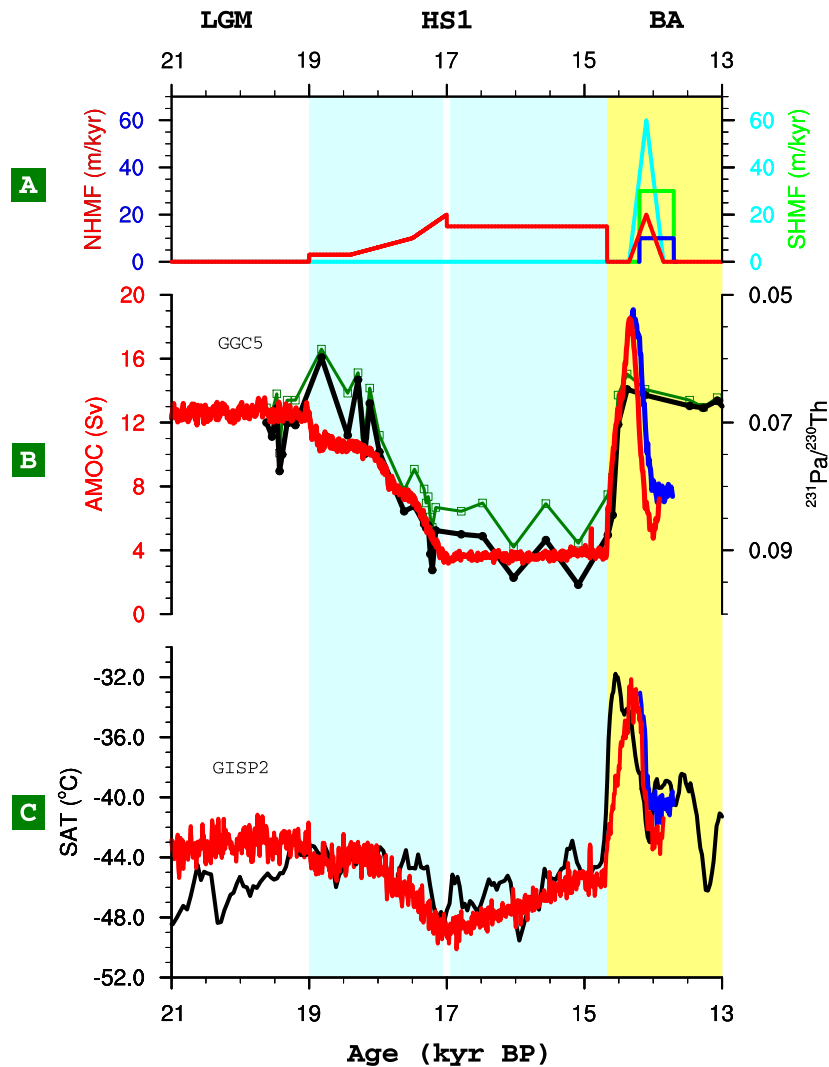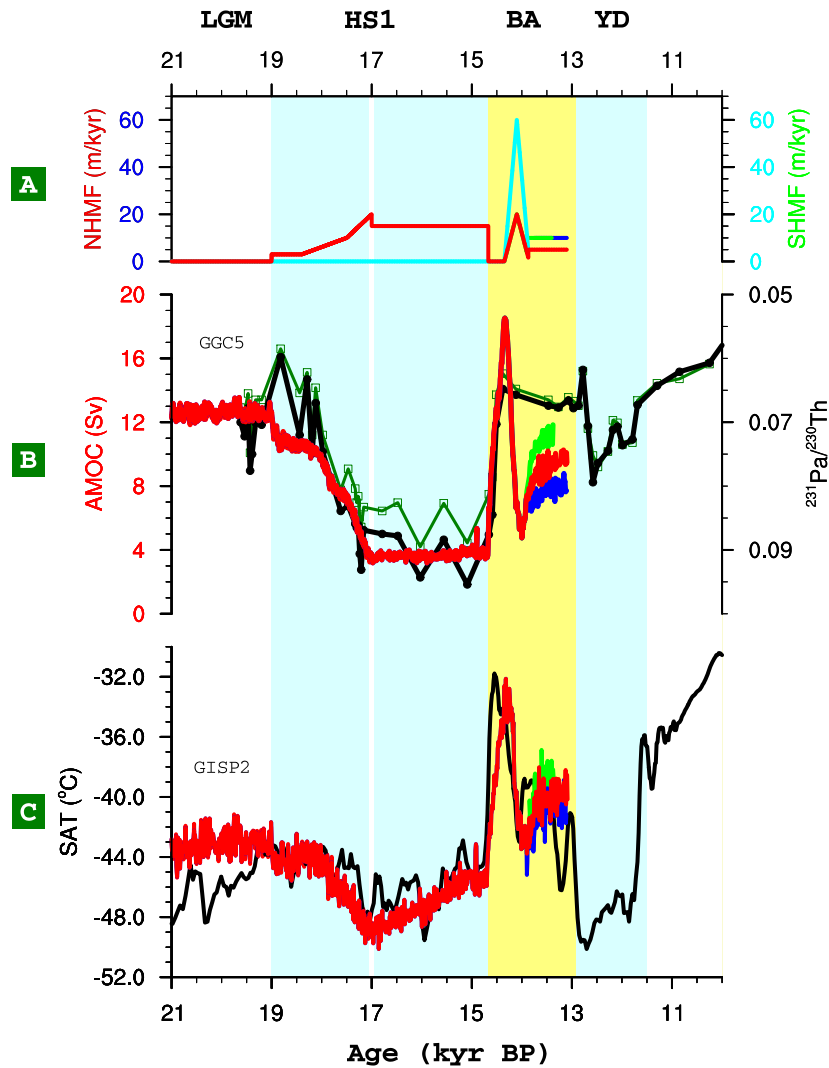
Figure 20: TraCE-21K between 21 and 13.85 ka. (**A**) NHMW (red) and SHMW (cyan) in segment TraCE-mwp-1A of TraCE-21K. Also plotted are NHMW (blue) and SHMW (green) in sensitivity experiment DGL-mwp-1A-D. (**B**) AMOC in segment TraCE-mwp-1A of TraCE-21K (red) and DGL-mwp-1A-D (blue), superimposed by AMOC reconstructions (black and green) [McManus et al., 2004]. (**C**) Greenland SAT in segment TraCE-mwp-1A of TraCE-21K (red) and DGL-mwp-1A-D (blue), superimposed by Greenland SAT reconstruction based on Greenland Ice Sheet Project 2 (GISP2) δ^{18}O with borehole temperature calibration (black) [Cuffey and Clow, 1997]. Refer to Table 4 for details of TraCE-mwp-1A and Table 5 for DGL-mwp-1A-D (Exp. 16).

Figure 21: TraCE-21K between the LGM and YD (21-12.9 ka). (**A**) NHMW (red) and SHMW (cyan) in segment TraCE-preYD of TraCE-21K. Also plotted are NHMW in sensitivity experiments DGL-mwp-1A-YD-A (blue) and DGL-mwp-1A-YD-B (green). (**B**) AMOC in segment TraCE-preYD of TraCE-21K (red) and DGL-mwp-1A-YD-A (blue) and DGL-mwp-1A-YD-B (green), superimposed by AMOC reconstructions (black and green) [McManus et al., 2004]. (**C**) Greenland SAT in segment TraCE-preYD of TraCE-21K (red) and DGL-mwp-1A-YD-A (blue) and DGL-mwp-1A-YD-B (green), superimposed by Greenland SAT reconstruction based on Greenland Ice Sheet Project 2 (GISP2) δ^{18}O with borehole temperature calibration (black) [Cuffey and Clow, 1997]. Refer to Table 4 for details of TraCE-preYD and Table 5 for DGL-mwp-1A-YD-A (Exp. 17) and DGL-mwp-1A-YD-B (Exp. 18).
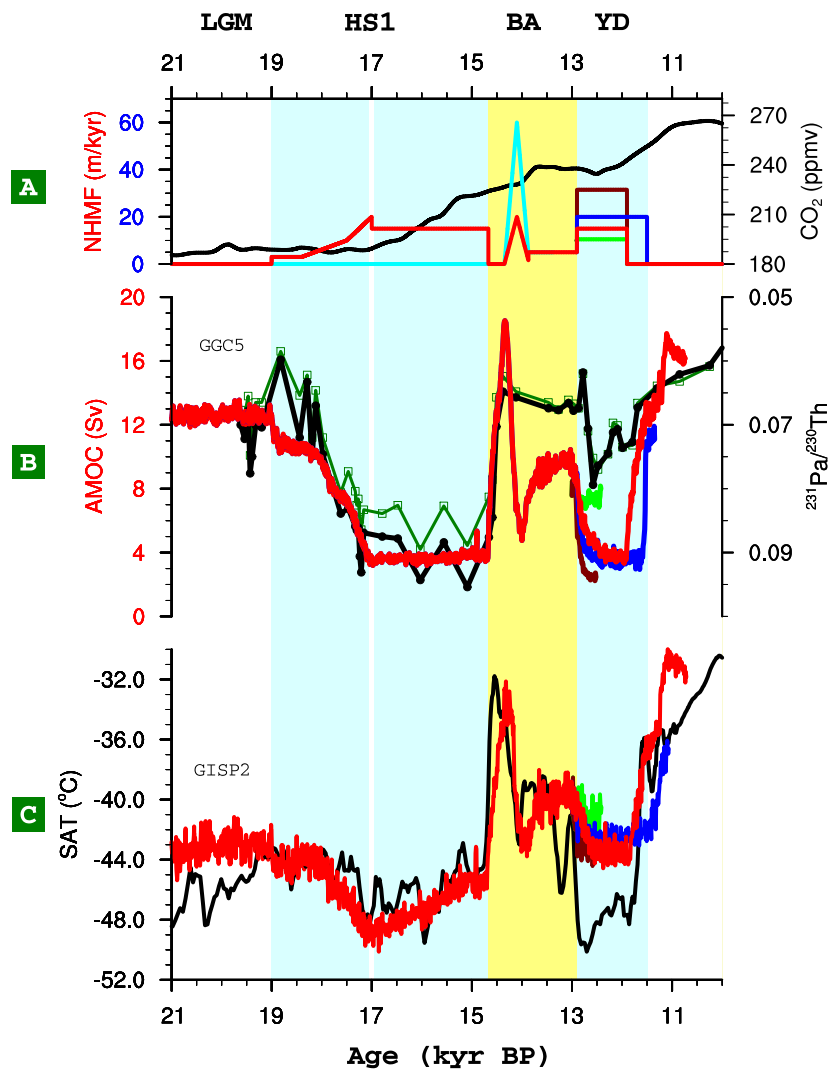
Figure 22: Sensitivity of AMOC (**B**) and Greenland SAT (**C**) to NHMW (**A**) during YD. Atmospheric CO_2 concentration [Joos and Spahni, 2008] (black) is also plotted in (**A**). Refer to Table 5 for details of the four sensitivity experiments: DGL-YD-CBS-A (green, Exp. 19), DGL-YD-CBS-B (red, Exp. 20), DGL-YD-CBS-C (blue, Exp. 21) and DGL-YD-CBS-D (dark red, Exp. 22). CBS, closed Bering Strait.
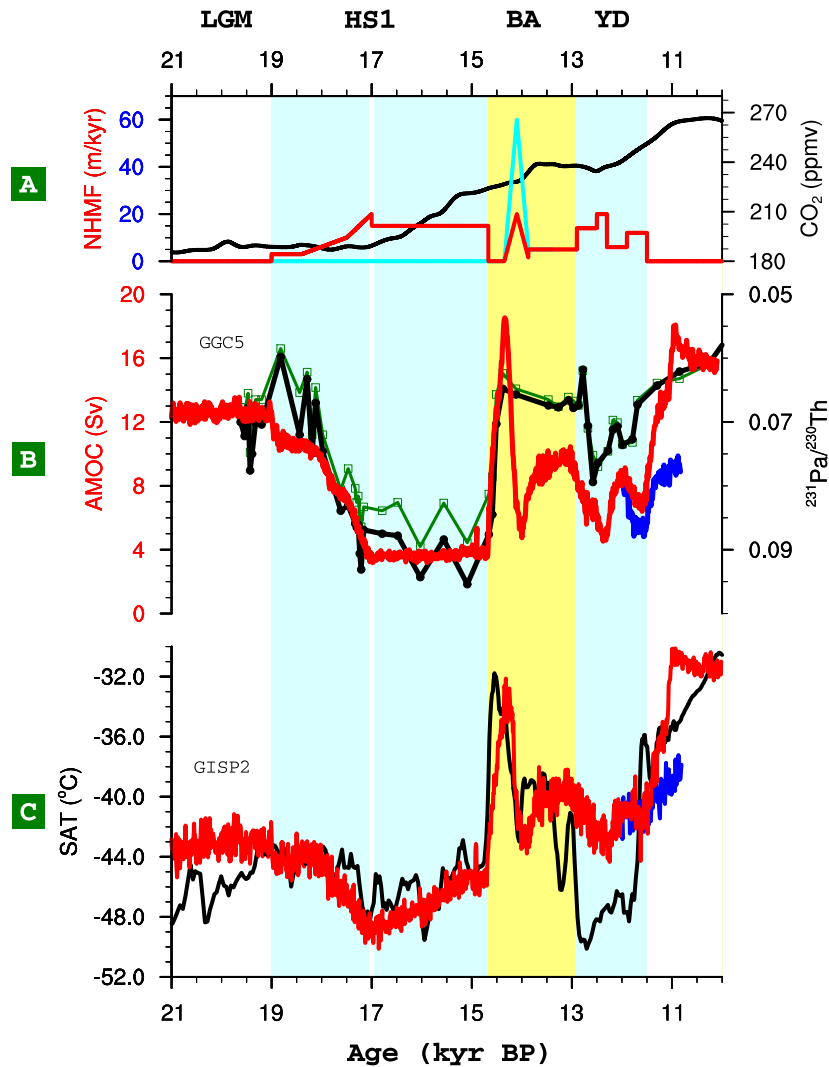
Figure 23: Sensitivity of AMOC (**B**) and Greenland SAT (**C**) to NHMW (**A**) during YD. Atmospheric CO_2 concentration [Joos and Spahni, 2008] (black) is also plotted in (**A**). Refer to Table 5 for details of the two sensitivity experiments: DGL-YD-CBS-E (red, Exp. 23), DGL-YD-OBS (blue, Exp. 24). These two experiments are subjected to the same NHMW forcing. The Bering Straits remains closed in DGL-YD-CBS-E, but opens at 12.0 ka in DGL-YD-OBS. CBS, closed Bering Strait. OBS, open Bering Strait.
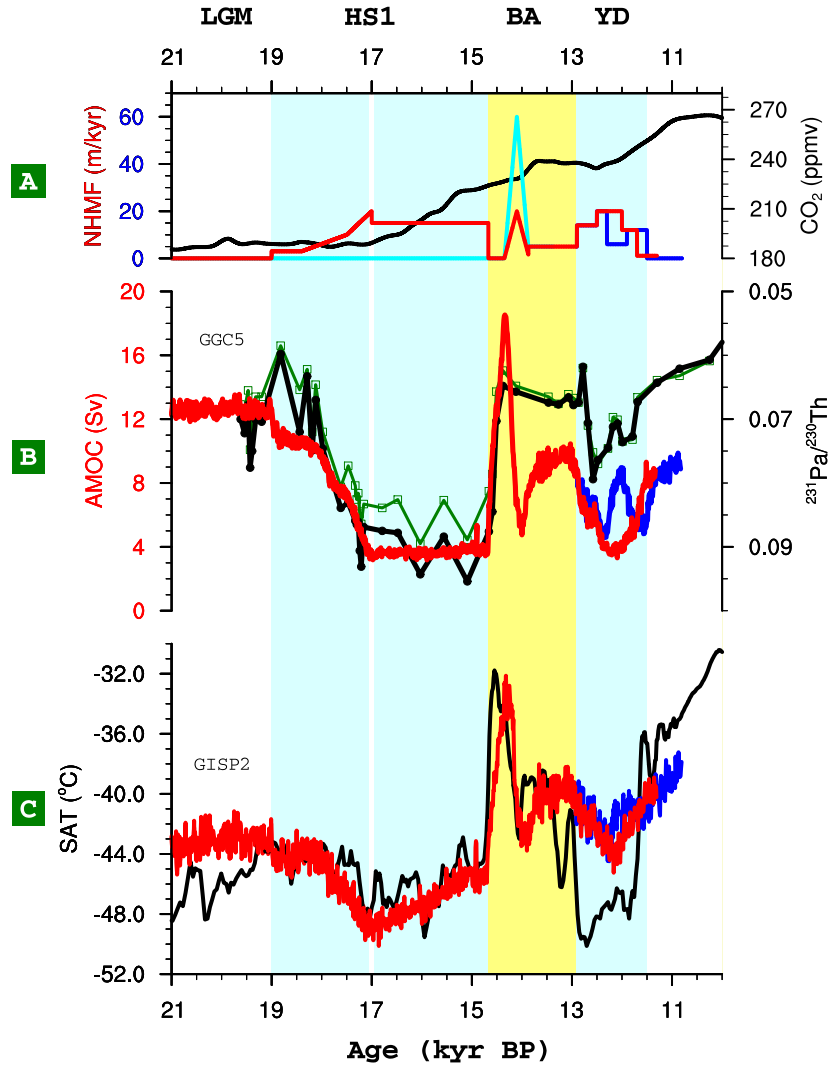
Figure 24: TraCE-21K between the LGM and the end of YD (21~11.7 ka). (**A**) Atmospheric CO_2 concentration [Joos and Spahni, 2008] (black), NHMW (red) and SHMW (cyan) in segment TraCE-YD of TraCE-21K. Also plotted is NHMW in sensitivity experiment DGL-YD-OBS (blue). (**B**) AMOC in segment TraCE-YD of TraCE-21K (red) and DGL-YD-OBS (blue), superimposed by AMOC reconstructions (black and green) [McManus et al., 2004]. (**C**) Greenland SAT in segment TraCE-YD of TraCE-21K (red) and DGL-YD-OBS (blue), superimposed by Greenland SAT reconstruction based on Greenland Ice Sheet Project 2 (GISP2) $\delta^{18}O$ with borehole temperature calibration (black) [Cuffey and Clow, 1997]. Refer to Table 4 for details of TraCE-YD and Table 5 for DGL-YD-OBS (Exp. 24). Refer to Table 1 for the land-sea configuration change in TraCE-21K based on Ice5G reconstructions.
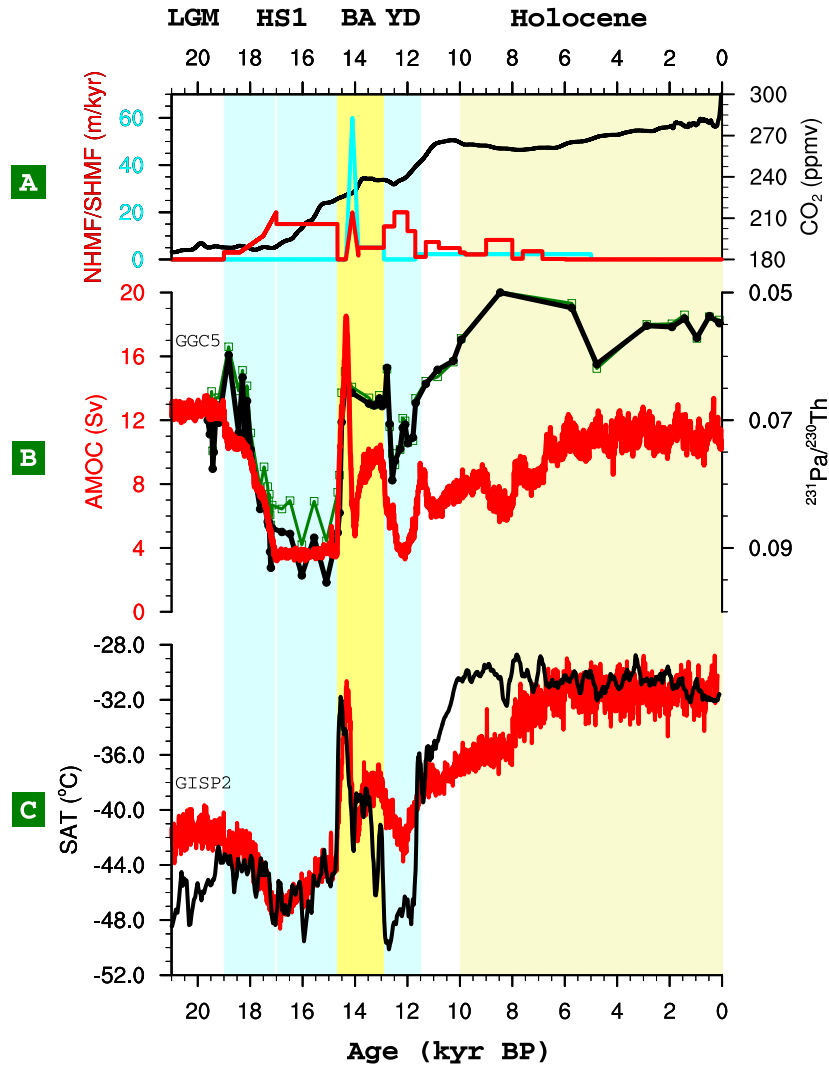
Figure 25: TraCE-Holocene in TraCE-21K. (**A**) Atmospheric CO_2 concentration [Joos and Spahni, 2008] (black), NHMW (red) and SHMW (cyan) in the complete simulation of TraCE-21K. (**B**) AMOC in the complete simulation of TraCE-21K (red), superimposed by AMOC reconstructions (black and green) [McManus et al., 2004]. (**C**) Greenland SAT in the complete simulation of TraCE-21K (red), superimposed by Greenland SAT reconstruction based on Greenland Ice Sheet Project 2 (GISP2) $\delta^{18}O$ with borehole temperature calibration (black) [Cuffey and Clow, 1997]. Refer to Table 4 for details of TraCE-Holocene, and Table 1 for the land-sea configuration change in TraCE-21K based on Ice5G reconstructions.
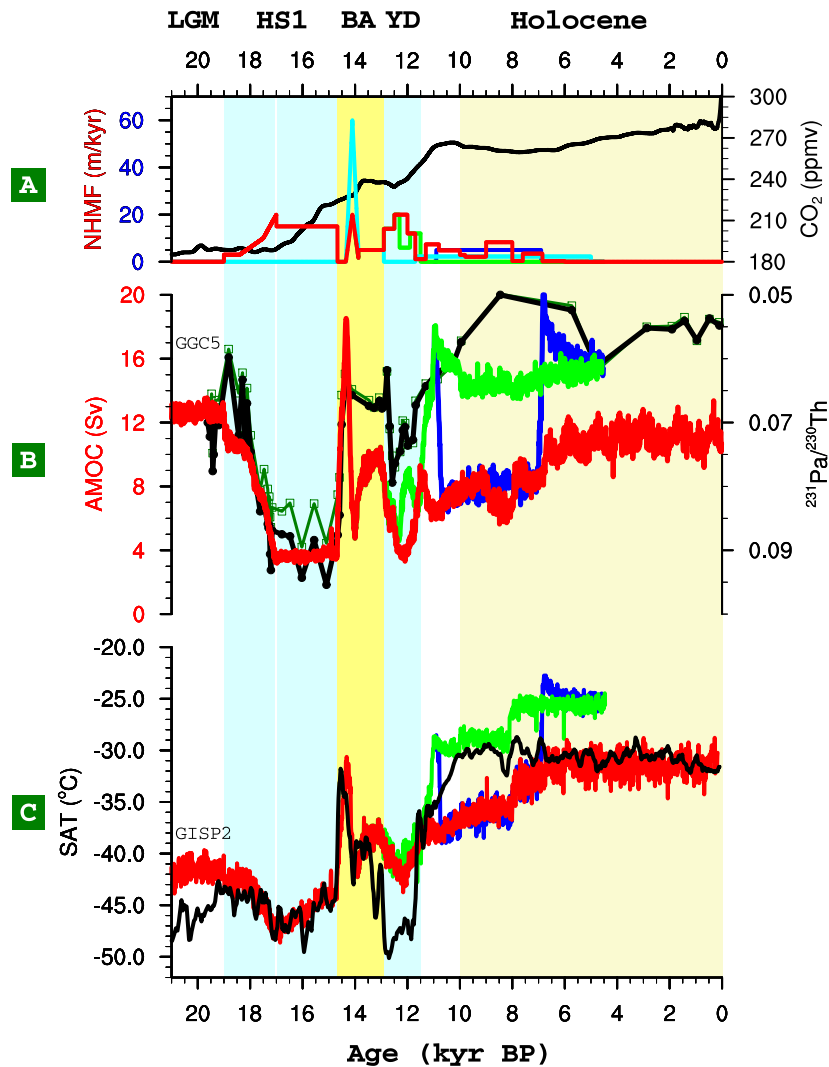
Figure 26: Sensitivity of Holocene simulation to the closing of Bering Strait (**A**) Atmospheric CO_2 concentration [Joos and Spahni, 2008] (black), NHMW (red) and SHMW (cyan) in the complete simulation of TraCE-21K. Also plotted are NHMW in sensitivity experiment Holocene-A (green) and Holocene-B (blue). (**B**) AMOC in the complete simulation of TraCE-21K (red) and sensitivity experiments Holocene-A (green) and Holocene-B (blue), superimposed by AMOC reconstructions (black and green) [McManus et al., 2004]. (**C**) Greenland SAT in the complete simulation of TraCE-21K (red) and sensitivity experiments Holocene-A (green) and Holocene-B (blue), superimposed by Greenland SAT reconstruction based on Greenland Ice Sheet Project 2 (GISP2) $\delta^{18}O$ with borehole temperature calibration (black) [Cuffey and Clow, 1997]. Refer to Table 4 for details of TraCE-Holocene, Table 5 for Holocene-A (Exp. 25) and Holocene-B (Exp. 26) and Table 1 for the land-sea configuration change in TraCE-21K based on Ice5G reconstructions.
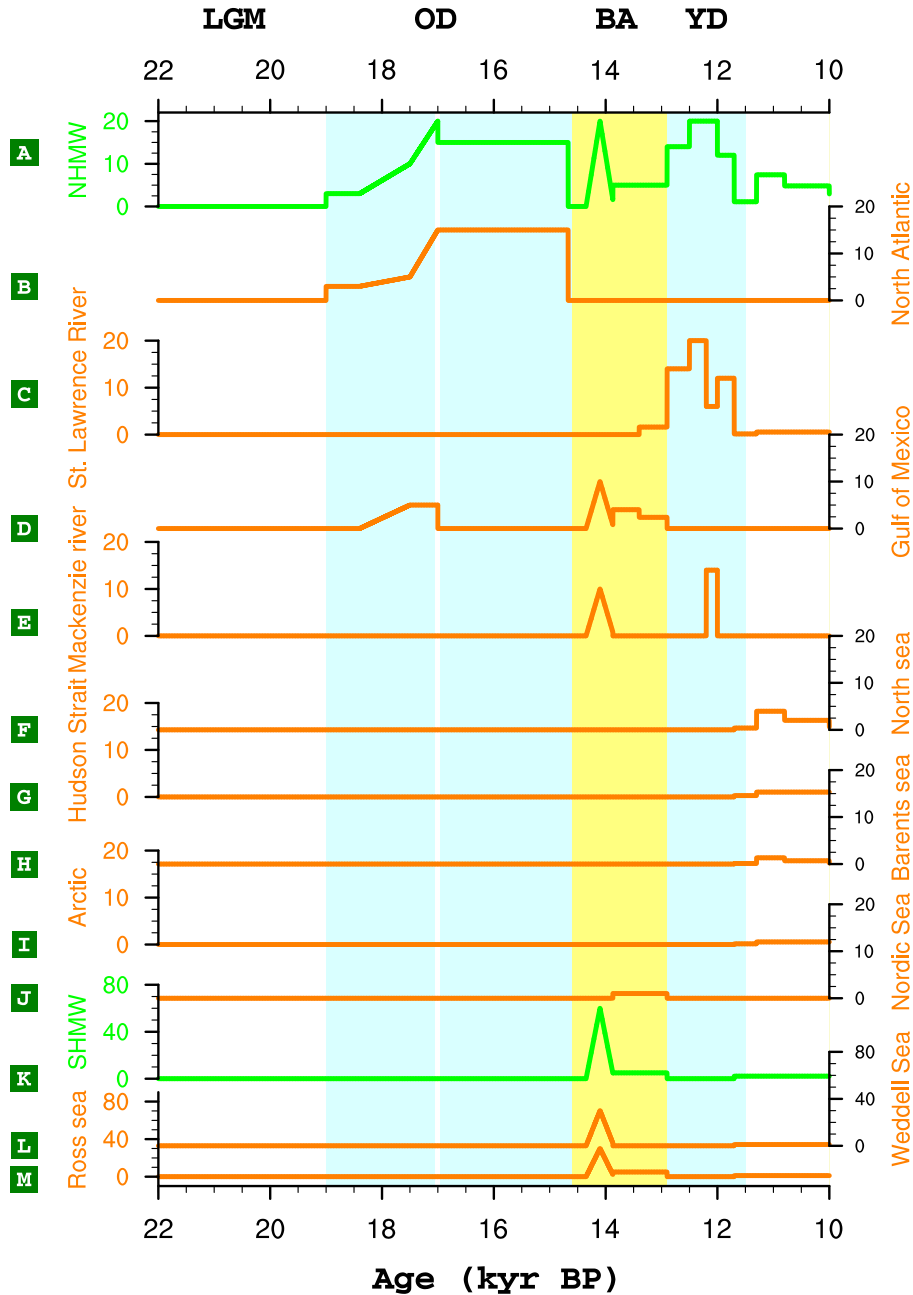
Figure 27: Meltwater forcing in the transient simulation in m/kyr (meters of global sea level rise in 1,000 years). (**A**) Total meltwater forcing from northern hemisphere, which includes the meltwater discharge into (**B**) North Atlantic between 50°N and 70°N, (**C**) St. Lawrence River, (**D**) Gulf of Mexico, (**E**) Mackenzie River, (**F**) North Sea, (**G**) Hudson Strait, (**H**) Barents Sea, (**I**) Arctic and (**J**) Nordic Sea. (**K**) Total meltwater forcing from southern hemisphere, which includes the meltwater discharge into (**L**) Weddell Sea and (**M**) Ross Sea. Refer table 3 and Fig. 28 for the exact location of meltwater discharge.
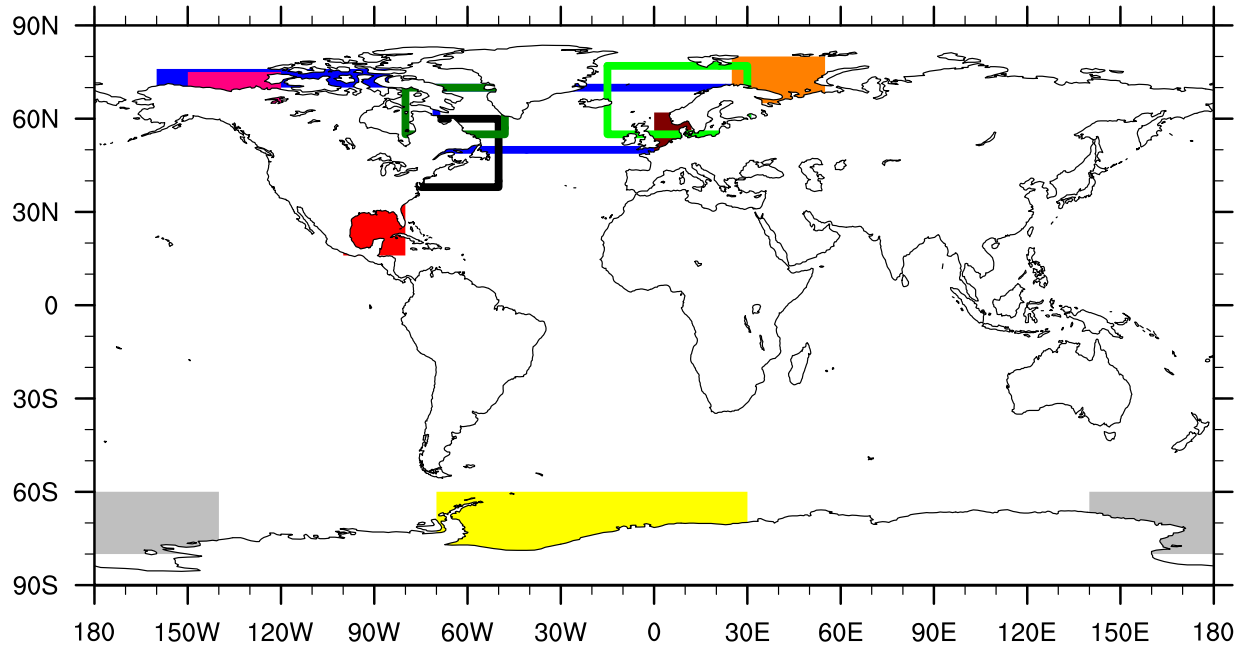
Figure 28: Location of meltwater discharge in the transient simulation: Arctic (blue shading), Mackenzie River (pink shading), Barents Sea (orange shading), Gulf of Mexico (red shading), North Sea (dark red shading), Nordic Sea (hollow green), North Atlantic between 50° and 70° N (hollow blue), Hudson Strait (hollow dark green), St. Lawrence River (hollow black), Weddell Sea (yellow shading) and Ross Sea (gray shading).

Chapter 3   The phasing of global climate responses to Northern Hemisphere meltwater discharge during the last deglaciation

3.1   Introduction

A simulation of the last deglaciation (21,000 to 10,000 years ago) using a synchronously coupled atmosphere-ocean general circulation model reproduces the structure and timing of global climate signals identified from proxy records. These results support the Milankovitch theory in showing that the last deglaciation was initiated by rising mid- to high-latitude Northern Hemisphere spring-summer insolation. The orbitally induced increase in meltwater discharge from Northern Hemisphere ice sheets causes early deglacial warming of the Southern and deep oceans through oceanic and atmospheric teleconnections, accounting for the Southern Ocean, deep-ocean and tropical Pacific lead over Northern Hemisphere temperatures. Meltwater-induced changes in deep-ocean temperature and Southern Hemisphere sea-ice extent may have also contributed to degassing of CO_2 from the ocean to the atmosphere.

The Milankovitch theory states that changes in high-latitude Northern Hemisphere (NH) summer insolation caused glacial cycles through their impact on ice-sheet mass balance [Milankovitch, 1941]. Although statistical analyses of long climate time series supported an orbital control on the Earth's climate by identifying the same periods as in the Earth's solar orbit, they posed a direct challenge to the Milankovitch theory in showing that changes in Southern Hemisphere (SH) climate were in phase with or led those in the north, including the marine $\delta^{18}O$ proxy of (largely NH) ice-volume changes [Hays et al., 1976; Imbrie et al., 1992; Imbrie et al., 1993]. Because temperature, local hydrography, and ocean transit time also affect the marine $\delta^{18}O$ signal, however, its use for evaluating the Milankovitch theory is compromised. This issue

can be circumvented by examining the ice-sheet and sea-level history of the last deglaciation, which is known directly from terrestrial [Clark et al., 2009] and paleo-shoreline [Fairbanks, 1989] records. These constraints support the theory in showing that onset of NH deglaciation began after an increase in high-latitude NH insolation but before the onset of SH warming and atmospheric CO_2 rise [Clark et al., 2009]. Nevertheless, subsequent climate changes still indicate a SH, deep-ocean and tropical Pacific Ocean lead over NH temperatures [Petit, 1999; EPICA Community Members, 2006; Charles et al., 1996; Lea et al., 2000], which is not an obvious prediction from NH insolation forcing. Two general hypotheses currently exist to explain these phase relationships. The first, consistent with Milankovitch, proposes that the initial response to orbital forcing occurs in the high-NH latitudes and is then transmitted rapidly to the Southern Ocean through North Atlantic Deep Water and changes in ocean heat transport [Imbrie et al., 1992; Alley et al., 2002; Clark et al., 2004]. The second hypothesis proposes a SH-insolation control on SH climate [Stott et al., 2007; Huybers and Denton, 2008; Timmermann et al., 2009], implying that the hemispheric responses were controlled by regional orbital forcing.

Here we use a synchronously coupled atmosphere-ocean general circulation model to test the hypothesis that high-latitude NH orbital forcing can explain the early deglacial warming of the SH and deep ocean. As the continuation of the simulation in Liu et al. [2009], we have completed the transient simulation of the last deglaciation using the NCAR-CCSM3 [Yeager et al., 2006]. Starting from a previous Last Glacial Maximum (LGM) simulation [Otto-Bliesner et al., 2006], our model was integrated from 22 ka forward (ka: 1,000 years ago). The model was forced by changes in insolation [Berger, 1978], atmospheric greenhouse gas concentrations [Joos and Spahni, 2008] (Fig. 1 A), continental ice-sheet orography and extent [Peltier, 2004],

coastlines [Peltier, 2004], and meltwater fluxes derived from NH and Antarctic ice sheets (Fig. 1, B and C). Detailed information for materials and methods is described in the supporting online material (SOM).

3.2   The trigger for the initial NHMW

The results from our transient simulation provide a rigorous test for the Milankovitch theory of NH-insolation control of the last deglaciation. Even though the deglacial increase of SH spring insolation was comparable to that of the NH summer insolation [Stott et al., 2007; Timmermann et al., 2009], during the onset of the last deglaciation (22-19 ka), mid- to high-latitude NH spring-summer insolation anomalies were ~3 times larger than those in the SH (shading in Fig. 2, A and B). As a result, NH summers warm by up to ~3 ^{o}C in the Arctic and ~5 ^{o}C over Eurasia, with an area average of 0.7 ^{o}C warming in NH mid-latitude and polar regions (Fig. 2, C and E). In contrast, the simulated area-average SH summer temperature 22-19 ka is only one-third (~0.2 ^{o}C) of that in the NH, with regional warming of less than 2 ^{o}C confined to between 90° E and 150° E of the eastern Antarctic region (Fig. 2, C and F). On the other hand, the SH summer duration in the transient simulation is mainly due to deglacial CO_2 increase, not the local insolation (Fig. 2 D and SOM Text 1), which is consistent with the relatively stable Antarctic temperature reconstruction during the Holocene [Petit, 1999; EPICA Community Members, 2006]. In summary, with realistic orbital forcing that exhibits the increase of austral spring insolation [Stott et al., 2007] and longer duration of austral summer [Huybers and Denton, 2008], our transient simulation does not produce significant warming in the SH at the onset of the last deglaciation. Instead, the last deglaciation originated in the NH due to its larger increase

of high-latitude spring-summer insolation, likely initiating the retreat of NH ice sheets 20-19 ka [Clark et al., 2009].

3.3   The simulation of deglacial climate evolution

As shown previously [Liu et al., 2009], the NH meltwater (NHMW) forcing associated with the onset of NH deglaciation ~19 ka causes the start of a decrease in the Atlantic meridional overturning circulation (AMOC) that continues to decrease in response to continued NHMW forcing associated with ongoing retreat of NH ice sheets [Dyke, 2004] and iceberg discharge during Heinrich event 1 [Bond et al., 1992], resulting in a near-collapse of the AMOC by 17.5 ka (Fig. 1 D). The reduction of the AMOC causes Oldest Dryas (OD) (19-14.5 ka) cooling in the Greenland ice core whereas the sudden termination of NHMW at 14.67 ka is responsible for the resumption of AMOC and abrupt Bølling warming (Fig. 1 E).

Our new results show that discharge during meltwater pulse 1A (mwp-1A) [Fairbanks, 1989], with 25% of the meltwater (5 m) sourced from the Northern Hemisphere and 75% (15 m) sourced from Antarctica [Bassett et al., 2005; Carlson, 2009] (Material and Method 2), causes a reduction in the AMOC and the associated cooling during the Older Dryas event at ~14 ka. The reduction of NHMW after mwp-1A causes the Allerød warm period ~14-12.9 ka, while a subsequent increase in NHMW weakens the AMOC, resulting in the Younger Dryas cold interval (~12.9-11.7 ka), although the cooling is less than that reconstructed from Greenland ice cores (SOM Text 2) (Fig. 1, C, D and E). Following the Younger Dryas, continued NH ice-sheet melting prevents AMOC from reaching the Holocene level and causes cooler Greenland surface air temperature (SAT) than proxy records in early Holocene (SOM Text 2).

Our simulated temperatures agree with the Antarctic ice-core temperature reconstructions in showing a gradual trend of deglacial warming. In particular, our simulation reproduces the early onset of Antarctic warming 19-18 ka as well as the full magnitude of deglacial warming of 8-10 $^{\circ}$C reconstructed from Antarctic ice cores (Fig. 1 J) [EPICA Community Members, 2006; Jouzel et al., 2007]. The model also simulates 500 years of cooling in response to the Antarctic contribution to mwp-1A. Although this cooling is coincident with the onset of the Antarctic Cold Reversal (ACR, ~14.5 ka), it is considerably shorter than the observed 2-kyr duration of the event. The long duration of ACR can be attributed to the resumption of NADW formation as well as the plateau of CO_2 levels during BA/ACR (SOM Text 3).

3.4   The deglacial phasing between NH, SH and Tropics

Our simulation also captures deglacial climate events reconstructed from proxy records in the Atlantic [Liu et al., 2009], Pacific and Indian oceans, including similar amplitude of deglacial warming. Consistent with sea surface temperature (SST) reconstructions [Calvo et al., 2007; Pahnke and Sachs, 2006], deglacial SST warming begins ~19 ka in the South Pacific (Fig. 1 I and SOM Text 4). In the western equatorial Pacific and Indian oceans, SST deglacial warming begins at ~17.5 ka (Fig. 1, G and H), or more than 1 kyr after warming begins in the South Pacific and Antarctic regions. When combined with results from the Antarctic region, we thus find that deglacial surface warming in the SH occurs first at high latitudes and then later at lower latitudes. Specifically, the zonal averages of the SSTs and Antarctic SATs in the transient simulation show that surface warming starts first at 19 ka in the SH polar and subpolar regions, followed by onset of warming at ~18 ka in the SH subtropics and tropics, and finally at 17 ka along the equator (Fig. 3 B).

In contrast to the southward age progression of deglacial surface warming, the deep ocean from the Southern Ocean to the equator warms synchronously at 19 ka in response to NHMW discharge (Fig. 3, A and C). The timing and amplitude of simulated global deep-ocean warming is in good agreement with a reconstruction derived from the ice-volume corrected global benthic d18O record [Clark et al., 2009] as well as with a Mg/Ca-derived ocean temperature reconstruction from 2500 m depth in the eastern tropical Pacific [Martin et al., 2005] (Fig. 4 B). The amount of simulated warming of the deep ocean, however, varies in different basins during the last deglaciation, with up to 4 ^{o}C warming in the Pacific and Indian Ocean and up to 7 ^{o}C warming in the Atlantic and Arctic basin warming (fig. S11).

The early warming of the Southern Ocean, Antarctica, and the deep ocean at ~19 ka occurs in response to the NHMW forcing associated with retreat of NH ice sheets. To further demonstrate these responses to NHMW, we performed a sensitivity experiment with a much stronger NHMW forcing (11 times that in the transient simulation) (fig. S3 A and Material and Method 3), which shows that the early warming is discernible in less than 100 years after the start of this stronger forcing (fig. S3, B and C). This rapid response in SH and deep-ocean temperatures to NHMW is caused by the bipolar seesaw (Fig. 1 F) [Crowley, 1992; Barker et al., 2009] and other climate teleconnections in the ocean and atmosphere [Huang et al., 2000; Liu and Alexander, 2007] (SOM Text 5 and 6).

In contrast to this SH response to NHMW, tropical SSTs do not begin to warm until the initial increase in atmospheric CO_2 around 17-18 ka [Stott et al., 2007; Mix et al., 1986; Lea et al., 2006] (Fig. 3, A and B) (SOM Text 7). We investigate the response of equatorial SST to deglacial CO_2 forcing using paired sensitivity experiments, one with only CO_2 and one with only

insolation as the transient forcing (Material and Method 3).   The results indicate that the insolation-only forcing cannot induce significant equatorial warming, whereas the CO_2-only transient forcing reproduces much of the observed equatorial SST deglacial evolution (fig. S4).

We next consider how our simulated changes in deep-ocean temperature and sea ice may have caused changes in atmospheric CO_2. Through its control on the mean solubility of CO_2 of the ocean [Martin et al., 2005; Kutzbach et al., 2010], the ~2.5 ^{o}C vertically averaged global ocean warming through the last deglaciation in our transient simulation (Fig. 4 B) can increase atmospheric CO_2 by ~30 ppmv, explaining 40% of the observed CO_2 rise (Fig. 4 A). SH sea ice may also affect atmosphere CO_2 by reducing air-sea gas exchange in critical areas of deep water formation [Stephens and Keeling, 2000; Fischer et al., 2010]. The simulated SH sea-ice area decreases by 50% during the last deglaciation and shows similar variability with a SH sea-ice reconstruction (Fig. 4 C) [Fischer et al., 2007]. It is notable that the deglacial changes of both ocean temperature increase and sea ice retreat occur in two stages, with two thirds of the deglacial changes occurring approximately between 19ka and BA/ACR and another one third occurring between YD and Holocene (fig. S12). We note that a similar two-stage deglacial evolution also occurred in atmospheric CO_2, with two thirds of the deglacial CO_2 rise occurring during the OD, a pause during the ACR, and another one third of deglacial rise between YD and Holocene. Since both ocean temperature and SH sea ice retreat starts 19ka as a response to NHMW (SOM Text 5 and 6), our transient simulation thus suggests that NHMW may contribute to the deglacial rise in atmospheric CO_2 through the reduction of seawater solubility from the global ocean warming and by a reduction in SH sea-ice extent via the bipolar seesaw.

3.5   Conclusions

Our transient simulation of the last deglaciation in CCSM3 reproduces the structure and timing of the major deglacial climate changes reconstructed from proxy records in Greenland, Antarctica, the tropical Pacific Ocean, the Southern Ocean, and the deep Pacific Ocean, suggesting that our model exhibits reasonable climate sensitivity in those regions and is capable of simulating abrupt climate changes. These results also demonstrate a physical mechanism that can explain the apparent inconsistency between the Milankovitch hypothesis and the early deglacial warming of the SH: the SH lead is caused by NHMW discharge (initially induced by orbital forcing) that warms the SH and cools the NH [Imbrie et al., 1992; Alley et al., 2002; Clark et al., 2004]. By causing deep-ocean warming and SH sea-ice retreat, NHMW likely also contributed to the deglacial CO_2 rise, providing an important feedback on subsequent global deglaciation.

References

Alley, R. B., E. J. Brook, and S. Anandakrishnan (2002), A northern lead in the orbital band: north-south phasing of Ice-Age events, Quaternary Science Reviews, 21(1), 431-441.

Bard, E., B. Hamelin, M. Arnold, L. Montaggioni, and G. Cabioch (1996), Deglacial sea-level record from Tahiti corals and the timing of global meltwater discharge, Nature, 382, 241.

Bard, E., F. Rostek, and C. Sonzogni (1997), Interhemispheric synchrony of the last deglaciation inferred from alkenone palaeothermometry, Nature, 385, 707.

Barker, S., P. Diz, M. J. Vautravers, J. Pike, G. Knorr, I. R. Hall, and W. S. Broecker (2009), Interhemispheric Atlantic seesaw response during the last deglaciation, Nature, 457(7233), 1097-1102.

Bassett, S. E., G. A. Milne, J. X. Mitrovica, and P. U. Clark (2005), Ice Sheet and Solid Earth Influences on Far-Field Sea-Level Histories, Science, 309(5736), 925-928, doi: 10.1126/science.1111575.

Berger, A. L. (1978), Long-Term Variations of Daily Insolation and Quaternary Climatic Changes, J.Atmos.Sci., 35(12), 2362-2367.

Bond, G., H. Heinrich, W. Broecker, L. Labeyrie, and J. McManus (1992), Evidence for massive discharges of icebergs into the North Atlantic ocean during the last glacial period, Nature, 360, 245.

Calvo, E., C. Pelejero, P. De Deckker, and G. A. Logan (2007), Antarctic deglacial pattern in a 30 kyr record of sea surface temperature offshore South Australia, Geophys.Res.Lett., 34(13), L13707, doi: 10.1029/2007GL029937.

Carlson, A. E. (2009), Geochemical constraints on the Laurentide Ice Sheet contribution to Meltwater Pulse 1A, Quaternary Science Reviews, 28(17-18), 1625-1630, doi: DOI: 10.1016/j.quascirev.2009.02.011.

Charles, C. D., J. Lynch-Stieglitz, U. S. Ninnemann, and R. G. Fairbanks (1996), Climate connections between the hemispheres revealed by deep sea sediment core/ice core correlations, Earth Planet.Sci.Lett., 142, 19.

Clark, P. U., A. S. Dyke, J. D. Shakun, A. E. Carlson, J. Clark, B. Wohlfarth, J. X. Mitrovica, S. W. Hostetler, and A. M. McCabe (2009), The Last Glacial Maximum, Science, 325(5941), 710-714, doi: 10.1126/science.1172873.

Clark, P. U., A. M. McCabe, A. C. Mix, and A. J. Weaver (2004), Rapid Rise of Sea Level 19,000 Years Ago and Its Global Implications, Science, 304(5674), 1141-1144, doi: 10.1126/science.1094449.

Crowley, T. J. (1992), North Atlantic deep water cools the southern hemisphere, Paleoceanography, 7, 489.

Cuffey, K. M., and G. D. Clow (1997), Temperature, accumulation, and ice sheet elevation in central Greenland through the last deglacial transition, Journal of Geophysical Research, 102(C12), 26383-26396.

Dyke, A. S. (2004), An outline of North American deglaciation with emphasis on central and northern Canada, in Developments in Quaternary Science edited by J. Ehlers and P.L. Gibbard, pp. 373-424, Elsevier, .

EPICA Community Members (2006), One-to-one coupling of glacial climate variability in Greenland and Antarctica, Nature, 444(7116), 195-198.

Fairbanks, R. G. (1989), A 17,000-year glacio-eustatic sea level record: influence of glacial melting rates on the Younger Dryas event and deep-ocean circulation, Nature, 342(6250), 637-642.

Fischer, H., et al (2007), Reconstruction of millennial changes in dust emission, transport and regional sea ice coverage using the deep EPICA ice cores from the Atlantic and Indian Ocean sector of Antarctica, Earth Planet.Sci.Lett., 260(1-2), 340-354, doi: DOI: 10.1016/j.epsl.2007.06.014.

Fischer, H., et al (2010), The role of Southern Ocean processes in orbital and millennial CO_2 variations – A synthesis, Quaternary Science Reviews, 29(1-2), 193-205, doi: DOI: 10.1016/j.quascirev.2009.06.007.

Hanebuth, T., K. Stattegger, and P. M. Grootes (2000), Rapid Flooding of the Sunda Shelf: A Late-Glacial Sea-Level Record, Science, 288(5468), 1033-1035, doi: 10.1126/science.288.5468.1033.

Hays, H. D., J. Imbrie, and N. J. Shackleton (1976), Variations in the earth's orbit: pacemaker of the ice ages, Science, 194, 1121.

Huang, R. X., M. A. Cane, N. Naik, and P. Goodman (2000), Global adjustment of the thermocline in response to deepwater formation, Geophys.Res.Lett., 27(6), 759-762, doi: 10.1029/1999GL002365.

Huybers, P., and G. Denton (2008), Antarctic temperature at orbital timescales controlled by local summer duration, Nature Geosci, 1(11), 787-792.

Imbrie, J., A. Berger, E. A. Boyle, S. C. Clemens, and A. Duffy (1993), On the structure and origin of major glaciation cycles: 2. The 100,000-year cycle, Paleoceanography, 8, 699.

Imbrie, J., E. A. Boyle, S. C. Clemens, A. Duffy, and W. R. Howard (1992), On the structure and origin of major glaciation cycles 1. Linear responses to Milankovitch forcing, Paleoceanography, 7, 701.

Joos, F., and R. Spahni (2008), Rates of change in natural and anthropogenic radiative forcing over the past 20,000 years, Proceedings of the National Academy of Sciences, 105(5), 1425-1430, doi: 10.1073/pnas.0707386105.

Jouzel, J., et al (2007), Orbital and Millennial Antarctic Climate Variability over the Past 800,000 Years, Science, 317(5839), 793-796, doi: 10.1126/science.1141038.

Kutzbach, J., W. Ruddiman, S. Vavrus, and G. Philippon (2010), Climate model simulation of anthropogenic influence on greenhouse-induced climate change (early agriculture to modern): the role of ocean feedbacks, Clim.Change, 99(3), 351-381.

Lea, D. W., D. K. Pak, C. L. Belanger, H. J. Spero, M. A. Hall, and N. J. Shackleton (2006), Paleoclimate history of Galápagos surface waters over the last 135,000 yr, Quaternary Science Reviews, 25(11-12), 1152-1167, doi: DOI: 10.1016/j.quascirev.2005.11.010.

Lea, D. W., D. K. Pak, and H. J. Spero (2000), Climate Impact of Late Quaternary Equatorial Pacific Sea Surface Temperature Variations, Science, 289(5485), 1719-1724, doi: 10.1126/science.289.5485.1719.

Liu, Z., et al (2009), Transient Simulation of Last Deglaciation with a New Mechanism for Bølling-Allerød Warming, Science, 325(5938), 310-314, doi: 10.1126/science.1171041.

Liu, Z., and M. Alexander (2007), Atmospheric bridge, oceanic tunnel, and global climatic teleconnections, Rev.Geophys., 45(2), RG2005, doi: 10.1029/2005RG000172.

Martin, P., D. Archer, and D. W. Lea (2005), Role of deep sea temperature in the carbon cycle during the last glacial, Paleoceanography, 20(2), PA2015.

McManus, J. F., R. Francois, J. M. Gherardi, L. D. Keigwin, and S. Brown-Leger (2004), Collapse and rapid resumption of Atlantic meridional circulation linked to deglacial climate changes, Nature, 428(6985), 834-837.

Milankovitch, M. (1941), Kanon der Erdbestrahlung und seine Anwendung auf das Eiszeitenproblem, Royal Serbian Academy Special Publication 132, Belgrade, Serbia.

Mix, A. C., W. F. Ruddiman, and A. McIntyre (1986), Late Quaternary paleoceanography of the tropical Atlantic, 1: Spatial variability of annual mean sea-surface temperatures, 0-20,000 years bp, Paleoceanography, 1, 43.

Otto-Bliesner, B. L., E. C. Brady, G. Clauzet, R. Tomas, S. Levis, and Z. Kothavala (2006), Last Glacial Maximum and Holocene Climate in CCSM3, J.Clim., 19(11), 2526-2544.

Pahnke, K., and J. P. Sachs (2006), Sea surface temperatures of southern midlatitudes 0–160 kyr B.P, Paleoceanography, 21(2), PA2003, doi: 10.1029/2005PA001191.

Peltier, W. R. (2004), Global glacial isostasy and the surface of the ice-age Earth- The ICE-5 G(VM 2) model and GRACE, Annu.Rev.Earth Planet.Sci., 32(1), 111-149.

Peltier, W. R., and R. G. Fairbanks (2006), Global glacial ice volume and Last Glacial Maximum duration from an extended Barbados sea level record, Quaternary Science Reviews, 25(23-24), 3322-3337.

Petit, J. R. (1999), Climate and atmospheric history of the past 420,000 years from the Vostok ice core, Antarctica, Nature, 399, 429-436.

Stephens, B. B., and R. F. Keeling (2000), The influence of Antarctic sea ice on glacial-interglacial CO 2 variations, Nature, 404(6774), 171-174.

Stott, L., A. Timmermann, and R. Thunell (2007), Southern Hemisphere and Deep-Sea Warming Led Deglacial Atmospheric CO_2 Rise and Tropical Warming, Science, 318(5849), 435-438.

Timmermann, A., O. Timm, L. Stott, and L. Menviel (2009), The Roles of CO_2 and Orbital Forcing in Driving Southern Hemispheric Temperature Variations during the Last 21 000 Yr*, J.Clim., 22(7), 1626-1640.

Yeager, S. G., C. A. Shields, W. G. Large, and J. J. Hack (2006), The Low-Resolution CCSM3, J.Clim., 19(11), 2545-2566.

Yokoyama, Y., K. Lambeck, P. De Deckker, P. Johnston, and L. K. Fifield (2000), Timing of the Last Glacial Maximum from observed sea-level minima, Nature, 406(6797), 713-716.
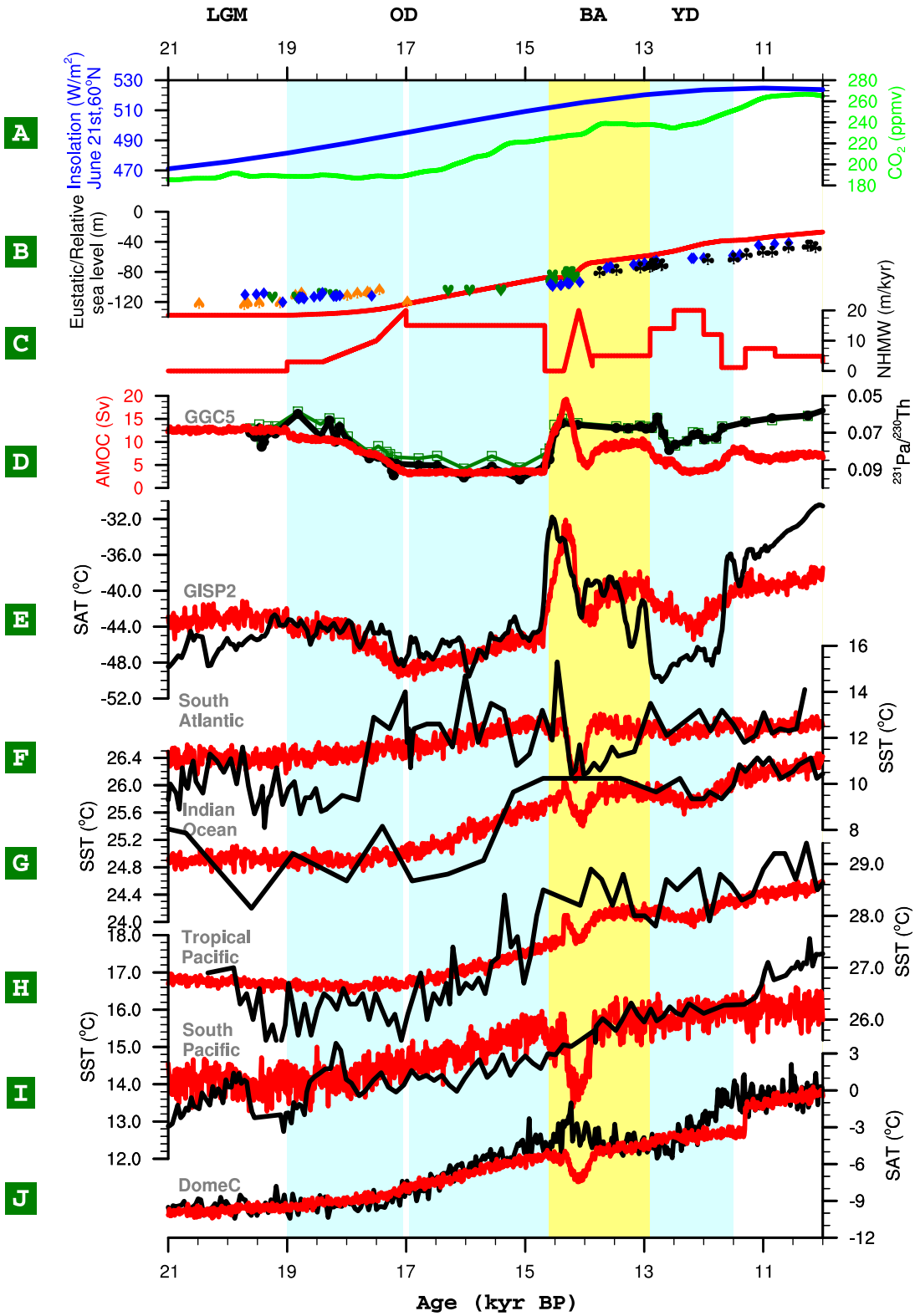
Figures

Figure 1: Data-model comparison for several benchmark time series. (**A**) June 21st insolation at 60°N (blue) [Berger, 1978] and atmospheric CO_2 concentration (green) [Joos and Spahni, 2008]. (**B**) Relative sea level from the reconstruction and eustatic sea level in the model (red). Sea level data are from Barbados (blue) [Peltier and Fairbanks, 2006], Bonaparte Gulf (orange) [Yokoyama et al., 2000], Sunda Shelf (green) [Hanebuth et al., 2000] and Tahiti (black) [Bard et al., 1996]. (**C**) NHMW fluxes in the model. (**D**) Pa/Th ratio at Bermuda as a proxy for AMOC export [McManus et al., 2004], and model maximum AMOC transport (below 500 m). Sv, Sverdrup (1 Sverdrup = 10^6 m^3 s^{-1}). (**E**) Greenland SAT based on GISP2 $\delta^{18}O$ reconstruction with borehole temperature calibration [Cuffey and Clow, 1997] and in the model (model offset by −4.5°C). (**F**) SST from the South Atlantic [Barker et al., 2009] and model (offset by 2.9°C). (**G**) SST from Southwest Indian Ocean [Bard et al., 1997] and model (offset by 2°C). (**H**) SST from the West Pacific warm pool (core MD98-2176) [Stott et al., 2007] and model (offset by -0.4°C). (**I**) SST off New Zealand [Pahnke and Sachs, 2006] and model (offset by 0.9°C). (**J**) Antarctic SAT from Dome C δD reconstruction [Jouzel et al., 2007] and model. In (**D**) to (**J**), black for the reconstruction, and red for transient simulation. All model variables are shown in 10 year averages. Overall, model simulations are in good agreement with the proxy records. BP, before present.
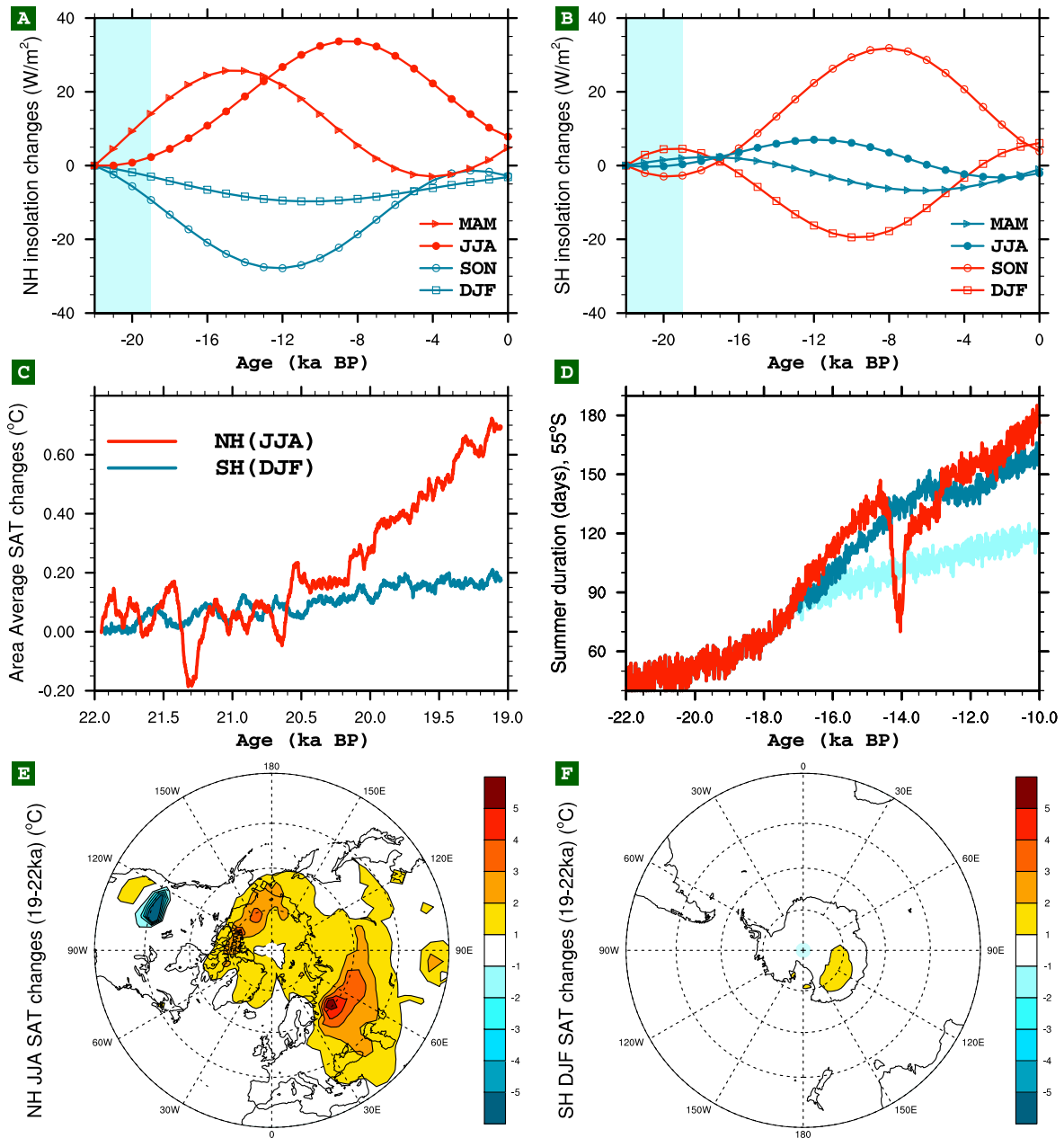
Figure 2: Local summer SAT changes at the end of LGM in the transient simulation. (**A**) Changes of area average of NH mid-high latitude (40~90° N) insolation at the top of the atmosphere in seasonal averages: MAM (triangle), JJA (filled circle), SON (open circle), DJF (square). (**B**), Same as (**A**), but for 40~90° S in SH. (**C**) Changes of area average of local summer SAT in NH (red) and SH (blue) mid-high latitude in 10 year averages. (**D**) Summer duration at 55° S with all (red), CO_2-only (blue) and orbit-only (light blue) forcing. (**E**, **F**), pattern of local summer SAT changes between 19 and 22ka in NH (E) and SH (F).
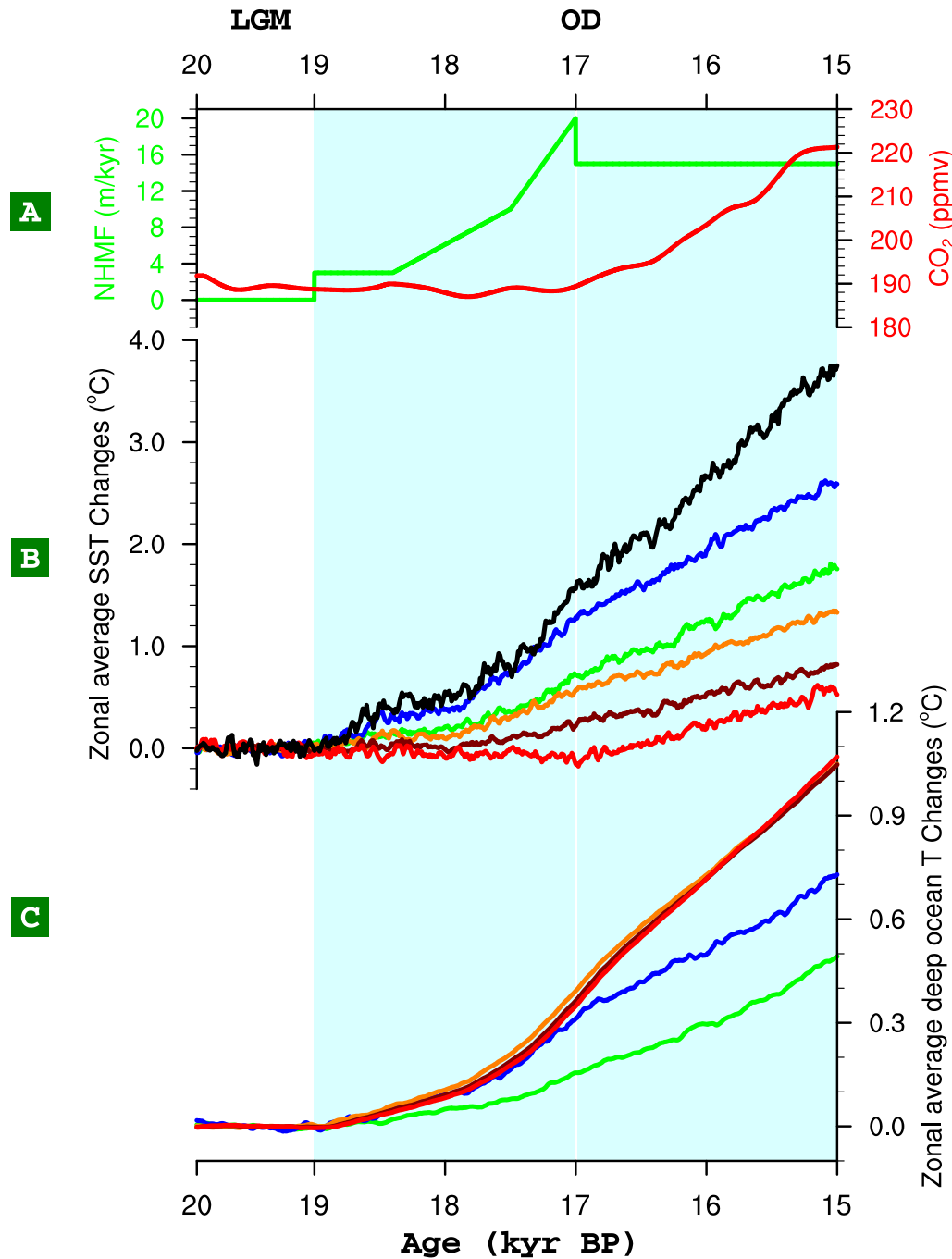
Figure 3: Southern hemisphere deglacial warming in transient simulation (20~15ka). (**A**) NHMW fluxes in the model (green) and atmospheric CO_2 concentration (red) [Joos and Spahni, 2008]. (**B**) Zonal average of Antarctic SAT at 80° S (black), Southern Ocean SST at 55° S (green), 45° S (blue) and Pacific SST at 30° S (orange), 15° S (dark red) and 0° S (red). All model variables are anomalies in 10-year averages with reference to the average value between 20 and 19ka. (**C**) Same as (**A**), but for deep ocean temperature at 2300 m depth.
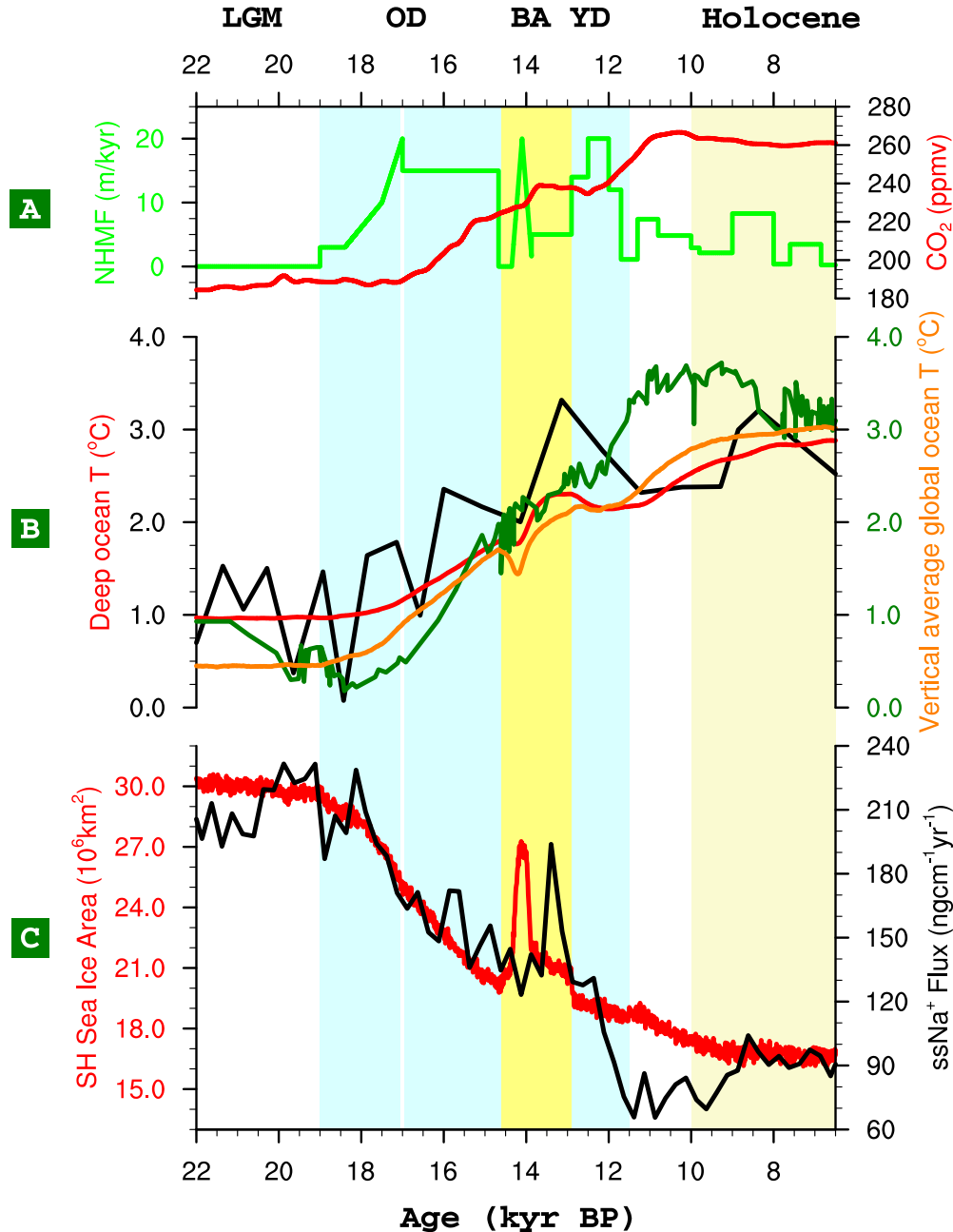
Figure 4: Deglacial evolution of ocean temperature and SH sea ice area from both the transient simulation and proxy data. (**A**) NHMW fluxes in the model (green) and atmospheric CO_2 concentration (red) [Joos and Spahni, 2008]. (**B**) Deep ocean temperature from eastern equatorial Pacific (black) [Martin et al., 2005] and model (red, offset by 2.5°C), overlaid with global mean ocean temperature in the model (orange) and proxy reconstruction (green) [Clark et al., 2009].

(**C**) SH sea ice area from sea salt Na$^+$ (ssNa) reconstruction in 250-year averages (black) [Fischer et al., 2007] and model (red). All model variables are shown in 10 year averages. Overall, model simulations are in good agreement with the proxy records.

Supporting online material (SOM)

3.6   Materials and method

3.6.1 Model Setup

The coupled general circulation model (CGCM) employed is the Community Climate System Model version 3 (CCSM3), centered at the National Center for Atmospheric Research (NCAR). CCSM3 is a global, coupled ocean–atmosphere–sea ice–land surface climate model without flux adjustment [Collins et al., 2006]. All the simulations were performed with T31_gx3v5 resolution [Yeager et al., 2006] that includes a dynamic global vegetation module. The atmospheric model is the Community Atmospheric Model 3 (CAM3) with 26 hybrid coordinate levels in the vertical and ~3.75-degree resolution in the horizontal. The land model uses the same resolution as the atmosphere, and each grid box includes a hierarchy of land units, soil columns, and plant types. Glaciers, lakes, wetlands, urban areas, and vegetated regions can be specified in the land units. The ocean model is the NCAR implementation of the Parallel Ocean Program (POP) in vertical z-coordinate with 25 levels. The longitudinal resolution is 3.6-degrees and the latitudinal resolution is variable, with finer resolution near the equator (~0.9 degrees). The sea ice model is the NCAR Community Sea Ice Model (CSIM). CSIM is a dynamic-thermodynamic model that includes a subgrid-scale ice thickness distribution. The resolution of CSIM is identical to that of POP. The preindustrial control simulation reproduces the major features of global climate, most notably in the deep ocean [Otto-Bliesner et al., 2006]. The Last Glacial Maximum (LGM) CCSM3 simulation has a global cooling of 4.5 °C compared to pre-industrial with amplification of this cooling at high latitudes and over continental ice sheets [Otto-Bliesner et al., 2006]. The LGM control run also simulates a shoaling of North

Atlantic Deep Water and farther northward penetration of Antarctic Bottom Water [Otto-Bliesner et al., 2007]. A 1,800-year LGM equilibrium simulation was branched off from an earlier LGM simulation in order to incorporate the dynamic global vegetation model (DGVM) and to reduce the model drift in the deep ocean. The transient simulation was then started at the end of the 1,800-year LGM/DGVM equilibrium run with transient orbital parameter starting at 22 ka (ka: 1,000 years ago). The transient concentrations of the greenhouse gases (CO_2, CH_4 and N_2O) were adopted from Joos and Spahni [2008]. The continental ice sheets were modified approximately once per 500 years according to the ICE-5G reconstruction [Peltier, 2004]. The coastlines at LGM were also taken from the ICE-5G reconstruction, and were modified at 13.1 ka with the removal of the Fennoscandian ice sheet from the Barents Sea and at 12.9 ka with the opening of the Bering Strait.

3.6.2 Meltwater Scheme

One of the challenges of last deglacial simulation is the poor knowledge of meltwater fluxes from retreating ice sheets. Although sea-level records provide globally integrated information on meltwater fluxes, they have relatively large (up to 6 m sea-level equivalent volume) uncertainties and do not constrain the location(s) of meltwater discharge to the ocean. In our transient simulation, we paid special attention to the meltwater forcing during millennial-scale events, such as the Bølling-Allerød (BA) warm periods, meltwater pulse 1A (mwp-1A), the Younger Dryas (YD) cold event, etc. At each millennial event, we performed several sensitivity experiments with the same initial condition, but different meltwater schemes in terms of the location and the rate of meltwater discharge. We chose the simulation to continue the transient simulation that best matched the proxy records of sea-level rise, Atlantic meridional overturning

circulation (AMOC) and Greenland surface air temperature (SAT). The results shown here are a continuation of the DGL-A meltwater scheme in Liu et al. [2009] into the early Holocene (SOM Table, figs. S1 and S2). Meltwater fluxes from the retreating ice sheets were derived from the record of sea level rise [Peltier and Fairbanks, 2006; Yokoyama et al., 2000; Clark et al., 2004; Bard et al., 2010] and geological indicators of ice-sheet retreat and meltwater discharge [Clark et al., 2004; Clark et al., 2002; Licciardi et al., 1999; Clark et al., 2001; Carlson et al., 2007; Carlson, 2008; Carlson et al., 2009; Clark et al., 2009; Carlson, 2009; Obbink et al., 2010]. The meltwater forcing during mwp-1A includes contributions from the Antarctic (15 m of equivalent sea-level volume) and Laurentide (5 m of equivalent sea-level volume) Ice Sheets [Clark et al., 2002; Carlson, 2009; Bassett et al., 2005]. Any larger (>5 m) Northern Hemisphere contribution results in a complete shutdown of AMOC and is inconsistent with proxy records [McManus et al., 2004; Stanford et al., 2006; Praetorius et al., 2008], which constrains the northern hemisphere's contribution to be <25 % of the total meltwater pulse volume (~20 m). We also adopted the sequence of freshwater discharge of Carlson et al. [2007] for the Younger Dryas.

3.6.3   Sensitivity experiments

Our simulation of the Transient Climate Evolution of the past 21,000 years (TraCE-21K) is driven by transient changes in the Earth's orbit configuration, meltwater discharge, atmospheric CO_2 and other greenhouse gasses (CH_4 and N_2O) as well as discrete changes of ice sheet and marginal seas. In order to better understand the climate sensitivity to individual climate forcing, we performed several sensitivity experiments to estimate the contribution of a single transient forcing to TraCE-21K.

3.6.3.1 TraCE-19ka

This sensitivity experiment was branched off at 19 ka from TraCE-21K and was integrated for 300 years with fixed forcing (fig. S3). We use the values at 19 ka for both the orbital forcing and greenhouse gas concentration. The discharge of Northern hemisphere meltwater (NHMW) in TraCE-19ka goes into the same region as TraCE-21K, but the intensity of NHMW in TraCE-19ka is 11 times larger than that in TraCE-21K.

3.6.3.2 TraCE-CO$_2$ and TraCE-Orbit

In TraCE-21K, marginal seas were not modified between 17 and 15 ka and the changes of the NH ice sheets during these 2,000 years were minimal in this low-resolution version of CCSM3. We also applied a constant flux of NHMW to maintain AMOC in the collapsed state (Fig. 1, C and D). Thus, the transient climate evolution 17-15ka is attributable to changes in Earth's orbit and greenhouse gases (mainly CO$_2$). Two experiments were performed, each with only one of the above transient forcing (fig. S4). Experiment TraCE-CO$_2$ branched off at 17ka from TraCE-21K, and was driven only by transient changes in greenhouse gas concentrations with all other forcing kept at 17 ka values. TraCE-Orbit is similar to TraCE-CO$_2$ where only orbital forcing continues to change after 17 ka with all other forcing kept constant at 17 ka values.

3.7   Supporting online text

3.7.1   SH summer duration mainly controlled by deglacial atmospheric CO_2 rise

Huybers and Denton [Huybers and Denton, 2008] proposed that the deglacial warming in the Southern Hemisphere (SH) polar region is caused by the deglacial increase of local summer duration. Based on one constant insolation threshold throughout the last 350,000 years, the calculated SH summer duration has been shown to covary with the Northern Hemisphere (NH) insolation intensity, which increased during the last deglaciation and decreased during the Holocene.

In Huybers and Denton [2008], the summer duration is defined as the number of days whose diurnal average insolation exceeds certain constant threshold. This constant insolation threshold is selected based on the modern day temperature-insolation relationship: the surface temperature is near $0^{o}C$ when the insolation intensity reaches this threshold [Huybers, 2006]. In this way, the definition of summer duration is essentially the time interval when the surface temperature is above zero, which can be explicitly calculated in our transient simulations. However, we find the variability of SH summer duration in our transient simulation exhibits different evolution from the calculation in Huybers and Denton [2008]: even though the SH summer duration in the polar region increases during the last deglaciation, it keeps at a constant level throughout the Holocene (fig. S5 A). We also find the simulated integrated summer energy also increases during the last deglaciation, but keeps at a constant level during the Holocene (fig. S5 B).

Here, we argue that it is not valid to use constant insolation threshold in calculating summer duration for the past 350,000 years. Instead, the insolation threshold should vary in

different climates. For example, 275 W m^{-2} is used as the threshold for the calculation of the NH polar region summer duration based on the modern day temperature-insolation relationship [Huybers, 2006]. The correspondence between 0°C surface temperature and 275 W m^{-2} insolation is expected to fail at LGM, simply because the temperature is not only determined by the local insolation, but also by other factors, such as atmospheric CO_2. In fact, our transient simulation demonstrates that the insolation threshold increases more than 300% from 60 to 250 W m^{-2} at polar regions from the modern climate to the LGM (fig. S5 C).

We investigate the deglacial evolution of SH summer duration using paired sensitivity experiments, one with only CO_2 and one with only insolation as the transient forcing (Material and Method 3). The results indicate that the CO_2-only transient forcing (blue in Fig. 2 D) reproduces much of the summer duration change found in the transient simulation with all forcing (red in Fig. 2 D), and the insolation-only forcing plays only the secondary role in deglacial increase of SH summer duration (light blue in Fig. 2 D). In addition to CO_2 and orbit forcing, we also find meltwater discharges also have a significant impact on the SH summer duration. For example, the substantial increase of SH summer duration starts ~19 ka due to the increase of the SH surface temperature, which itself is caused by the bipolar seesaw response to NHMW (Fig. 3 and SOM Text 5-6). On the other hand, the meltwater discharge from Antarctica also significantly reduces the SH summer duration during mwp-1A.

3.7.2   Discrepancies between transient simulation and proxy data

In the transient simulation of the last deglaciation, there are several major discrepancies between the model and proxy data. Notable discrepancies between model and proxy records exist in Greenland during YD and early Holocene.

It remains a challenge for the climate model to produce Heinrich event 1 (H1)-like YD cooling when CO_2 has increased by 50 ppmv (parts per million by volume) between H1 and YD (Fig. 1 E). For the beginning of the Holocene at 10 ka, the deglacial warming in the transient simulation does not reach the Holocene level because the sea level is still rising and considerable NHMW from the remaining Laurentide Ice Sheet keeps the AMOC in a weaker state and produces lower Greenland SAT than proxy record (Fig. 1 E). Alternatively, the Greenland δ^{18}O-temperature calibration may not account for changes in precipitation source. Indeed, LeGrande and Schmidt [2009] showed a breakdown in the calibration during the early Holocene (i.e. colder temperatures but higher δ^{18}O values) due to the rapid thinning and retreat of the Laurentide Ice Sheet. Similarly, Summit Greenland borehole SAT reconstructions show continued warming until 8 ka [Dahl-Jensen et al., 1998] while the Greenland δ^{18}O records have relatively constant values starting at ~10 ka. Thus this disagreement may not necessarily be due to model error but rather assumptions that go into converting δ^{18}O to temperature with a constant calibration.

3.7.3   Transient simulation of the ACR

In Antarctica, a possible discrepancy exists during the ACR when the warming trend was interrupted between 14.8-14.2 and 12.9-12.6 ka depending on the ice-core record. Although the transient simulation only produces short-lived cooling at the onset of the ACR as a result of the mwp-1A contribution from Antarctic, there is a longer plateau in simulated Antarctic SAT driven by the resumption of NADW formation as well as the plateau of CO_2 levels (Fig. 1 J). This can be explicitly demonstrated in one sensitivity experiment (EXP-ACR hereafter) with the default transient forcing of insolation and greenhouse gas concentration, but without any meltwater discharge from either hemisphere during BA/ACR (fig. S6). The shutdown of NHMW at the

onset of the BA induces rapid resumption of the AMOC that causes warming over Greenland (fig. S6, A-C). Due to bipolar seesaw, the rapid resumption of the AMOC also initiates the cooling trend over the Antarctic (fig. S6 D). The cooling trend of Antarctic temperature lasts ~2,000 years during the ACR, presumably due to the long time scale associated with the adjustment of global thermohaline circulation. The small reduction of the atmospheric CO_2 at the latter half of ACR also helps to maintain the cooling trend. Both the AMOC and Antarctic temperature during ACR in EXP-ACR have better agreement with the proxy reconstructions; however, EXP-ACR fails to simulate the Older Dryas over Greenland.

In the transient simulation (Fig. 1 J), the abrupt warming of the Antarctic SAT at the end of ACR is associated with the lowering of the Antarctic ice sheet in the prescribed ICE-5G reconstruction [Peltier, 2004].

3.7.4   Data-model comparison of the South Pacific SST

We performed comprehensive data-model comparison for the SST record in the South Pacific (fig. S7), and found the model exhibits reasonable climate sensitivity in simulating the proxy record through the last deglaciation in Chilean margin, South Australian margin, offshore of New Zealand and the Indian sector of the Southern Ocean. Both the model and proxy data suggest that deglacial SST warming begins ~19-18 ka in the South Pacific and Southern Ocean.

3.7.5   Bipolar seesaw plays the dominant role in SH deglacial warming

In Fig. 2, we demonstrate that the last deglaciation originated in the NH due to its larger increase of high-latitude spring-summer insolation, likely initiating the retreat of NH ice sheets and the NHWM discharge 20-19 ka. Using a sensitivity experiment with only transient orbital

forcing (EXP-Orbit-19ka hereafter), we explicitly demonstrate that the NHMW discharge and associated bipolar seesaw [Crowley, 1992] plays a more important role than the local (SH) insolation in SH deglacial warming (fig. S8). EXP-Orbit-19ka is a 2,000-year simulation between 19 and 17ka with only transient orbital forcing. Since the CO_2 record used in this study adopted the EDC1 age model [Joos and Spahni, 2008], CO_2 does not vary significantly between 19 and 17ka in the transient simulation. Therefore the major difference between the transient simulation and EXP-Orbit-19ka is the NHMW discharge and the associated bipolar seesaw. It is readily to see that the NHMW discharge causes the SH mid-high latitude summer temperature to increase substantially at the onset of the SH deglaciation ~19ka with bipolar seesaw, which amounts to over 1 ^{o}C between 19 and 17 ka (red in fig. S8). With only the transient orbital forcing in EXP-Orbit-19ka, no significant warming is found in SH mid-high latitude between 19 and 17 ka. The comparison of the twin experiments with/without bipolar seesaw clearly shows the dominant role of bipolar seesaw in SH deglacial warming ~19ka. We note that the ~1 ^{o}C deglacial warming induced by the bipolar seesaw between 19 and 17 ka is also consistent with Antarctic temperature reconstruction (Fig. 1 J).

3.7.6 Mechanism of the Pacific bipolar-seesaw and deep ocean warming

In the transient simulation, the early deglacial warming of the surface Southern Ocean is induced by the bipolar seesaw associated with NHMW forcing [Crowley, 1992]. The zonal average of Atlantic SST shows the Greenland-like millennial variations in the North and Antarctic-like deglacial warming in the South (fig. S9). Notably the zonal-average of Pacific SST also exhibits the similar feature with Greenland-like millennial variations in the north and Antarctic-like warming trend in the south (fig. S10). The North Pacific millennial variations

were induced by the atmospheric teleconnections with cooling during H1 and YD and with warming during BA [Okumura et al., 2009]. As noted in Huang et al. [2000], a slowdown or shutoff of the NADW causes the cooling of North Atlantic, but tends to induce warming elsewhere via the deepening of the ocean thermocline. The signal is transmitted on decadal to centennial time scale from basin to basin through coastal and equatorial Kelvin waves, and is carried into interior of the ocean through Rossby waves. Therefore, the early warming in Southern and Deep Ocean is due to oceanic teleconnections via wave propagations from Atlantic into Pacific through Indian Ocean (fig. S11) [Knutti et al., 2004; Liu and Alexander, 2007].

3.7.7   Age uncertainty in CO_2 records

The CO_2 record used in this study adopted the EDC1 age model [Joos and Spahni, 2008] and the deglacial CO_2 rise started at ~17 ka. If GISP2 age model is adopted [Marchitto et al., 2007; Lemieux-Dudon et al., 2010], the CO_2 record during last deglaciation can be shifted by ~1,000 years earlier, which suggests deglacial CO_2 rise started at ~18 ka. In the transient simulation, the simulated deglacial warming in the Southern Ocean and Antarctic starts at 19 ka and leads the tropical warming by 2,000 years with the CO_2 forcing on the EDC1 age model, or by 1,000 years with a CO_2 forcing on the GISP2 age model. Therefore, our conclusion about the lead-lag relationship between SH and equatorial Pacific does not change if we adopt the GISP2 age model for the CO_2 record.

SOM references

Bard, E., B. Hamelin, and D. Delanghe-Sabatier (2010), Deglacial Meltwater Pulse 1B and Younger Dryas Sea Levels Revisited with Boreholes at Tahiti, Science, 327(5970), 1235-1237, doi: 10.1126/science.1180557.

Bassett, S. E., G. A. Milne, J. X. Mitrovica, and P. U. Clark (2005), Ice Sheet and Solid Earth Influences on Far-Field Sea-Level Histories, Science, 309(5736), 925-928, doi: 10.1126/science.1111575.

Berger, A. L. (1978), Long-Term Variations of Daily Insolation and Quaternary Climatic Changes, J.Atmos.Sci., 35(12), 2362-2367.

Calvo, E., C. Pelejero, P. De Deckker, and G. A. Logan (2007), Antarctic deglacial pattern in a 30 kyr record of sea surface temperature offshore South Australia, Geophys.Res.Lett., 34(13), L13707, doi: 10.1029/2007GL029937.

Carlson, A. E., P. U. Clark, B. A. Haley, G. P. Klinkhammer, K. Simmons, E. J. Brook, and K. J. Meissner (2007), Geochemical proxies of North American freshwater routing during the Younger Dryas cold event, Proceedings of the National Academy of Sciences, 104(16), 6556.

Carlson, A. E. (2008), Rapid early Holocene deglaciation of the Laurentide ice sheet, Nature Geosci., 1, 620-624.

Carlson, A. E. (2009), Geochemical constraints on the Laurentide Ice Sheet contribution to Meltwater Pulse 1A, Quaternary Science Reviews, 28(17-18), 1625-1630, doi: DOI: 10.1016/j.quascirev.2009.02.011.

Carlson, A. E., P. U. Clark, B. A. Haley, and G. P. Klinkhammer (2009), Routing of western Canadian Plains runoff during the 8.2 ka cold event, Geophys.Res.Lett., 36(14), L14704, doi: 10.1029/2009GL038778.

Clark, P. U., J. X. Mitrovica, G. A. Milne, and M. E. Tamisiea (2002), Sea-Level Fingerprinting as a Direct Test for the Source of Global Meltwater Pulse IA, Science, 295(5564), 2438-2441, doi: 10.1126/science.1068797.

Clark, P. U., A. S. Dyke, J. D. Shakun, A. E. Carlson, J. Clark, B. Wohlfarth, J. X. Mitrovica, S. W. Hostetler, and A. M. McCabe (2009), The Last Glacial Maximum, Science, 325(5941), 710-714, doi: 10.1126/science.1172873.

Clark, P. U., S. J. Marshall, G. K. C. Clarke, S. W. Hostetler, J. M. Licciardi, and J. T. Teller (2001), Freshwater Forcing of Abrupt Climate Change During the Last Glaciation, Science, 293(5528), 283-287, doi: 10.1126/science.1062517.

Clark, P. U., A. M. McCabe, A. C. Mix, and A. J. Weaver (2004), Rapid Rise of Sea Level 19,000 Years Ago and Its Global Implications, Science, 304(5674), 1141-1144, doi: 10.1126/science.1094449.

Collins, W. D., et al (2006), The Community Climate System Model Version 3 (CCSM3), J.Climate, 19(11), 2122-2143, doi: 10.1175/JCLI3761.1.

Crowley, T. J. (1992), North Atlantic deep water cools the southern hemisphere, Paleoceanography, 7, 489.

Dahl-Jensen, D., K. Mosegaard, N. Gundestrup, G. D. Clow, S. J. Johnsen, A. W. Hansen, and N. Balling (1998), Past Temperatures Directly from the Greenland Ice Sheet, Science, 282(5387), 268-271, doi: 10.1126/science.282.5387.268.

Huang, R. X., M. A. Cane, N. Naik, and P. Goodman (2000), Global adjustment of the thermocline in response to deepwater formation, Geophys.Res.Lett., 27(6), 759-762, doi: 10.1029/1999GL002365.

Huybers, P. (2006), Early Pleistocene Glacial Cycles and the Integrated Summer Insolation Forcing, Science, 313(5786), 508-511, doi: 10.1126/science.1125249.

Huybers, P., and G. Denton (2008), Antarctic temperature at orbital timescales controlled by local summer duration, Nature Geosci, 1(11), 787-792.

Joos, F., and R. Spahni (2008), Rates of change in natural and anthropogenic radiative forcing over the past 20,000 years, Proceedings of the National Academy of Sciences, 105(5), 1425-1430, doi: 10.1073/pnas.0707386105.

Kaiser, J., F. Lamy, and D. Hebbeln (2005), A 70-kyr sea surface temperature record off southern Chile (Ocean Drilling Program Site 1233), Paleoceanography, 20(4), PA4009, doi: 10.1029/2005PA001146.

Knutti, R., J. Fluckiger, T. F. Stocker, and A. Timmermann (2004), Strong hemispheric coupling of glacial climate through freshwater discharge and ocean circulation, Nature, 430(7002), 851-856.

LeGrande, A. N., and G. A. Schmidt (2009), Sources of Holocene variability of oxygen isotopes in paleoclimate archives, Clim.Past, 5(3), 441-455, doi: 10.5194/cp-5-441-2009.

Lemieux-Dudon, B., E. Blayo, J. Petit, C. Waelbroeck, A. Svensson, C. Ritz, J. Barnola, B. M. Narcisi, and F. Parrenin (2010), Consistent dating for Antarctic and Greenland ice cores, Quaternary Science Reviews, 29(1-2), 8-20, doi: DOI: 10.1016/j.quascirev.2009.11.010.

Licciardi, J. M., J. T. Teller, and P. U. Clark (1999), Freshwater routing by the Laurentide Ice Sheet during the last deglaciation, in   Mechanisms of Global Climate Change

at Millennial Time Scalesedited by P. U. Clark, R. S. Webb and L. D. Keigwin, pp. 177–201, American Geophysical Union, Washington, DC, .

Liu, Z., et al (2009), Transient Simulation of Last Deglaciation with a New Mechanism for Bølling-Allerød Warming, Science, 325(5938), 310-314, doi: 10.1126/science.1171041.

Liu, Z., and M. Alexander (2007), Atmospheric bridge, oceanic tunnel, and global climatic teleconnections, Rev.Geophys., 45(2), RG2005, doi: 10.1029/2005RG000172.

Marchitto, T. M., S. J. Lehman, J. D. Ortiz, J. Fluckiger, and A. van Geen (2007), Marine Radiocarbon Evidence for the Mechanism of Deglacial Atmospheric CO_2 Rise, Science, , 1138679.

McManus, J. F., R. Francois, J. M. Gherardi, L. D. Keigwin, and S. Brown-Leger (2004), Collapse and rapid resumption of Atlantic meridional circulation linked to deglacial climate changes, Nature, 428(6985), 834-837.

Obbink, E. A., A. E. Carlson, and G. P. Klinkhammer (2010), Eastern North American freshwater discharge during the Bølling-Allerød warm periods, Geology, 38(2), 171-174, doi: 10.1130/G30389.1.

Okumura, Y. M., C. Deser, A. Hu, A. Timmermann, and S. Xie (2009), North Pacific Climate Response to Freshwater Forcing in the Subarctic North Atlantic: Oceanic and Atmospheric Pathways, J.Clim., 22(6), 1424-1445.

Otto-Bliesner, B. L., E. C. Brady, G. Clauzet, R. Tomas, S. Levis, and Z. Kothavala (2006), Last Glacial Maximum and Holocene Climate in CCSM3, J.Clim., 19(11), 2526-2544.

Otto-Bliesner, B., C. D. Hewitt, T. M. Marchitto, E. Brady, A. Abe-Ouchi, M. Crucifix, S. Murakami, and S. L. Weber (2007), Last Glacial Maximum ocean thermohaline circulation: PMIP2 model intercomparisons and data constraints, Geophys.Res.Lett., 34(12), L12706, doi: 10.1029/2007GL029475.

Pahnke, K., and J. P. Sachs (2006), Sea surface temperatures of southern midlatitudes 0–160 kyr B.P, Paleoceanography, 21(2), PA2003, doi: 10.1029/2005PA001191.

Peltier, W. R. (2004), Global glacial isostasy and the surface of the ice-age Earth- The ICE-5 G(VM 2) model and GRACE, Annu.Rev.Earth Planet.Sci., 32(1), 111-149.

Peltier, W. R., and R. G. Fairbanks (2006), Global glacial ice volume and Last Glacial Maximum duration from an extended Barbados sea level record, Quaternary Science Reviews, 25(23-24), 3322-3337.

Praetorius, S. K., J. F. McManus, D. W. Oppo, and W. B. Curry (2008), Episodic reductions in bottom-water currents since the last ice age, Nature Geosci, 1(7), 449-452.

Rickaby, R. E. M., and H. Elderfield (1999), Planktonic Foraminiferal Cd/Ca: Paleonutrients or Paleotemperature? Paleoceanography, 14(3), 293-303, doi: 10.1029/1999PA900007.

Stanford, J. D., E. J. Rohling, S. E. Hunter, A. P. Roberts, S. O. Rasmussen, E. Bard, J. McManus, and R. G. Fairbanks (2006), Timing of meltwater pulse 1a and climate responses to meltwater injections, Paleoceanography, 21(4), PA4103.

Yeager, S. G., C. A. Shields, W. G. Large, and J. J. Hack (2006), The Low-Resolution CCSM3, J.Clim., 19(11), 2545-2566.

Yokoyama, Y., K. Lambeck, P. De Deckker, P. Johnston, and L. K. Fifield (2000), Timing of the Last Glacial Maximum from observed sea-level minima, Nature, 406(6797), 713-716.

SOM table

Location of the meltwater forcing in the transient simulation

Location	Longitude	Latitude
North Atlantic	$80^oW \sim 20^oE$	$50^oN \sim 70^oN$
Mackenzie river	$210^oE \sim 240^oE$	$65^oN \sim 75^oN$
Nordic Sea	$15^oW \sim 30^oE$	$55^oN \sim 75^oN$
St. Lawrence River	$270^oE \sim 310^oE$	$38^oN \sim 60^oN$
Gulf of Mexico	$255^oE \sim 280^oE$	$15^oN \sim 33^oN$
Ross Sea	$140^oE \sim 220^oE$	$60^oS \sim 80^oS$
Weddell Sea	$70^oW \sim 30^oE$	$60^oS \sim 80^oS$
Hudson Strait	$280^oE \sim 312^oE$	$55^oN \sim 70^oN$
Arctic	$200^oE \sim 275^oE$	$70^oN \sim 76^oN$
Barents Sea	$25^oE \sim 55^oE$	$65^oN \sim 80^oN$
North Sea	$0^oE \sim 12^oE$	$45^oN \sim 62^oN$

SOM figures

Figure S1: Meltwater forcing in the transient simulation in m/kyr (meters of global sea level rise in 1,000 years). (**A**) Total meltwater forcing from northern hemisphere, which includes the meltwater discharge into (**B**) North Atlantic between 50° N and 70° N, (**C**) St. Lawrence River, (**D**) Gulf of Mexico, (**E**) Mackenzie River, (**F**) North Sea, (**G**) Hudson Strait, (**H**) Barents Sea, (**I**) Arctic and (**J**) Nordic Sea. (**K**) Total meltwater forcing from southern hemisphere, which includes the meltwater discharge into (**L**) Weddell Sea and (**M**) Ross Sea. Refer SOM table 1 and fig. S2 for the exact location of meltwater discharge.
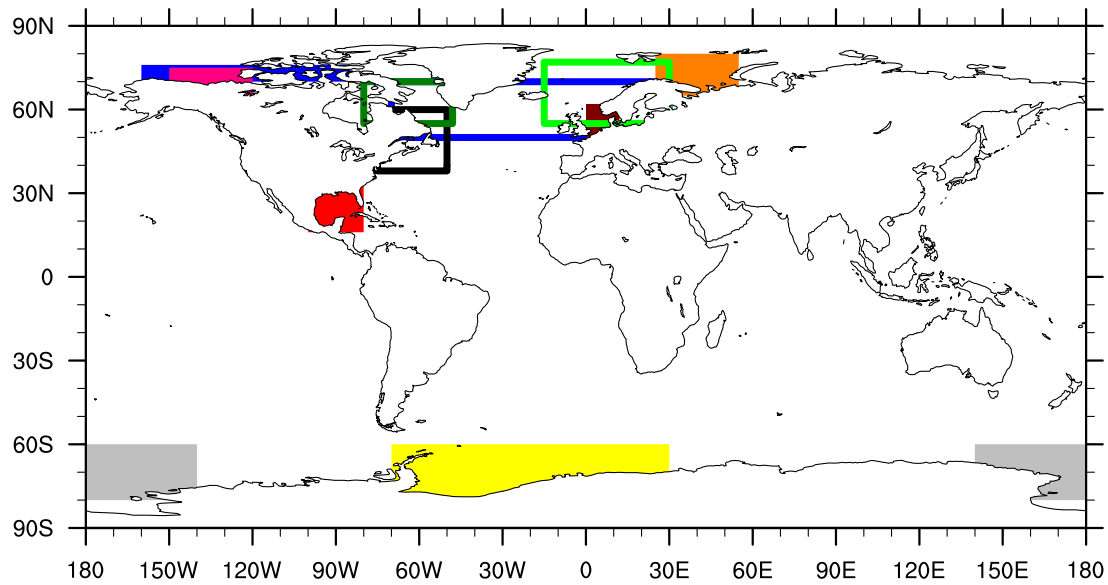
Figure S2: Location of meltwater discharge in the transient simulation: Arctic (blue shading), Mackenzie River (pink shading), Barents Sea (orange shading), Gulf of Mexico (red shading), North Sea (dark red shading), Nordic Sea (hollow green), North Atlantic between 50° N and 70° N (hollow blue), Hudson Strait (hollow dark green), St. Lawrence River (hollow black), Weddell Sea (yellow shading) and Ross Sea (gray shading).
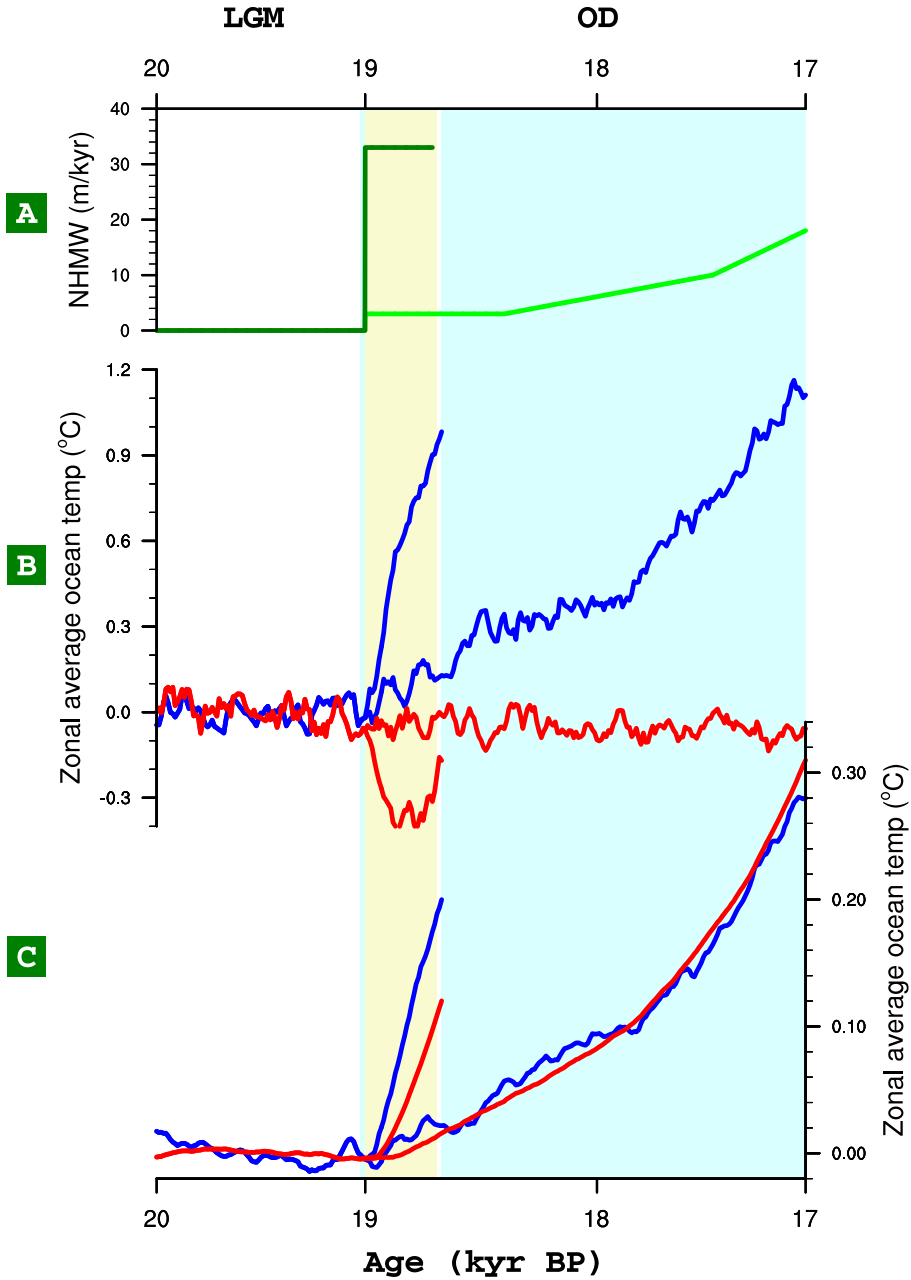
Figure S3: Response of the Southern Ocean and equatorial Pacific to the NHMW. (**A**) NHMW fluxes in transient simulation (light blue shading) and sensitivity experiment TraCE-19ka (light yellow shading). (**B**) Changes of zonal average SSTs in the Southern Ocean (45°S, blue) and equatorial Pacific (red) in the transient simulation (light blue shading) and TraCE-19ka (light yellow shading). All model variables are anomalies in 10-year averages with reference to the average value between 20 and 19ka. (**C**) Same as (**B**), but for deep ocean temperatures at 2300 m.
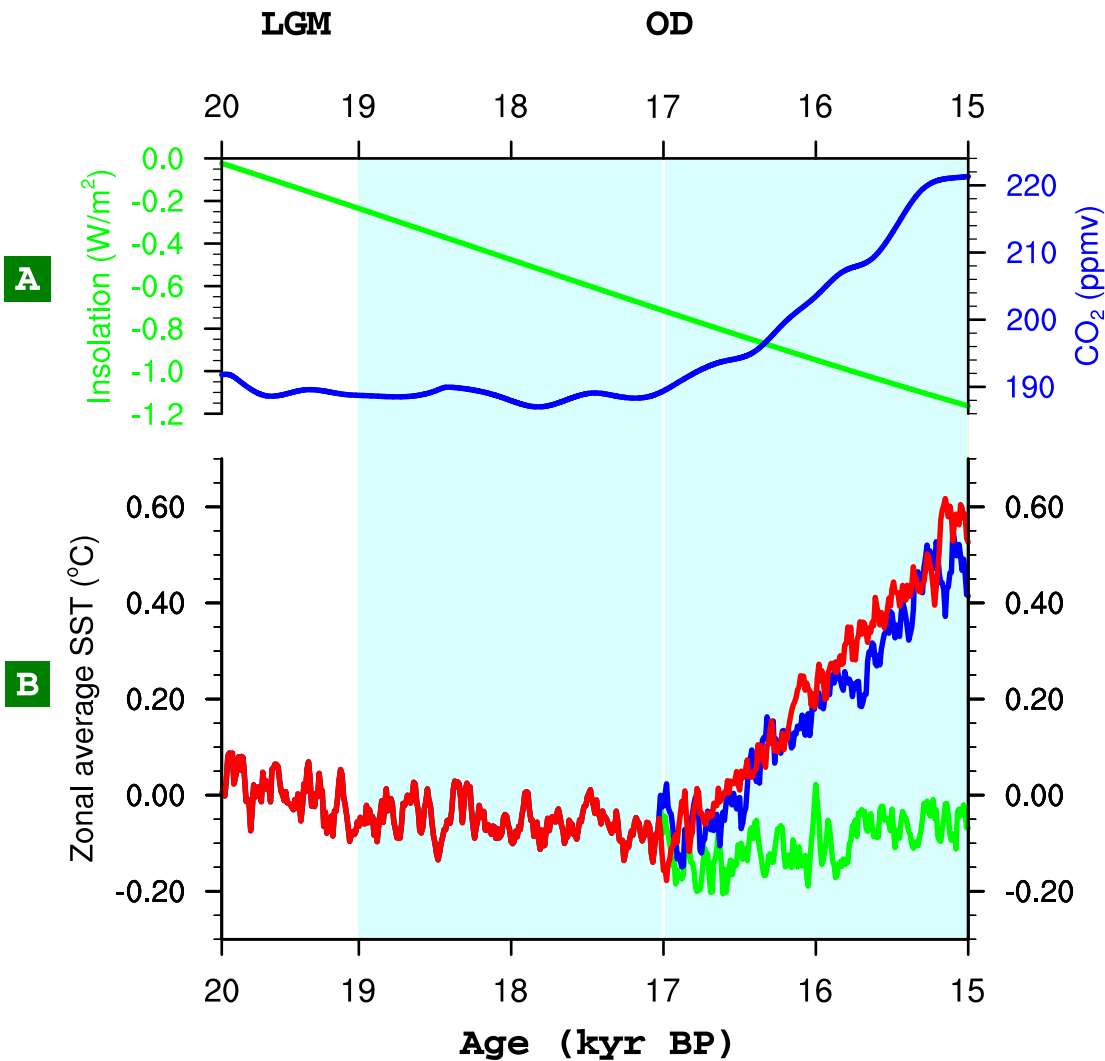
Figure S4: Attribution of deglacial warming of the equatorial Pacific to deglacial CO_2 rise. (**A**) Atmospheric CO_2 concentration (blue) [Joos and Spahni, 2008] and changes of annual average insolation at equator (green) [Berger, 1978]. (**B**) Changes of Zonal average SSTs of equatorial Pacific in transient simulation TraCE-21K (red) and twin sensitivity experiments TraCE-Orbit (green) and TraCE-CO_2 (blue). All model variables are anomalies in 10 year averages with reference to the average value between 20 and 19ka. Since TraCE-CO_2 produces the majority warming of equatorial Pacific in TraCE-21K between 17-15ka, the deglacial warming of equatorial Pacific in TraCE-21K is mostly caused by the transient CO_2 forcing.
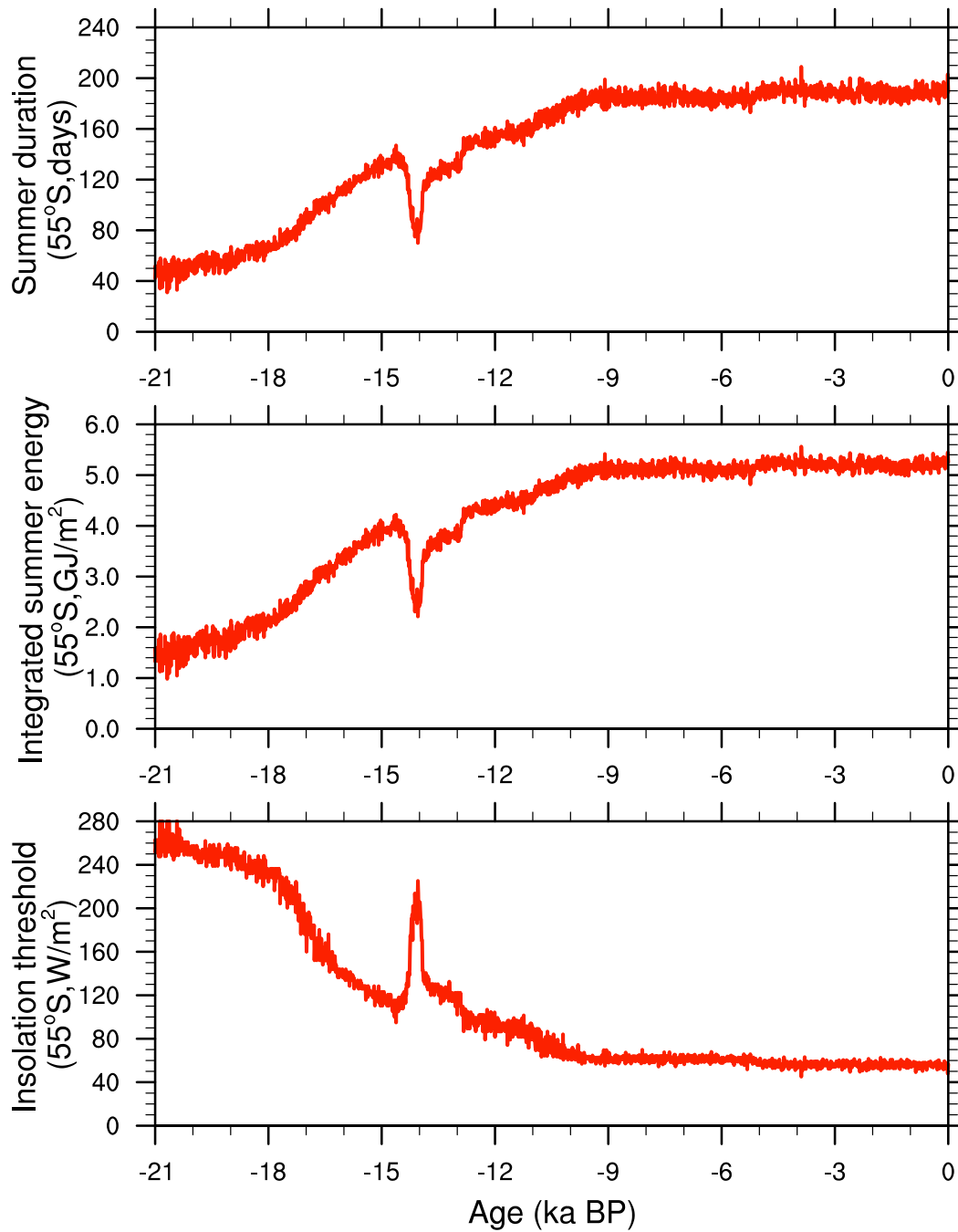
Figure S5: The evolution of the insolation threshold for the summer durations in the transient simulation. (**A**) Summer duration at 55ºS. (**B**) Integrated summer energy at 55ºS. (**C**) Insolation threshold for 55ºS at the end of the summer.
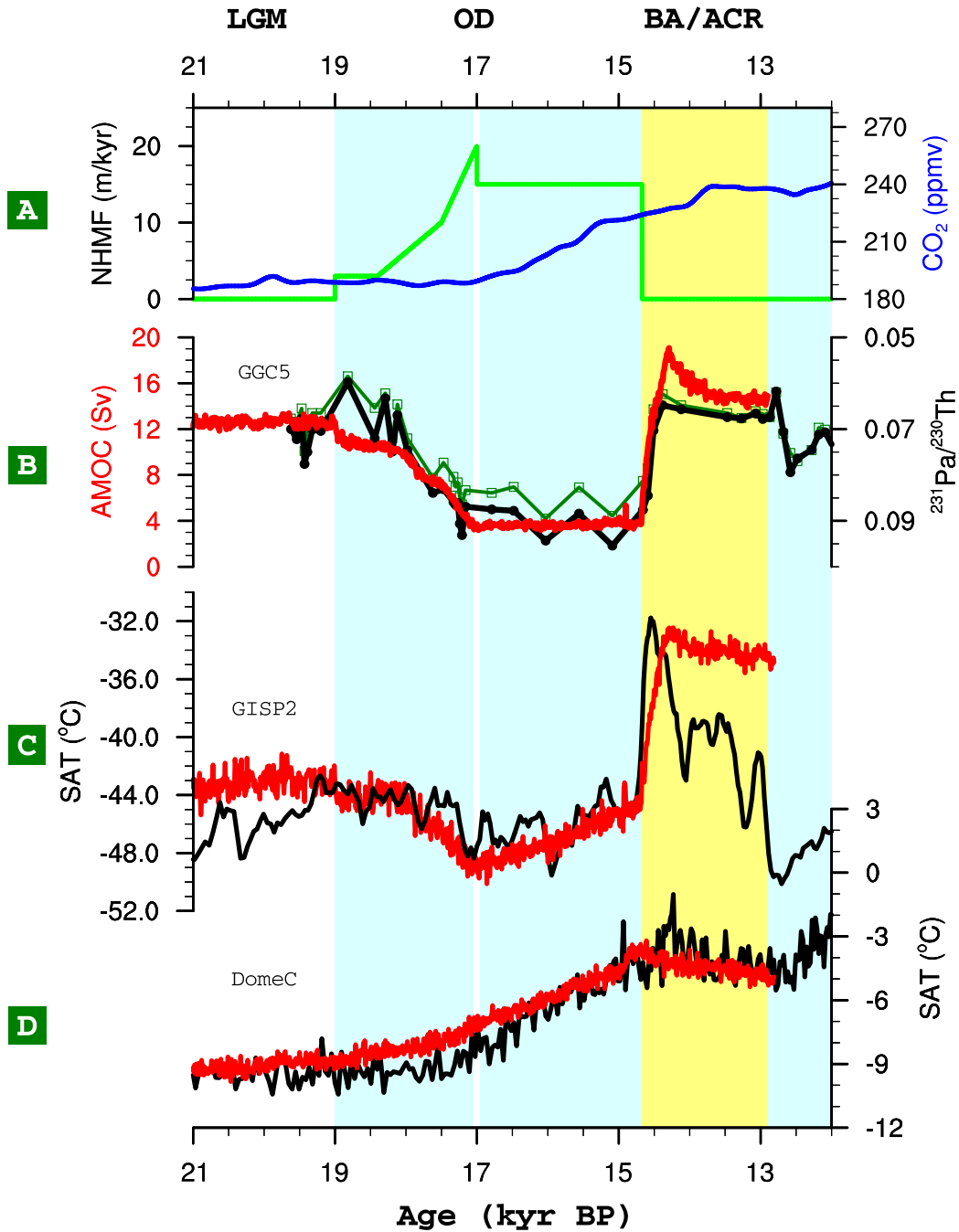
Figure S6: The transient simulation of the ACR in EXP-ACR. (**A**) Atmospheric CO_2 concentration (blue) [Joos and Spahni, 2008] and NHMW (green) in the sensitivity experiment. (**B**) AMOC in the sensitivity experiment (red), superimposed by AMOC reconstructions (black and green) [McManus et al., 2004]. (**C**) Greenland SAT based on GISP2 $\delta^{18}O$ reconstruction with borehole temperature calibration (black) and in the sensitivity experiment (red, model offset by $-4.5°C$). (**D**) Antarctic SAT from Dome C δD reconstruction (black) and model (red).
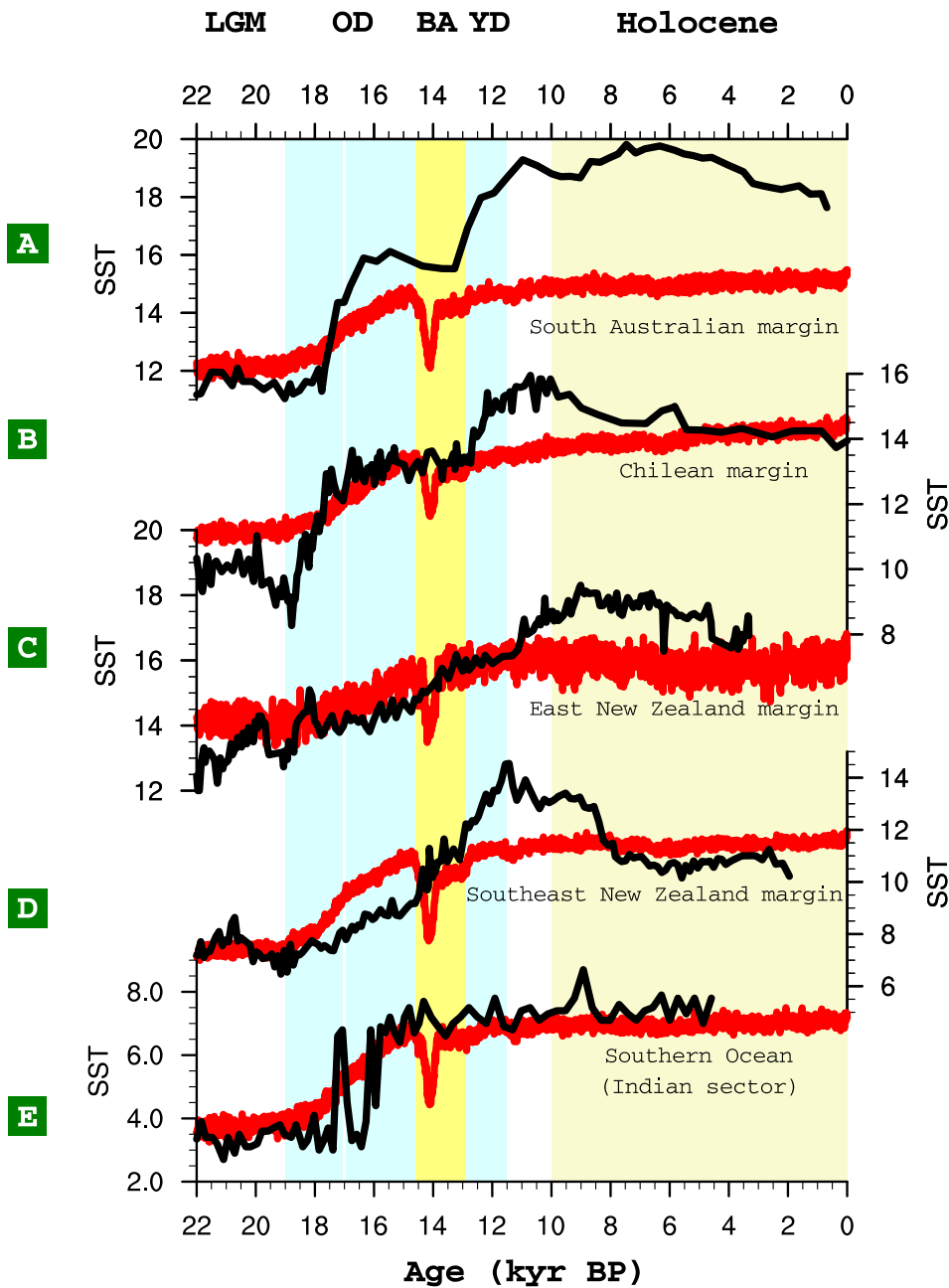
Figure S7: Data-model comparison for SST in South Pacific. (**A**) SST from South Australian margin [Calvo et al., 2007] and model (offset by 3°C). (**B**) SST from Chilean margin [Kaiser et al., 2005] and model (offset by 3°C). (**C**) SST from East New Zealand margin [Pahnke and Sachs, 2006] and model (offset by 1°C). (**D**) SST from Southeast New Zealand margin [Pahnke and Sachs, 2006] and model (offset by 3.5°C). (**E**) SST from Indian sector of the Southern Ocean [Rickaby and Elderfield, 1999] and model (offset by 0.7°C). Overall, model simulations are in good agreement with the proxy records.
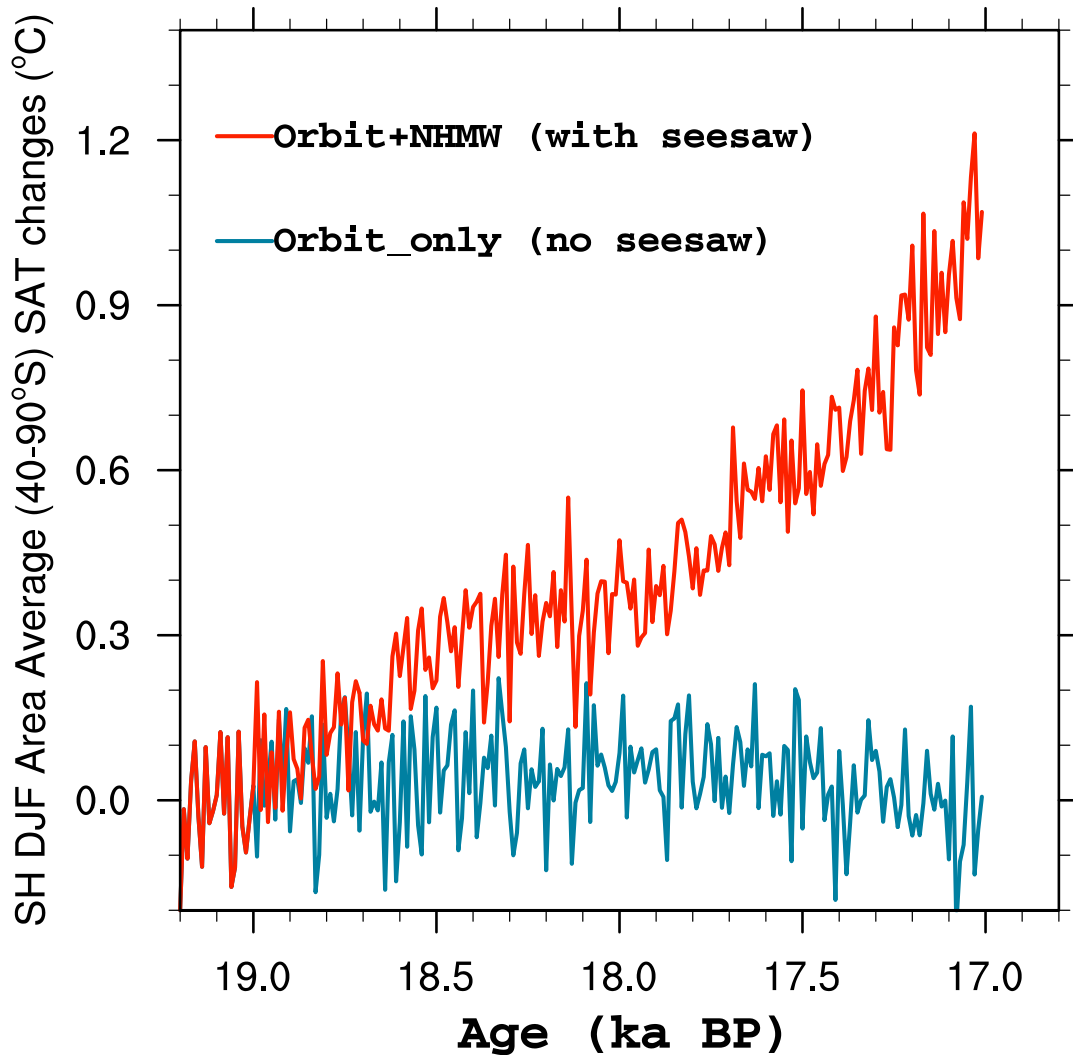
Figure S8: The dominant role of bipolar seesaw at the onset of SH deglacial warming. The transient simulation with bipolar seesaw (all forcing) is shown in red, and the transient simulation without bipolar seesaw (orbit-only forcing) is shown in blue. It is readily to see that the NHMW discharge causes the SH mid-high latitude summer temperature to increase substantially at the onset of the SH deglaciation ~19ka with bipolar seesaw. All data are plotted in 10 year running averages.
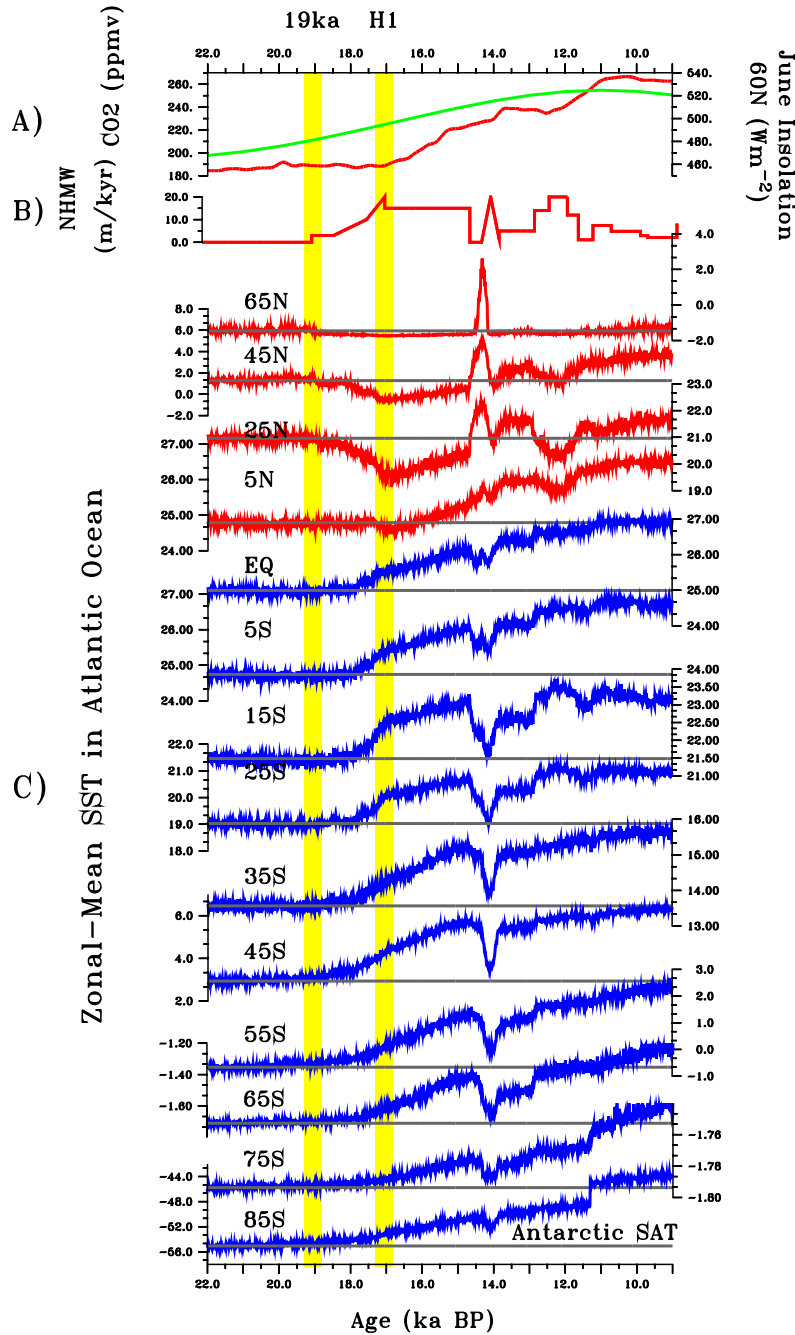
Figure S9: Simulated zonal-average SST at various latitudes in Atlantic Ocean during last deglaciation. (**A**) June 21st insolation at 60°N (green) [Berger, 1978] and atmospheric CO_2 concentration (red) [Joos and Spahni, 2008]. (**B**) NHMW fluxes in the model. (**C**) Simulated zonal-average SSTs at various latitudes in the North Atlantic Ocean (red), South Atlantic and Southern Ocean (blue). The zonal-average of Antarctic SAT at 85°S is also plotted in blue. The bipolar seesaw can be identified between 19 and H1 (~17ka) when the cooling occurs in the North Atlantic Ocean and the warming occurs in the south.
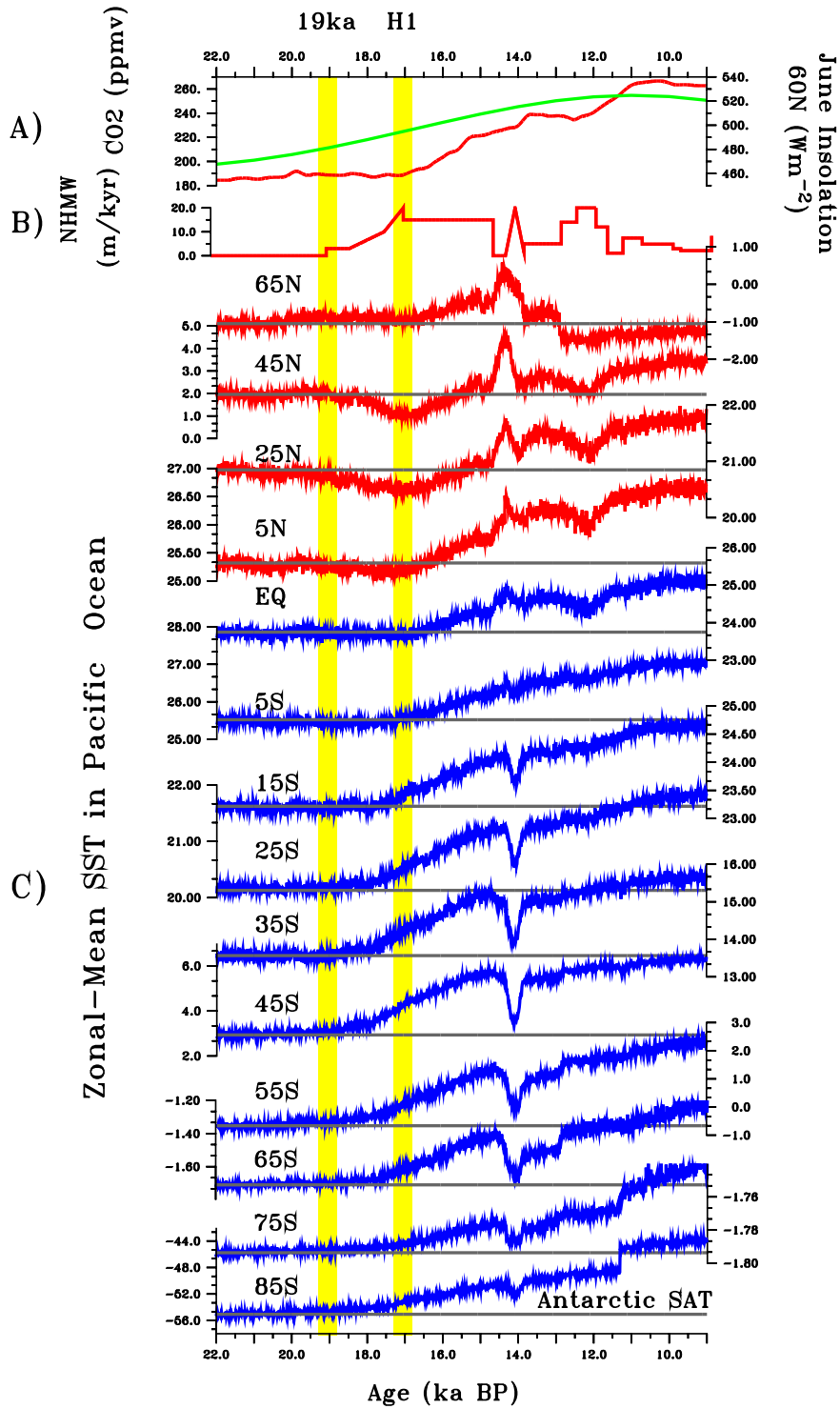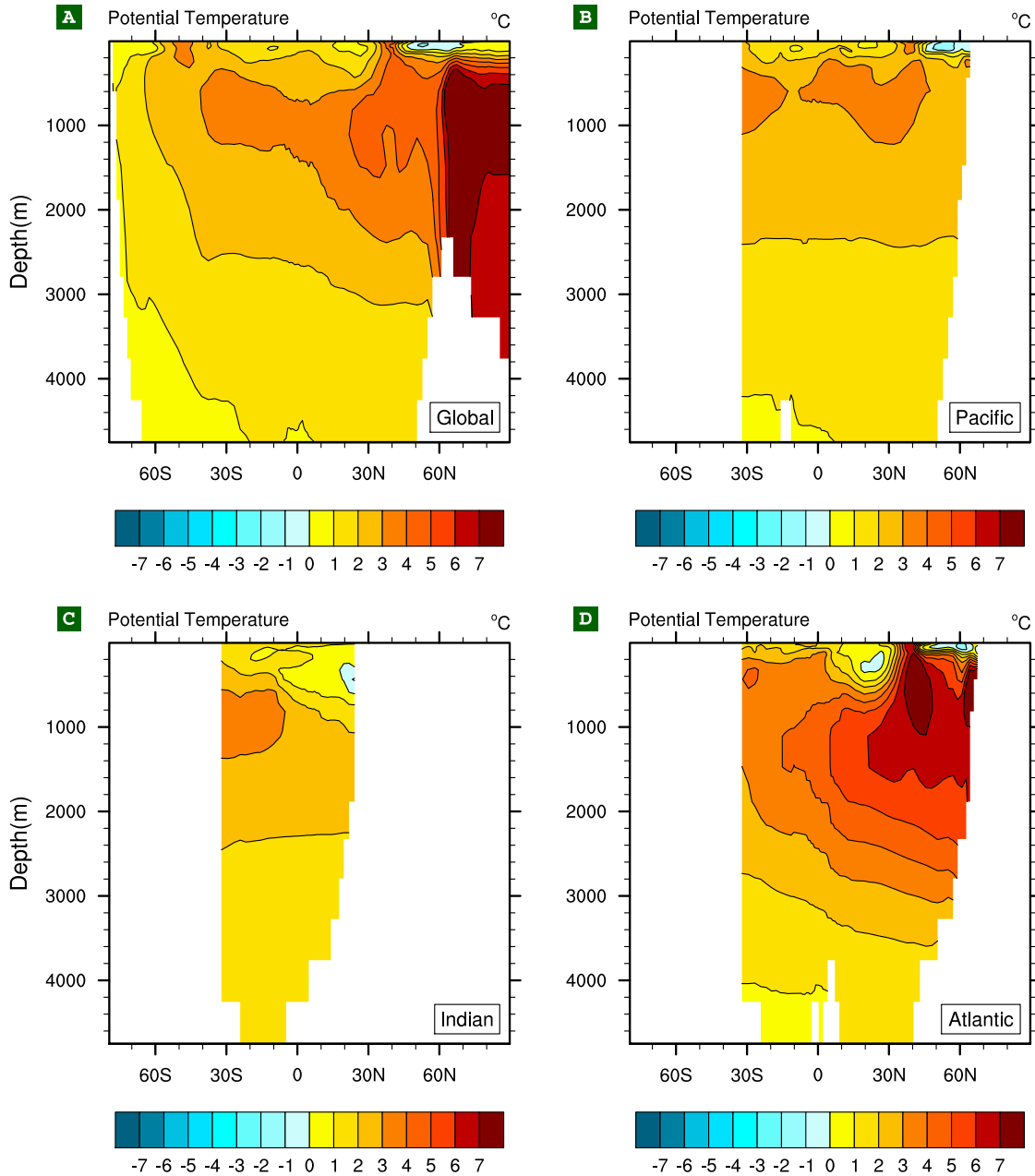
Figure S10: Same as fig. S9, but for Pacific Ocean. Again, the "Pacific bipolar seesaw" can be identified between 19 and H1 (~17ka) when the cooling occurs in the North Pacific Ocean and the warming occurs in the south.

Figure S11: Simulated zonal-average warming of the world oceans during last deglaciation (21~10ka): (**A**) Global Ocean. (**B**) Pacific Ocean. (**C**) Indian Ocean (**D**) Atlantic Ocean. The warming in Arctic Ocean can be seen in the NH polar region in (**A**).
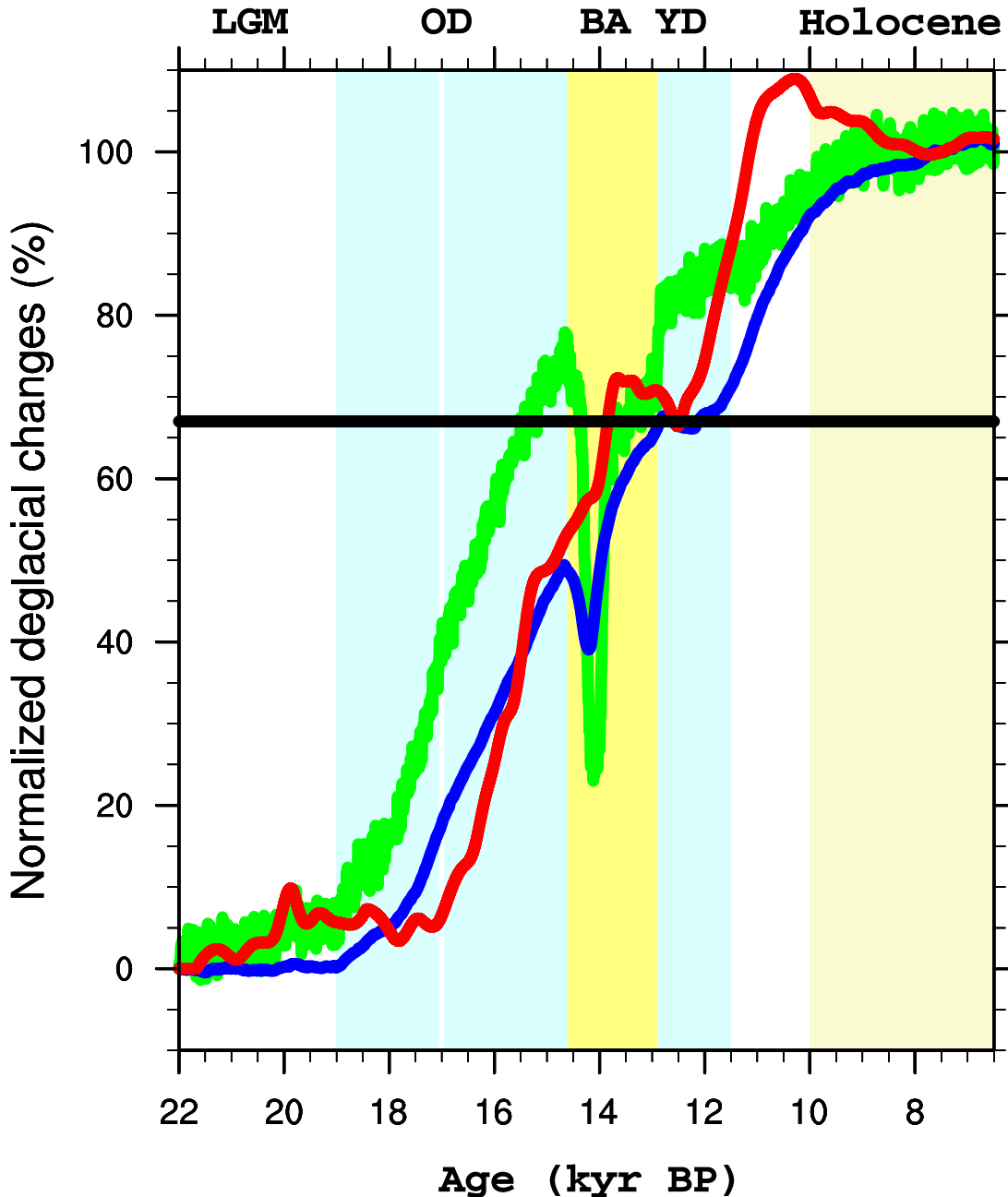
Figure S12: Two-stage deglacial changes in transient simulation and proxy data. The vertically average global ocean temperature (blue) and SH sea ice (green) are from transient simulation, and the atmospheric CO_2 concentration (red) are from the Dome C ice core [Joos and Spahni, 2008]. All the time series are normalized by their total deglacial changes from 22 to 7.5 ka, respectively. The black line delineates the level of two thirds (66.7%). It is notable that both the ocean temperature increase and SH sea ice retreat occur in two stages in the transient simulation, with two thirds of the deglacial changes occurring approximately before BA/ACR and another one third occurring between YD and Holocene. A similar two-stage change also occurred in deglacial atmospheric CO_2 rise.

Chapter 4   Abrupt Climate Change Triggered by Norwegian Sea Convections

4.1   Introduction

In the IPCC AR4 report the warming at the end of 21st century is projected as between two and four degree Celsius, depending on the different scenarios of future carbon emissions [Solomon et al., 2007]. However, this statement is based on the equilibrium sensitivity, and the climate system is likely to exhibit unexpected climate changes through the transient and nonlinear dynamics, especially in the polar region. During the last deglaciation (21,000 to 10,000 years ago), several millennial climatic events with temperature shifts of 10 ^{o}C or more punctuated the overall warming trend as recorded in both the Greenland ice core and ocean sediments in the North Atlantic Ocean [Cuffey and Clow, 1997; Waelbroeck et al., 1998; Bard et al., 2000]. The close relationship between the proxy data from the ice cores and the ocean sediment has been suggested to be caused by the variability of the Atlantic meridional overturning circulation (AMOC) [Broecker, 1985; Rahmstorf, 1995]. Recent reconstruction of AMOC via Pa/Th provides further evidence that the variability of AMOC plays a critical role in modulating the millennial climate events during the last deglaciation [McManus et al., 2004]. Furthermore, regional abrupt climate changes are more likely to occur on even shorter time scale. For example, Lehman and Keigwin [1992] (LK92 thereafter) documented abrupt warming of Sea Surface Temperature (SST) and Surface Air Temperature (SAT) in less than 40 years in the Norwegian Sea during the last deglaciation, and they suspected that the abrupt warming was caused by the sudden deep water formation in the Norwegian Sea, which drew the Atlantic water into the Norwegian basin for the first time during the last deglaciation.

As stated in Alley et al. [2002], an abrupt climate change occurs when the climate system is forced to transition to a new state at a rate that is determined by the climate system itself, and which is more rapid than the rate of change of the external forcing. This statement emphasizes the importance of the nonlinearity and the transient climate response in the abrupt climate change: the abrupt climate changes develop more rapidly than the external forcing. In order to provide more accurate projection in the future, we need to demonstrate that the IPCC-type global climate models (GCMs) not only have the correct climate sensitivity to greenhouse gases, but also have the capability of simulating abrupt climate changes in the past. For this reason, the reasonable simulation of the abrupt climate change event in LK92 becomes one of the prerequisites for the current and future generation of GCMs to make faithful climate projections.

4.2   Model setup and boundary condition

Using low resolution of the NCAR-CCSM3 [Yeager et al., 2006], we have completed the first synchronously coupled atmosphere-ocean general circulation model simulation of the transient evolution of global climate of the last 21,000 years (TraCE-21K). Our simulation reproduces the timing, structure and amplitude of the major deglacial climate changes reconstructed from proxy records in Greenland, Antarctica, the tropical Pacific Ocean, the Southern Ocean, and the deep Pacific Ocean, suggesting that our model exhibits reasonable climate sensitivity in those regions. Since the first inflow of the Atlantic water to the Norwegian Sea occurred between Heinrich event 1 (H1) ~17 ka and Bølling-Allerød (BA) warming ~14.5 ka [Slubowska et al., 2005], we performed the 2,800-year transient simulation from 17.0 to 14.2 ka (TraCE-Abrupt thereafter) to test the capability of NCAR-CCSM3 in simulating the abrupt warming of the Norwegian Sea under slow changes of external forcing.

In TraCE-21K, the H1 cooling is caused by the collapse of the AMOC with 15 m kyr^{-1} North Hemisphere meltwater (NHMW) discharge into the 50-70° N of North Atlantic Ocean and 5 m kyr^{-1} NHMW discharge into Gulf of Mexico [Liu et al., 2009]. Starting from H1, TraCE-Abrupt was forced by smooth changes in insolation [Berger, 1978] and atmospheric greenhouse gas concentrations [Joos and Spahni, 2008] (Fig. 1 A). In order to ensure slow changes of external forcing for TraCE-Abrupt, we linearly decreased NHMW from 20 m kyr^{1} to 0 in 2,800 years from 17.0 to 14.2 ka (Fig. 1 B and C). We also kept the continental ice-sheet orography and extent at its H1 condition.

4.3   Abrupt onset of the Norwegian Sea warming

In TraCE-Abrupt, even though the reduction of NHMW is linear (Fig. 1 C), the response of AMOC to the ramped forcing exhibits nonlinearity (Fig. 1 D and Fig. 2). AMOC starts to increase slowly to 6 Sv (1 Sv = 10^6 m^3 s^{-1}) as NHMW drops from 20 to 10 m kyr^{-1}, then AMOC increases more rapidly to 10 Sv as NHMW drops from 10 to 6 m kyr^{-1}. When NHMW drops from 6 to 3.0 m kyr^{-1}, AMOC increases slowly from 10 to 11.5 Sv. Just before NHMW zeroes out, there is a rapid 5.5 Sv increase of AMOC from 11.5 Sv to 17 Sv when NHMW drops from 3 m kyr^{-1} to 0. The modeled GISP2 temperature closely follows the change of AMOC and exhibits a similar nonlinear variability under the linear reduction of NHMW (Fig. 1 E and Fig. 3). There is also a rapid 4.5 ^{o}C increase of SAT over Summit Greenland when NHMW drops from 3 m/kyr to 0. Even though TraCE-Abrupt fails to simulate the abrupt resumption of Greenland SAT as reconstructed from oxygen isotopes in Greenland ice cores, the modeled Summit Greenland temperature increases by 16 ^{o}C from -45 to -29 ^{o}C from the H1 to the onset of the BA (Fig. 3),

exhibiting excellent agreement with the amplitude of the SAT increase from the ice core reconstructions [Cuffey and Clow, 1997].

Associated with the rapid resumption of AMOC in TraCE-Abrupt ~14.5ka, the SAT in the Norwegian Sea shoots up from -10 ^{o}C to above freezing in just four decades (Fig. 1 F). The extent of the ~10 ^{o}C abrupt warming is mostly confined in the Norwegian Sea, and up to 3 ^{o}C warming also occurs in Greenland and Northwest Europe (Fig. 4 A). The SST in the Norwegian Sea also exhibits abrupt 3 ^{o}C increase from near -1 ^{o}C to 2 ^{o}C in ~40 years (Fig. 1 G). This is the first time in TraCE-Abrupt that the Norwegian Sea has experienced above zero surface temperature since the LGM and it marks the onset of the deglaciation in this region.

The abrupt warming in the Norwegian Sea is indeed associated with the deep water formation and the Atlantic inflow, as was suggested by LK92. The maximum mix layer depth, an indicator of the deep water formation, remains around 50 m for 7500 years since 22ka before abruptly deepens by more than 350 m in the Norwegian Sea in ~40 years ~14.5ka (Fig. 1 J and Fig. 4 C). The deep water formation induces anticlockwise circulation in the Nordic Sea basin (Fig. 4 D) and draws the North Atlantic water into the Norwegian basin, with the speed of Norwegian current almost tripled within ~40 years (Fig. 1 H). With the inflow of the warmer and saltier Atlantic water, the sea ice concentration in Norwegian basin abruptly reduces from 60% to 10% in ~40 years (Fig. 1 I and Fig. 4 B). After the sea ice opens, massive heat fluxes (Fig. 5 A) with maximum value above 100 W m^{-2} are transferred from the ocean into the atmosphere, resulting in the abrupt SAT increase. These heat fluxes are mainly from the sensible and latent heat fluxes (Fig. 5 B-D) as a result of the sudden opening of the sea ice in the Norwegian Sea.

The upward heat fluxes exclude any scenarios that the atmosphere dynamics accounts for the abrupt climate change.

4.4   Norwegian Sea stability as the threshold for the regional abrupt climate change

The spontaneous abrupt change with the slow changes of external forcing is often explained with the scenario that the system exceeds certain threshold [Lenton et al., 2008]. Therefore, the search for the specific threshold and the investigation of the associated physical mechanism are crucial for the potential projections of abrupt climate changes. It was hypothesized in LK92 and also clearly demonstrated in the transient simulation that the deep water formation in the Norwegian Sea is one of the crucial physical processes for the ~40-year abrupt warming in the Norwegian Sea. However, it is still unclear what triggers the convections in the Norwegian Sea, what sets the threshold for this event and whether this abrupt climate change event can be projected several years in advance.

The ocean convections can often be induced by the relatively unstable vertical density profiles, where the density of the water in the upper layer is larger than that below it. In TraCE-Abrupt, with the linear reduction of NHMW discharge in Gulf of Mexico and 50-70° N of North Atlantic, the Norwegian Sea density starts to recover (Fig. 6). In addition, the density recovery is much faster on the upper layers than the lower layers because the fresh meltwater has the tendency to spread in the upper layer of the ocean. As a result, the stability in the Norwegian Sea becomes progressively weaker in TraCE-Abrupt and becomes marginally unstable at ~14.5ka between 250 and 700 m (Fig. 1 K and Fig. 6), 300 years before the NHMW zeros out. The marginally unstable density profile quickly initiates the convections and induces the ~10 ^{o}C abrupt warming event in the Norwegian Sea. In summary, our transient simulation suggests that

the abrupt Norwegian Sea warming event documented in LK92 can be triggered by the density instability in the subsurface ocean (Fig. 1 J and K). Because the stability of the Norwegian Sea is reduced relatively linearly under the slow change of the external forcing, the long term observations of the density structure in this region can give a reasonable projection several years before it becomes relatively unstable and sets off to initiate the ocean convections.

4.5   Conclusion

Our 2,800-year transient simulation with smooth changes of external forcing reproduces the 40-year Norwegian Sea abrupt warming event documented by LK92, suggesting that CCSM3 is capable of simulating abrupt climate changes. This abrupt warming is triggered by the sudden switch–on of the Norwegian Sea deep water formation that results in strong inflow of North Atlantic water and rapid opening of the sea ice in the Norwegian basin. The timing of the abrupt warming can be estimated by projecting when the subsurface water density profile reaches the threshold of the marginal instability. Our study suggests that long term observations of density profiles in the Arctic and West Antarctic are vital for projections of the potential abrupt climate events in the future.

References

Alley, R. B., J. Marotzke, W. Nordhaus, J. Overpeck, D. Peteet, R. Pielke Jr, R. Pierrehumbert, P. Rhines, T. Stocker, and L. Talley (2002), Abrupt climate change: Inevitable surprises, 244 pp., National Academy Press, Washington, D.C.

Bard, E., F. Rostek, J. L. Turon, and S. Gendreau (2000), Hydrological Impact of Heinrich Events in the Subtropical Northeast Atlantic, Science, 289(5483), 1321-1324.

Berger, A. L. (1978), Long-Term Variations of Daily Insolation and Quaternary Climatic Changes, J.Atmos.Sci., 35(12), 2362-2367.

Broecker, W. S., D. M. Peteet, and D. Rind (1985), Does the ocean-atmosphere system have more than one stable mode of operation? Nature, 315(6014), 21-26.

Cuffey, K. M., and G. D. Clow (1997), Temperature, accumulation, and ice sheet elevation in central Greenland through the last deglacial transition, Journal of Geophysical Research, 102(C12), 26383-26396.

Joos, F., and R. Spahni (2008), Rates of change in natural and anthropogenic radiative forcing over the past 20,000 years, Proceedings of the National Academy of Sciences, 105(5), 1425-1430, doi: 10.1073/pnas.0707386105.

Lehman, S. J. and L.D. Keigwin (1992). Sudden changes in the North Atlantic circulation during the last deglaciation. Nature 356: 757-762.

Lenton, T. M., H. Held, E. Kriegler, J. W. Hall, W. Lucht, S. Rahmstorf, and H. J. Schellnhuber (2008), Tipping elements in the Earth's climate system, Proceedings of the National Academy of Sciences, 105(6), 1786-1793, doi: 10.1073/pnas.0705414105.

Liu, Z., et al (2009), Transient Simulation of Last Deglaciation with a New Mechanism for Bølling-Allerød Warming, Science, 325(5938), 310-314, doi: 10.1126/science.1171041.

McManus, J. F., R. Francois, J. M. Gherardi, L. D. Keigwin, and S. Brown-Leger (2004), Collapse and rapid resumption of Atlantic meridional circulation linked to deglacial climate changes, Nature, 428(6985), 834-837.

Rahmstorf, S. (1995), Bifurcations of the Atlantic thermohaline circulation in response to changes in the hydrological cycle, Nature, 378(6553), 145-149.

Slubowska, M. A., N. Koc, T. L. Rasmussen, and D. Klitgaard-Kristensen (2005), Changes in the flow of Atlantic water into the Arctic Ocean since the last deglaciation: Evidence from the northern Svalbard continental margin, 80°N, Paleoceanography, 20, doi: 10.1029/2005PA001141.

Solomon, S., D. Qin, M. Manning, Z. Chen, M. Marquis, K. Averyt, M. Tignor, and H. Miller (2007), IPCC, 2007: Climate Change 2007: The Physical Science Basis. Contribution of Working Group I to the Fourth Assessment Report of the Intergovernmental Panel on Climate Change, .

Waelbroeck, C., L. Labeyrie, J. C. Duplessy, J. Guiot, M. Labracherie, H. Leclaire, and J. Duprat (1998), Improving past sea surface temperature estimates based on planktonic fossil faunas, Paleoceanography, 13, 272-283.

Yeager, S. G., C. A. Shields, W. G. Large, and J. J. Hack (2006), The Low-Resolution CCSM3, J.Clim., 19(11), 2545-2566.
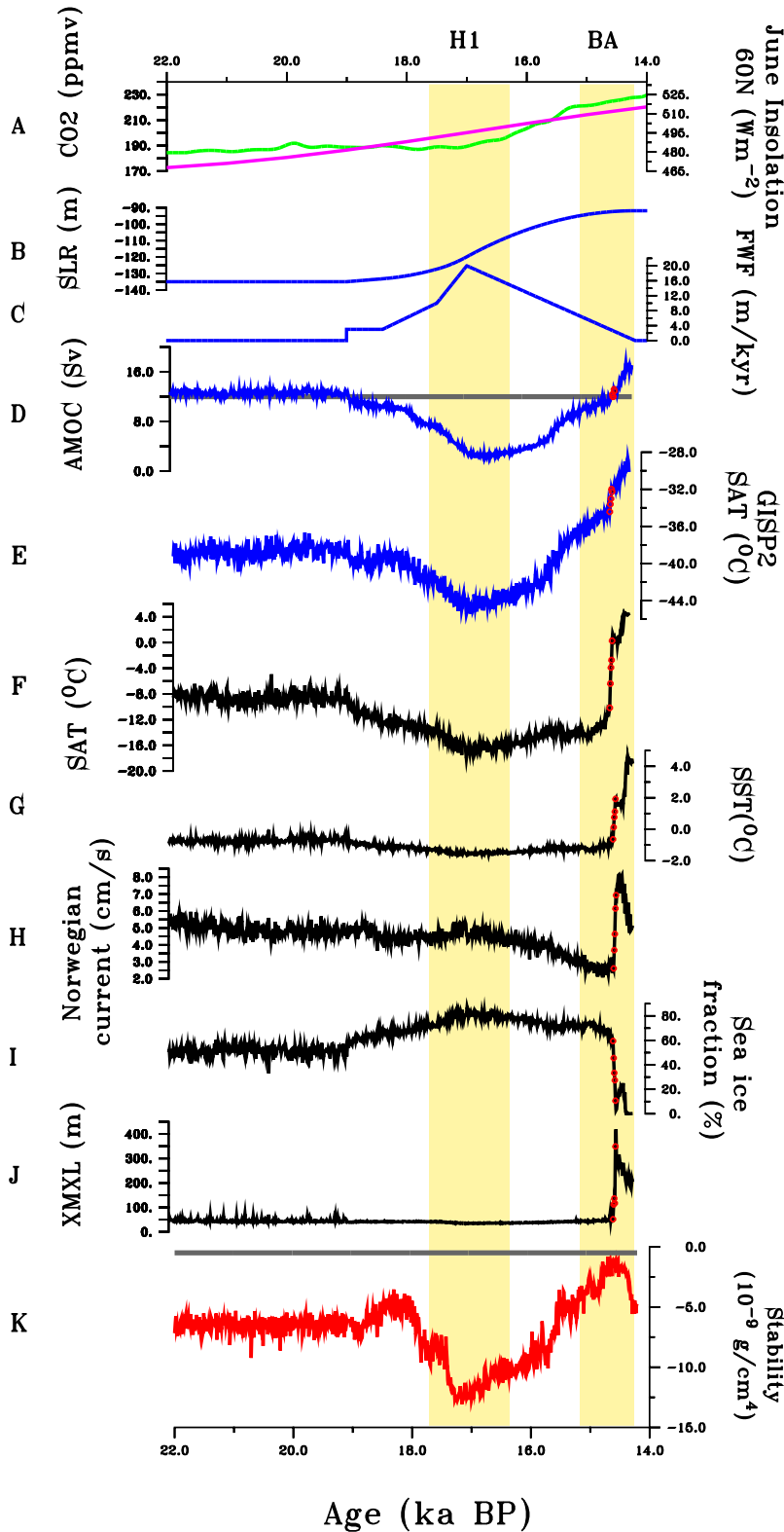
Figures

Figure 1. Transient simulation of the abrupt climate change in the Norwegian Sea. (**A**) June 21st insolation at 60° N (purple) [Berger, 1978] and atmospheric CO_2 concentration (green) [Joos and Spahni, 2008]. (**B**) Eustatic sea level. (**C**) NHMW fluxes. (**D**) Maximum AMOC transport (below 500 m). Sv, Sverdrup (1 Sverdrup = 10^6 m^3 s^{-1}). (**E**) Greenland SAT. **F-G**, Area average of the Norwegian Sea SAT (**F**) and SST (**G**). (**H**) Speed of Norwegian Current. **I-K**, Area average of the Norwegian Sea sea ice concentration (**I**), maximum mix layer depth (**J**) and density stability (**K**, dρ/dz at 300 m depth, negative means stable). BP, before present. All data are shown in decadal mean averages. The five circles denote the data between 14.53 and 14.49 ka.
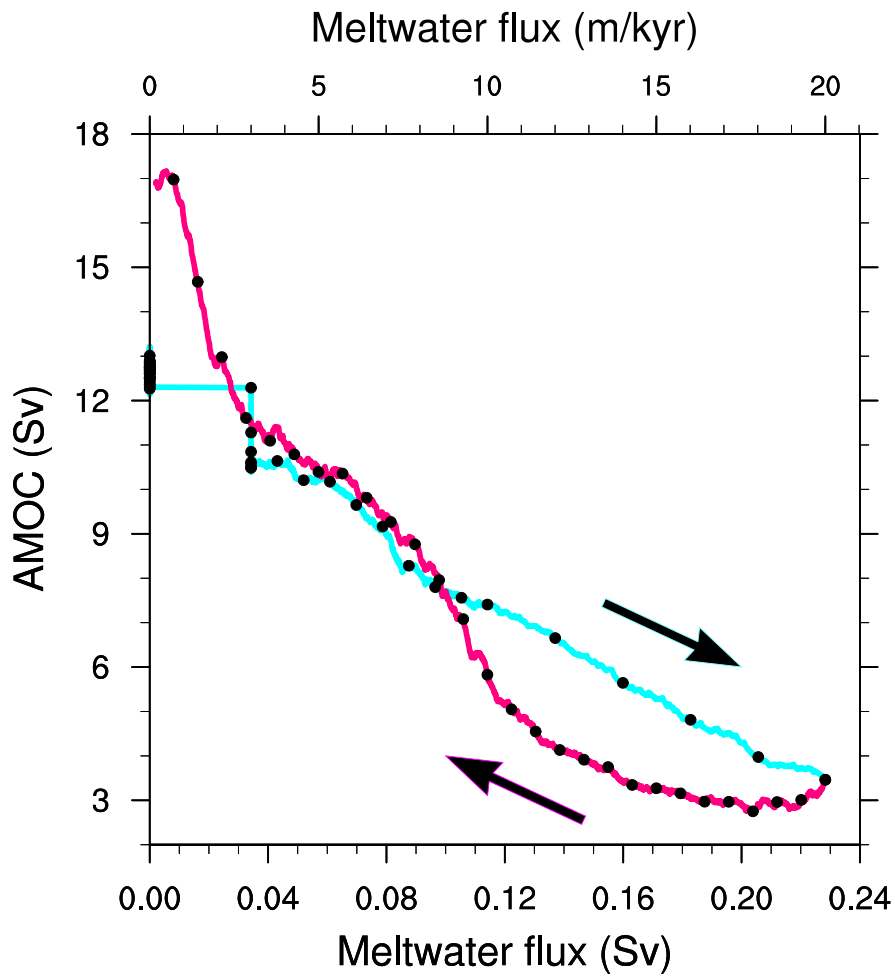
Figure 2. The co-variability between AMOC and NHMW flux in the transient simulation. Each dot represents 100-year running mean. Blue line is for the early part with the increase of the NHMW in the transient simulation and purple line for the latter part with the reduction of the NHMW in TraCE-Abrupt.
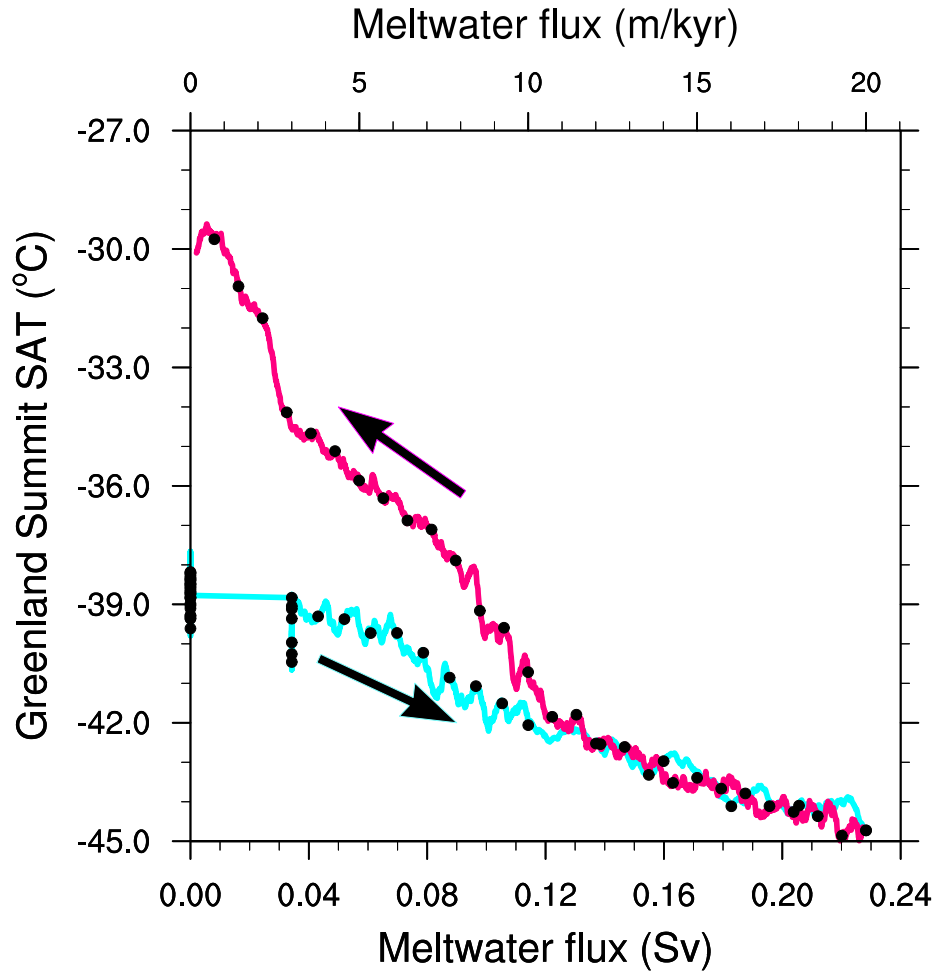
Figure 3. Same as Figure 2, but for the co-variability between Summit Greenland SAT and NHMW.
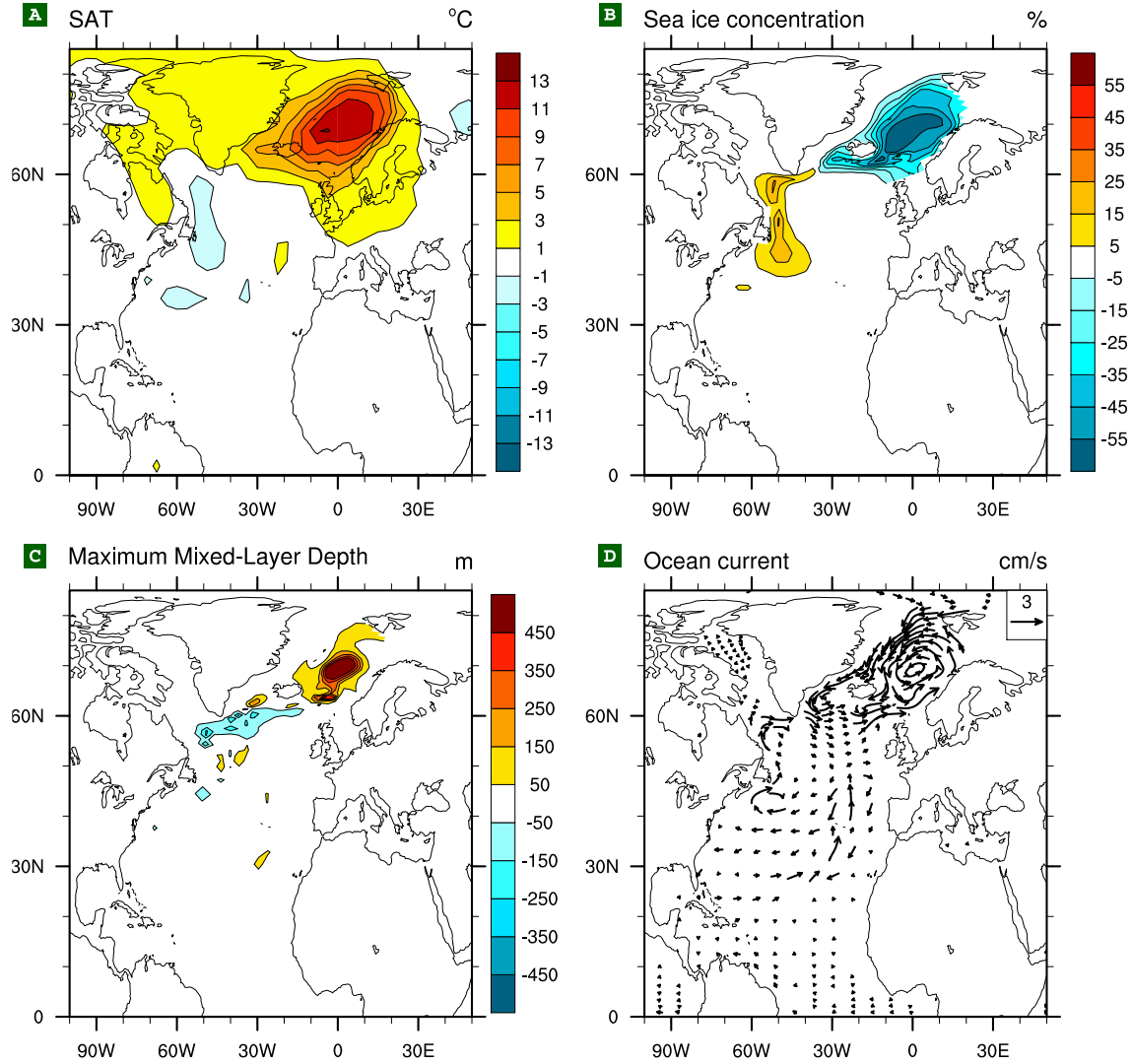
Figure 4. The abrupt climate change in the Norwegian Sea in the transient simulation between 14.53 and 14.49 ka. (**A**) SAT. (**B**) Sea ice concentration. (**C**) Maximum mix layer depth. (**D**) Subsurface ocean current at 350 m depth.
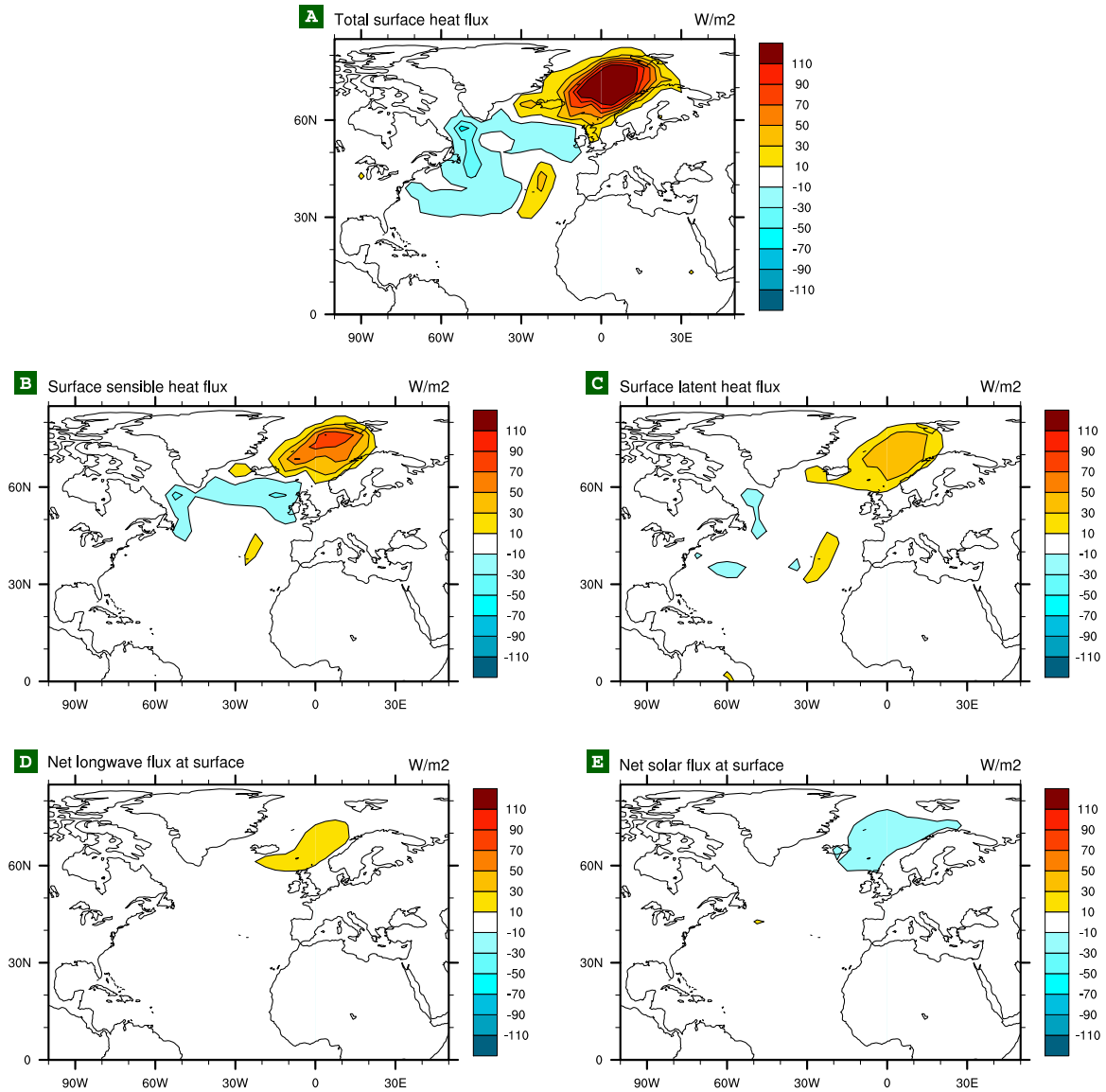
Figure 5. Same as Figure 4, but for surface heat flux (positive means out of the ocean and land). (**A**) Total surface heat flux. (**B**) Surface sensible heat flux. (**C**) Surface latent heat flux. (**D**) Net longwave heat flux at surface. (**E**) Net shortwave heat flux at surface.
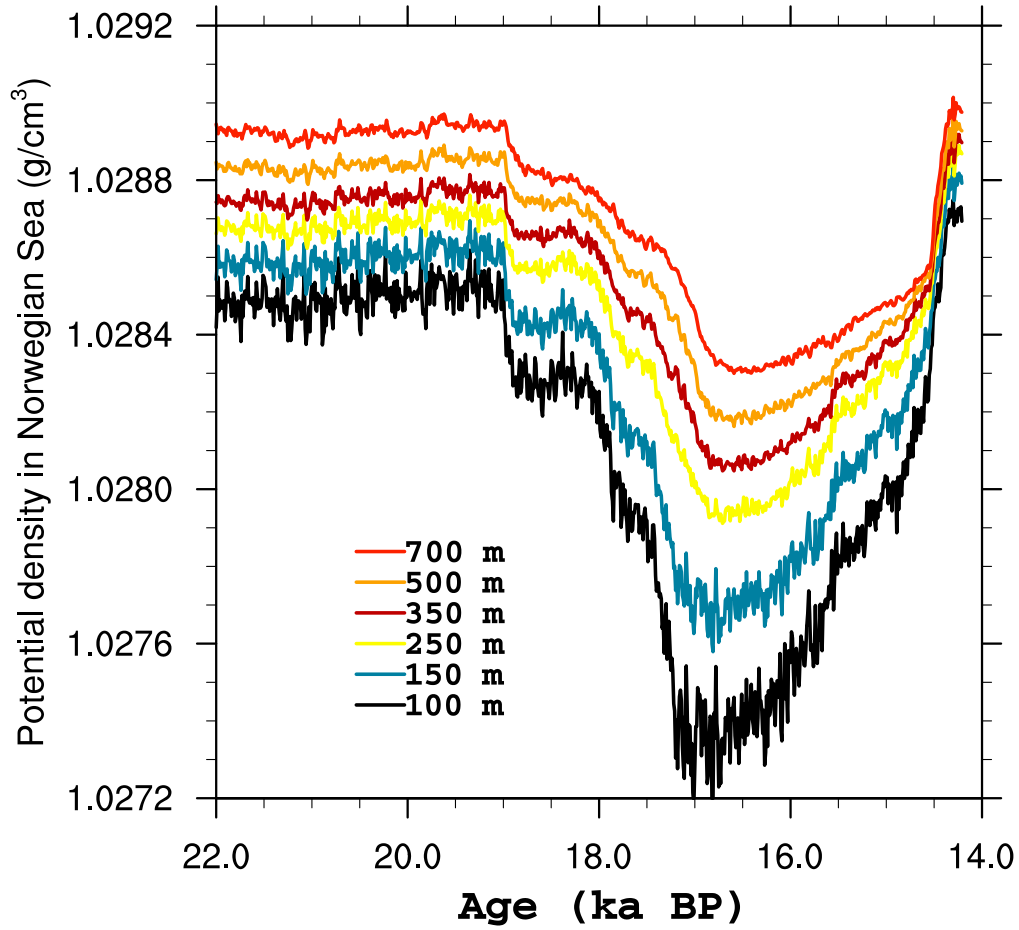
Figure 6. Evolution of the area average of the potential density in the Norwegian Sea at 100 m (black), 150 m (blue), 250 m (yellow), 350 m (dark red), 500 m (orange) and 700 m (red).

Chapter 5 Summary and Concluding Remarks

5.1 Summary

The transient climate evolution of last Ice-Age termination (21,000 to 10,000 years ago) provides key observations for constraining the climate sensitivity and enhancing the understanding of global carbon cycle. In this dissertation, I presented the first complete synchronously coupled atmosphere-ocean general circulation model simulation of the last deglaciation using NCAR-CCSM3. The transient simulation reproduces many major features of the deglacial climate evolution in Greenland, Antarctic, tropical Pacific, Southern and Deep Ocean, suggesting that NCAR-CCSM3 exhibits reasonable climate sensitivity in those regions and is capable of simulating abrupt climate change.

In *Chapter 1*, I described the transient climate evolution of last deglaciation in light of updated or new proxy data reconstructions during the last decade, focusing on the deglacial history of polar temperatures and its potential drivers, such as insolation, CO_2, ice sheet and ocean circulation. The updated proxy reconstructions show more clearly than before the close relationship between the ice cores and the ocean sediment reconstructions: the cooling of the Summit Greenland during OD and YD coincides with the slowdown of the AMOC; the warming of the Summit Greenland during BA and YD/Holocene transition coincides with the strengthening of the AMOC. The short synthesis of proxy data corroborates the notion that the variability of AMOC plays a critical role in modulating the millennial climate events during the last deglaciation [Broecker, 1985; McManus et al., 2004]. This provides a more concrete basis

for the possibility of conducting the simulation of the last deglaciation with the transient forcing of the AMOC, greenhouse gas concentration and the earth's orbital parameters.

After three years of number crunching between 2007 and 2010, I have completed the first transient simulation of the last 21,000 years (TraCE-21K) using a synchronously coupled atmosphere-ocean general circulation model (NCAR-CCSM3), thanks to the great advice from TraCE-21K team and the massive computational allocations at the National Center for Computational Science from the Department of Energy's INCITE program. TraCE-21K produces ~200,000 gigabytes of model output from both the 21,000-year control simulation and ~300 sensitivity runs. All of the simulations have been analyzed with the help of the NCAR component post processing utilities, which produced detailed diagnostics of the transient evolution of the atmosphere, ocean, sea ice and vegetation in the model.

In *Chapter 2*, I documented in great detail the transient simulation of the last deglaciation, focusing on the rates and locations of meltwater discharge. Given its significant climatic impact, large uncertainties of meltwater discharge during the last deglaciation represent the major challenge for this transient simulation. Another large uncertainty involves the timing of the Bering Strait opening, which controls the freshwater exchanges between the Pacific, Arctic and Nordic Sea, and has significant impact on the AMOC as well. All the other transient forcing, such as the change of the insolation and greenhouse gases, are fairly accurate. In this regard, the transient simulation of the last deglaciation depends heavily on which scheme of meltwater discharge is adopted. Therefore, one of the major products from the TraCE-21K project is the derivation of one reasonable scheme of the meltwater discharges for the last deglaciation.

Another major product from the TraCE-21K project is the transient simulation of the surface temperature and precipitation of the last 21,000 years. With the data-model comparison approach, the surface temperature simulation can potentially provide more accurate estimate of the climate sensitivity to changes of insolation, greenhouse gases and ocean circulation.

The successful simulation of the onset of Bølling-Allerød (BA) warming demonstrates the excellent climate sensitivity of NCAR-CCSM3 to changes of AMOC [Liu et al., 2009]. The complete simulation of the climate evolution of the last 21,000 years further demonstrates that the NCAR-CCSM3 exhibits excellent regional climate sensitivity to changes of greenhouse gases. For example, the transient simulation of the last 21,000 years successfully reproduces the paleoclimatic reconstructions of the ~12 ℃ deglacial warming over Summit Greenland, 2~3 ℃ deglacial warming over Tropical Pacific, 9~11 ℃ deglacial warming over Antarctic and 2~3 ℃ deglacial warming at 3000 m depth of the Pacific Ocean. In addition, the transient simulation of the precipitation in southeastern China also reproduces the relatively dryer condition during OD and YD and relatively wetter condition during BA and YD/Holocene transition (Fig. 1). Because the transient simulation of the last 21,000 years adopted the default parameterizations in NCAR-CCSM3, the excellent sensitivity of NCAR-CCSM3 to greenhouses provides more confidence to its projection of future global temperature change in the IPCC Fourth Assessment Report [Solomon et al., 2007].

The transient simulation of the climate evolution of last 21,000 years provides us with a great tool for the evaluation of various hypotheses on glacial-interglacial transitions, deglacial carbon cycles, the termination of the African Humid Period, etc. In ***chapter 3***, I provided quantitative evaluation of the prominent hypotheses of late Quaternary ice-age cycles

[Milankovitch, 1941; Stott et al., 2007; Huybers and Denton, 2008; Timmerman et al., 2009]. Using synchronously coupled atmosphere-ocean-dynamic vegetation general circulation model, I found that the Milankovitch theory not only survived another round of tests from the updated proxy data, but also survived the new test from the first transient simulation of the last deglaciation. The transient simulation supports the Milankovitch theory that the last deglaciation is triggered by the enhanced spring-summer insolation locally in the Northern Hemisphere. Northern Hemisphere glacial meltwater is able to induce the early deglacial warming of the Southern and Deep Ocean, and accounts for the lead-lag relationship among the Southern Ocean, tropical Pacific and Northern Hemisphere observed during the last Ice-Age termination. Furthermore, by inducing deep ocean warming and Southern Ocean sea ice retreat, Northern Hemisphere glacial meltwater likely plays an active role in deglacial CO_2 rise and gives an explanation for the associations between Heinrich events and atmospheric CO_2 rise.

In *chapter 4*, I demonstrated that NCAR-CCSM3 is capable of simulating the spontaneous abrupt climate change with smooth changes of external forcing [Alley et al., 2002]. NCAR-CCSM3 reproduces the 40-year Norwegian Sea abrupt warming event during the last deglaciation with the exact mechanism proposed by Lehman and Keigwin [1992]. This abrupt warming is triggered by the sudden switch–on of the Norwegian Sea deep water formation that results in the strong inflow of North Atlantic water and the rapid opening of the sea ice in the Norwegian basin. The timing of the abrupt warming can be estimated by projecting when the smooth changes of the subsurface water density profile reach the threshold of the marginal instability.

5.2   Concluding remarks

Before concluding, I want to draw your attention again to the meltwater discharge, the major challenge in TraCE-21K project. Even with the consideration of the 5 m uncertainty in the sea level record, there are still large discrepancies in deglacial sea level rise between the transient simulation and proxy data (Fig. 2).

In fact, the data-model discrepancies result from the disagreement between the reconstructions of surface temperature around the North Atlantic Ocean and the relative sea level. With the associated northward heat transport, the slowdown of the AMOC has been suggested to be responsible for the cooling around the North Atlantic Ocean during OD and YD [Broecker et al., 1985; McManus et al., 2004], and the acceleration of the AMOC should account for the warming around the North Atlantic Ocean during BA and YD/Holocene transition. In this regard, the cold periods of the North Atlantic Ocean during OD and YD should witness more meltwater discharge and sea level rise, while the warm periods around North Atlantic Ocean during BA and YD/Holocene transition should witness less meltwater discharge and sea level rise. However, the relative sea level data shows just the opposite, with less sea level rise within OD and YD, and more sea level rise during BA and YD/Holocene transition. In fact, this inconsistency between North Atlantic temperature and sea level rise during BA is one of the reasons behind the Antarctic origin of the meltwater pulse 1A [Clark et al. 1996]. However, it is still unclear what is responsible for the inconsistency between North Atlantic temperature and sea level rise during OD, YD and early Holocene, which results in the discrepancy in the sea level rise between the data and the transient simulation in those periods (Fig. 2).

One of the possible explanations for the data-model discrepancy in deglacial sea level rise is that the relative sea level data do not indicate the eustatic (global) sea level rise from meltwater discharge due to the local glacial isostatic adjustment [Lambeck and Chappell, 2001]. The eustatic sea level rise, i.e., the estimate of the sea level rise from the meltwater discharge, has been estimated to be 130-140 m during the last deglaciation [Yokoyama et al., 2000, Lambeck and Chappell, 2001, Clark and Mix, 2002]. This is consistent with 135 m eustatic sea level from the meltwater discharge in the transient simulation.

To conclude, I'm looking forward to the data assimilation of the last deglaciation with coupled ice sheet model and carbon cycle model, which will give the ultimate test of the Milankovitch theory and provide the more convincing answers for the future climate change on our planet.

References

Alley, R. B., J. Marotzke, W. Nordhaus, J. Overpeck, D. Peteet, R. Pielke Jr, R. Pierrehumbert, P. Rhines, T. Stocker, and L. Talley (2002), Abrupt climate change: Inevitable surprises, 244 pp., National Academy Press, Washington, D.C.

Bard, E., B. Hamelin, M. Arnold, L. Montaggioni, and G. Cabioch (1996), Deglacial sea-level record from Tahiti corals and the timing of global meltwater discharge, *Nature, 382*, 241.

Broecker, W. S., D. M. Peteet, and D. Rind (1985), Does the ocean-atmosphere system have more than one stable mode of operation? Nature, 315(6014), 21-26.

Clark, P. U., R. B. Alley, L. D. Keigwin, J. M. Licciardi, S. J. Johnsen, and H. X. Wang (1996), Origin of the first global meltwater pulse following the last glacial maximum, Paleoceanography, 11, 563.

Clark, P. U., and A. C. Mix (2002), Ice sheets and sea level of the Last Glacial Maximum, Quaternary Science Reviews, 21(1-3), 1-7.

Cutler, K. B., R. L. Edwards, F. W. Taylor, H. Cheng, J. Adkins, C. D. Gallup, P. M. Cutler, G. S. Burr, and A. L. Bloom (2003), Rapid sea-level fall and deep-ocean temperature change since the last interglacial period, Earth Planet.Sci.Lett., 206(3-4), 253-271, doi: DOI: 10.1016/S0012-821X(02)01107-X.

Hanebuth, T., K. Stattegger, and P. M. Grootes (2000), Rapid Flooding of the Sunda Shelf: A Late-Glacial Sea-Level Record, *Science, 288*(5468), 1033-1035, doi: 10.1126/science.288.5468.1033.

Huybers, P., and G. Denton (2008), Antarctic temperature at orbital timescales controlled by local summer duration, Nature Geosci, 1(11), 787-792.

Lambeck, K., and J. Chappell (2001), Sea level change through the last glacial cycle, Science, 292, 679-686.

Liu, Z., et al (2009), Transient Simulation of Last Deglaciation with a New Mechanism for Bølling-Allerød Warming, Science, 325(5938), 310-314, doi: 10.1126/science.1171041.

Lehman, S. J. and L.D. Keigwin (1992). Sudden changes in the North Atlantic circulation during the last deglaciation. Nature 356: 757-762.

McManus, J. F., R. Francois, J. M. Gherardi, L. D. Keigwin, and S. Brown-Leger (2004), Collapse and rapid resumption of Atlantic meridional circulation linked to deglacial climate changes, Nature, 428(6985), 834-837.

Milankovitch, M. (1941), Kanon der Erdbestrahlung und seine Anwendung auf das Eiszeitenproblem, Royal Serbian Academy Special Publication 132, Belgrade, Serbia.

Peltier, W. R., and R. G. Fairbanks (2006), Global glacial ice volume and Last Glacial Maximum duration from an extended Barbados sea level record, *Quaternary Science Reviews, 25*(23-24), 3322-3337.

Solomon, S., D. Qin, M. Manning, Z. Chen, M. Marquis, K. Averyt, M. Tignor, and H. Miller (2007), IPCC, 2007: Climate Change 2007: The Physical Science Basis. Contribution of Working Group I to the Fourth Assessment Report of the Intergovernmental Panel on Climate Change.

Stott, L., A. Timmermann, and R. Thunell (2007), Southern Hemisphere and Deep-Sea Warming Led Deglacial Atmospheric CO_2 Rise and Tropical Warming, Science, 318(5849), 435-438.

Timmermann, A., O. Timm, L. Stott, and L. Menviel (2009), The Roles of CO_2 and Orbital Forcing in Driving Southern Hemispheric Temperature Variations during the Last 21 000 Yr, J.Clim., 22(7), 1626-1640.

Wang, Y. J., H. Cheng, R. L. Edwards, Z. S. An, J. Y. Wu, C. -. Shen, and J. A. Dorale (2001), A High-Resolution Absolute-Dated Late Pleistocene Monsoon Record from Hulu Cave, China, Science, 294(5550), 2345-2348, doi: 10.1126/science.1064618.

Yokoyama, Y., K. Lambeck, P. De Deckker, P. Johnston, and L. K. Fifield (2000), Timing of the Last Glacial Maximum from observed sea-level minima, *Nature, 406*(6797), 713-716.
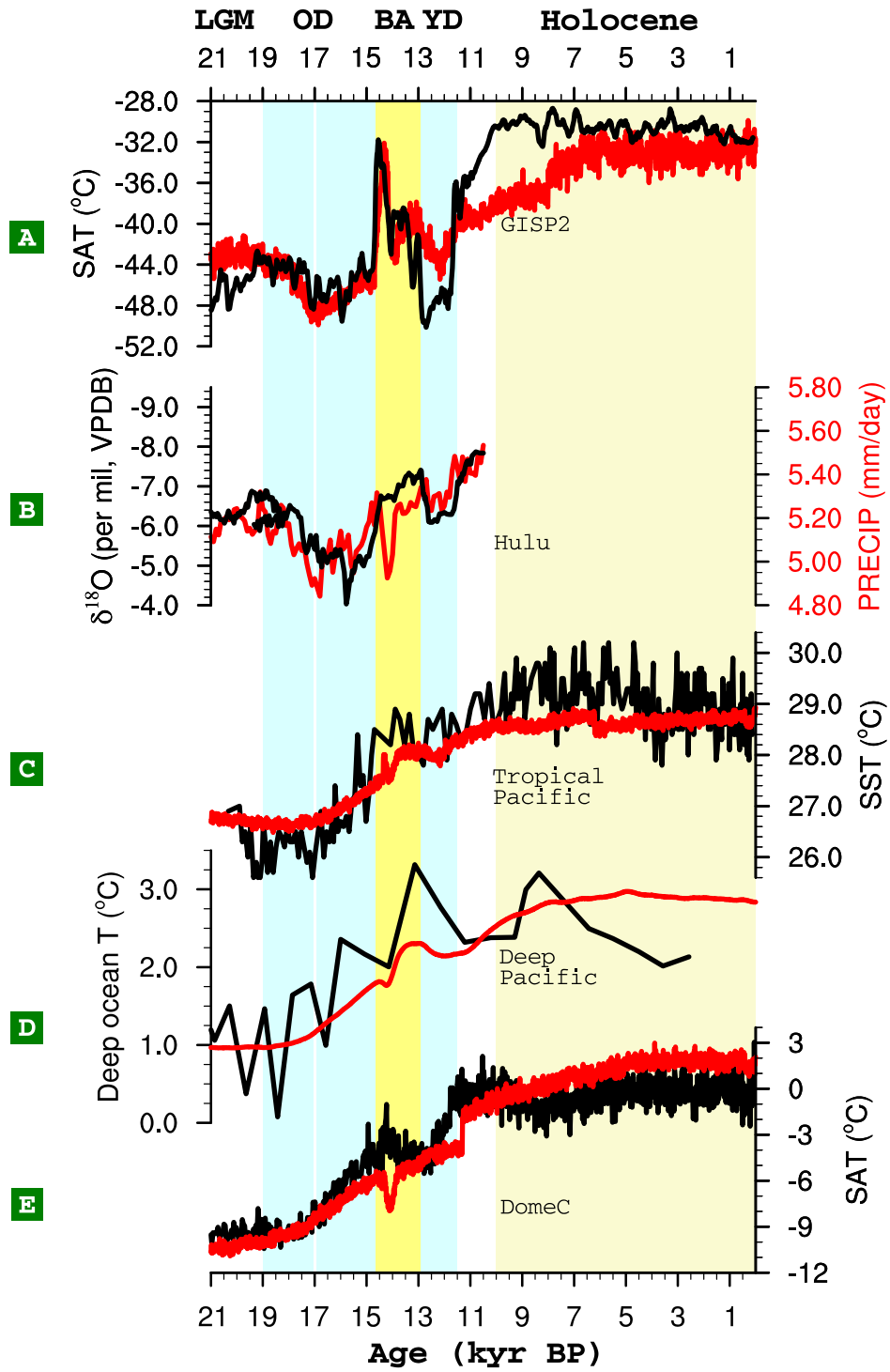
Figures

Figure 1: Data-model comparison for several benchmark time series. (**A**) Greenland surface air temperature based on Greenland Ice Sheet Project 2 (GISP2) $\delta^{18}O$ reconstruction with borehole temperature calibration [Cuffey and Clow, 1997] and in the model (model offset by –4.5°C). (**B**) $\delta^{18}O$ of Hulu Cave stalagmites [Wang et al., 2001] and southeastern China (32° N and 110° E) precipitation in the model. (**C**) SST in the west pacific warm pool from reconstruction (core MD98-2176) [Stott et al., 2007] and in the model (model offset by -0.4°C). (**D**) Deep ocean temperature in eastern equatorial Pacific from reconstruction [Martin et al., 2005] and in the model (model offset by 2.5°C). (**E**) Antarctic SAT based on Dome C δD reconstruction [Jouzel et al., 2007] and in the model. Black is used for the reconstructions, and red for transient simulation. All model variables are shown in 10-year averages. Overall, model simulations are in good agreement with the proxy records. BP, before present.
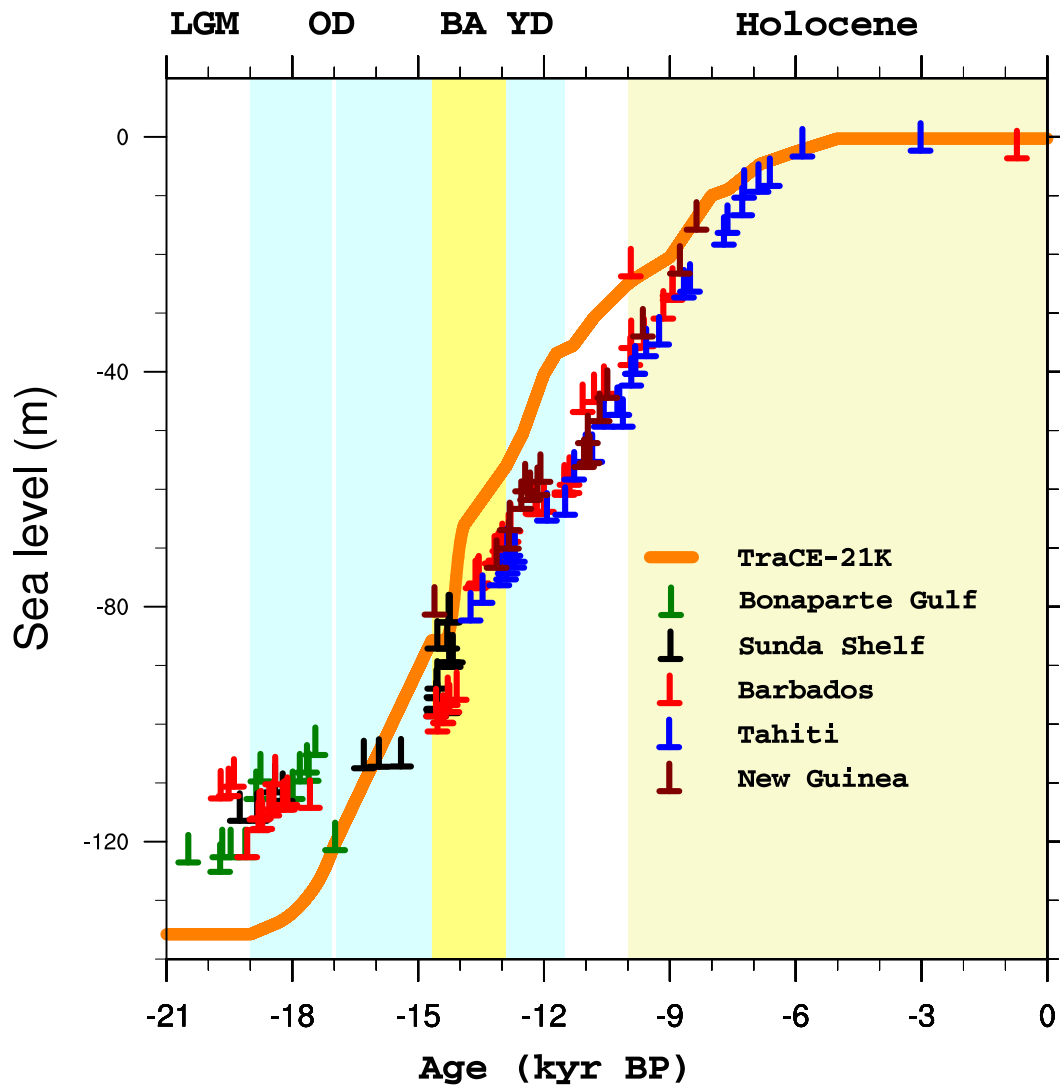
Figure 2: Relative sea level from the reconstructions and eustatic sea level in the model (orange). Sea level data are from Bonaparte Gulf (green) [Yokoyama et al., 2000], Sunda Shelf (black) [Hanebuth et al., 2000], Barbados (red) [Peltier and Fairbanks, 2006], Tahiti (blue) [Bard et al., 1996] and New Guinea (dark red) [Cutler et al., 2003]. The half-pluses represent the 5 m depth uncertainty of the relative sea level records.